creative commons
COMMONS DEED

저작자표시-비영리-변경금지 2.0 대한민국

이용자는 아래의 조건을 따르는 경우에 한하여 자유롭게

- 이 저작물을 복제, 배포, 전송, 전시, 공연 및 방송할 수 있습니다.

다음과 같은 조건을 따라야 합니다:

저작자표시. 귀하는 원저작자를 표시하여야 합니다.

비영리. 귀하는 이 저작물을 영리 목적으로 이용할 수 없습니다.

변경금지. 귀하는 이 저작물을 개작, 변형 또는 가공할 수 없습니다.

- 귀하는, 이 저작물의 재이용이나 배포의 경우, 이 저작물에 적용된 이용허락조건을 명확하게 나타내어야 합니다.
- 저작권자로부터 별도의 허가를 받으면 이러한 조건들은 적용되지 않습니다.

저작권법에 따른 이용자의 권리는 위의 내용에 의하여 영향을 받지 않습니다.

이것은 이용허락규약(Legal Code)을 이해하기 쉽게 요약한 것입니다.

Disclaimer

dCollection

ULSAN NATIONAL INSTITUTE OF
SCIENCE AND TECHNOLOGY

ULSAN NATIONAL INSTITUTE OF
SCIENCE AND TECHNOLOGY

Doctoral Thesis

Mechanisms and remote impacts of Arctic amplification

Doyeon Kim

Department of Urban and Environmental Engineering
(Environmental Science and Engineering)

Ulsan National Institute of Science and Technology

2022

ULSAN NATIONAL INSTITUTE OF
SCIENCE AND TECHNOLOGY

Mechanisms and remote impacts of Arctic amplification

Doyeon Kim

Department of Urban and Environmental Engineering
(Environmental Science and Engineering)

Ulsan National Institute of Science and Technology

ULSAN NATIONAL INSTITUTE OF
SCIENCE AND TECHNOLOGY

Mechanisms and remote impacts of Arctic amplification

A thesis/dissertation submitted to
Ulsan National Institute of Science and Technology
in partial fulfillment of the
requirements for the degree of
Doctor of Philosophy

Doyeon Kim

06.15.2022 of submission

Approved by

Advisor
Sarah M. Kang

Doyeon Kim

ULSAN NATIONAL INSTITUTE OF
SCIENCE AND TECHNOLOGY

Mechanisms and remote impacts of Arctic amplification

This certifies that the thesis/dissertation of Doyeon Kim is approved.

06.15.2022 of submission

Signature

Advisor: Sarah M. Kang

Signature

Dong-Hyun Cha

Signature

Myong-In Lee

Signature

Baek-Min Kim

Signature

Malte F. Stuecker

ULSAN NATIONAL INSTITUTE OF
SCIENCE AND TECHNOLOGY

Abstract

The Arctic surface temperature warmed two to three times faster than the global average, so called Arctic amplification (AA). However, identifying the drivers of AA is challenging due to the tightly inter-connected feedbacks in Arctic climate, addressing the questions of which feedback processes determine the AA and how the strength of interactions between the processes can be quantified explicitly. Furthermore, Arctic climate change studies have been highlighted due to the potential influence of the Arctic warming on climate at mid-latitude. In this thesis, feedback processes of AA and its remote effects are examined.

First, the mechanism of AA is investigated using an atmospheric coupled an aquaplanet slab ocean forced by a CO_2 doubling. Within the context of complex feedback mechanisms of AA, our approach is to first capture the essential dynamical processes in low complexity models, so we examine the polar amplification in the absence of surface albedo feedback with the sensitivity of polar surface warming response under different insolation conditions from equinox (EQN) to annual mean (ANN) to seasonally varying (SEA). Varying insolation greatly affects the climatological static stability. The equinox condition, with the largest polar static stability, exhibits a bottom-heavy vertical profile of polar warming response that leads to the strongest polar amplification. In contrast, the polar warming response in ANN and SEA exhibits a maximum in the mid-troposphere, which leads to only weak polar amplification. The mid-tropospheric warming maximum, which results from an increased poleward atmospheric energy transport in response to the tropics-to-pole energy imbalance, contributes to polar surface warming via downward clear-sky longwave radiation. However, it is cancelled by negative response in shortwave cloud radiative effect (SWCRE) locally. The strong negative SWCRE response in local cloud response is a controlling factor for determining the degree of polar amplification and its seasonality.

To understand the role of SWCRE in the projection of AA, the study necessitates a further investigation with realistic model comparisons. Using CMIP (Coupled Model Intercomparison Project) models, we decompose the SWCRE over the Arctic surface and analyze inter-model differences in quadrupled CO_2 simulations. This is done by taking into account the fact that the response of SWCRE to Arctic warming is influenced by change in surface albedo, cloud amount, and cloud microphysics. In sunlight season, reduction in surface albedo associated with sea ice loss is directly linked to strong negative SWCRE and explains the considerable model discrepancy. Arctic clouds may hamper the positive surface albedo feedback by albedo change with (1) decreasing incoming shortwave radiation due to cloud reflection (42%) and (2) decreasing of shortwave reaching the surface after being reflected by clouds. In addition, increased (decreased) cloud amount and cloud liquid water are shown to be less (more) incoming shortwave fluxes at the surface, but not dominating factors to the Arctic surface radiation budget and its inter-model variation. As a results, this study reasonably decomposes the

ULSAN NATIONAL INSTITUTE OF
SCIENCE AND TECHNOLOGY

individual SWCRE feedback at the Arctic surface and emphasizes that considering not only the cloud amount or its properties, but also surface albedo change is critical for the prediction of SWCRE on the Arctic surface.

Lastly, the study examines the effects of the vertical structure of polar warming on the remote atmospheric circulation. We apply thermal forcing at different vertical levels in the Northern Hemisphere polar region in two atmospheric global climate models of different complexity, both coupled to an aquaplanet slab ocean. The efficacy of polar heating in perturbing the remote climate increases with the altitude at which it is applied. This robust sensitivity arises from the dominance of surface temperature contribution to the outgoing longwave radiation owing to the large emissivity of the polar troposphere. An upper-level polar heating has a smaller fraction of forcing balanced by radiative flux changes and a larger contribution from atmospheric energy transport changes, which provokes larger shifts in the extratropical jet and Hadley circulation. Our results suggest increasingly far-reaching impacts of Arctic warming as a less surface-trapped profile is projected for seasonally ice-free conditions in the near future.

ULSAN NATIONAL INSTITUTE OF
SCIENCE AND TECHNOLOGY

ULSAN NATIONAL INSTITUTE OF SCIENCE AND TECHNOLOGY

Contents

Chapter 1. Introduction 1

1.1. Motivation 1

1.2. Inter-connected feedback mechanisms in the Arctic 3

1.3. Importance of shortwave surface energy budget in the Arctic 5

1.4. Diverged conclusions on the potential influence of the Arctic on climate at mid-latitude 6

1.5. Research objectives and outline 7

Chapter 2. Feedback diagnostic frameworks 9

2.1. Partial radiative perturbation 9

2.2. Radiative kernel technique 10

Chapter 3. Sensitivity of Polar Amplification to Varying Insolation Conditions 12

3.1. Background 12

3.2. Data and methodology 14

3.2.1. Prescribed cloud radiative feedback 14

3.2.2. Radiative kernel technique in slab ocean model 15

3.3. Results 15

3.3.1. Polar amplification in aquaplanet 15

3.3.2. Cloud response 21

3.3.3. Seasonality of polar amplification 24

3.3.4. Feedbacks and remote effects 30

3.4. Summary and discussion 33

ULSAN NATIONAL INSTITUTE OF SCIENCE AND TECHNOLOGY

Chapter 4. The decomposition of changes in the Arctic shortwave cloud radiative effects....36

4.1. Background....36

4.2. Data and methodology....38

4.2.1. Offline radiation calculation....38

4.2.2. Extend APRP method for the Arctic surface SWCRE....39

4.2.3. Datasets....40

4.3. Results....43

4.3.1. Model projections of changes in Arctic surface SWCRE....43

4.3.2. Validation of extended APRP method: focusing on the Arctic surface SWCRE....45

4.3.4. Inter-model spread in projected Arctic surface SWCRE....51

4.3.5. Uncertainties of Arctic surface SWCRE in present-day....55

4.5. Summary and discussion....58

Chapter 5. Atmospheric circulation sensitivity to changes in the vertical structure of polar warming....59

5.1. Background....59

5.2. Data and methodology....60

5.3. Results....61

5.4. Summary and discussion....70

6. Summary....72

Bibliography....74

ULSAN NATIONAL INSTITUTE OF SCIENCE AND TECHNOLOGY

List of figures

Figure 1.1. Summary for the local and remote mechanisms of AA.

Figure 3.1. (a) Zonal- and time-mean surface temperature response (K) in 2xCO_2. (b-d) Shading indicates the zonal- and time-mean temperature response (K) in 2xCO_2 and contours indicate the static stability (with an interval of 0.4℃/100m) in 1xCO_2, defined as $\frac{d\theta}{dz} = -\frac{\rho g}{(RT)} \times \frac{d\theta}{dp}$ following Graversen and Wang (2009), in (b) EQN, (c) ANN, and (d) SEA.

Figure 3.2. A comparison of actual surface temperature response in SEAFC (black) and its prediction by removing the cloud feedback contribution (blue in Fig. 3.9a) from the surface temperature response in SEA (gray).

Figure 3.3. Changes in mid-tropospheric temperature (450-700 hPa) poleward of 70° (K) versus changes in (a) atmospheric energy transport at 70°, and (b) eddy latent energy transport at 70° (PW). Changes in downward longwave radiation at the surface poleward of 70° (W/m^2) versus changes in (c) mid-tropospheric temperature (450-700 hPa) and (d) surface temperature poleward of 70° (K). Simulations are color coded as in the legend of Figure 3.4a. The open squares indicate the models with prescribed CRE.

Figure 3.4. Zonal- and time-mean responses to 2xCO_2 in (a) cloud radiative effects at TOA (CRE_{TOA}; W/m^2) and (b) cloud fraction (%) in SEA (shading) and ANN (contour; interval is 1%). (c) Changes in mid-tropospheric temperature (450-700 hPa) poleward of 70° (K) versus area-mean CRE_{TOA} changes in the tropics (<20°; W/m^2). (d) Polar Amplification Index (PAI; unitless) versus area-mean CRE_{TOA} changes poleward of 60° (W/m^2). Simulations are color coded as in the legend of panel (a). The open squares indicate the models with prescribed CRE.

Figure 3.5. (a) Same as in Figure 3.1a, but for different simulations as noted in the legend (b-d). Same as in Figure 3.1b-d, but for (b) SEAFC, (c) SEAFC_POL, and (d) SEAFC_TRO.

Figure 3.6. (Top) low cloud fraction (%), (middle) cloud radiative effects at the surface (W/m^2), and (bottom) surface temperature (K). In the left column, black and orange lines are the annual averages of zonal-mean responses for SEA and ANN, respectively. The right column indicates the monthly zonally averaged responses in SEA.

Figure 3.7. Changes in (a) cloud fraction (%), (b) relative humidity (%), (c) temperature (K), and (d) specific humidity (g kg^{-1}) averaged over poleward of 60°N for the August-September-October (red), and February-March-April (blue) in SEA.

Figure 3.8. Monthly Polar Amplification Index (PAI; unitless) in SEA (black solid), SEAFC (black dashed), and ANN (orange solid) for the NH.

Figure 3.9. Zonal- and time-mean partial temperature changes (K) attributed to 2xCO_2 forcing (red),

ULSAN NATIONAL INSTITUTE OF SCIENCE AND TECHNOLOGY

Planck (violet), transport (pink), water vapor feedback (green), cloud feedback (blue), and lapse rate feedback (orange), weighted by the global-mean Planck feedback following Feldl and Roe (2013). The sum of colored lines is shown in grey circled lines and the total surface temperature change, shown as black solid and dash-dot in Figure 3.5a, in black circled lines. (a) SEA and (b) SEAFC.

Figure 3.10. Zonal- and time-mean partial temperature changes (K) attributed to lapse rate feedback in EQN (green), SEA (black), and ANN (orange).

Figure 4.1. The box-and-whisker plots of results from 54 CMIP models (Table 4.1) after an abrupt quadrupling of CO_2 concentrations from the corresponding pre-industrial control climatology. The bars indicate the spread of changes in **a.** surface SWCRE (W/m^2) and **b.** cloud amount (%) averaged over the Arctic Ocean during the sunlit season (i.e., March through September). Extreme outliers, presented by the grey cross marks, are defined as points beyond three times the interquartile range from the edge of the box.

Figure 4.2. Average monthly maps of changes in surface SW radiation budget (W/m^2) in response to increases in CO_2 from the CESM2 model simulations calculated by the PRP method. Months are averaged during the sunlight season. **a.** Changes in surface net SW fluxes attributed to changes in **b.** surface albedo in clear-sky, **c.** surface albedo in CRE, **e.** cloud properties, and **d.** extra components such as water vapor, gases, and aerosols. **d.** The residual of the SW fluxes between the sums of all radiative components in the PRP method and model outputs.

Figure 4.3. Monthly changes in surface net SW fluxes (W/m^2) in response to increases in CO_2 from the CESM2 model simulations calculated by the PRP (black solid line) and APRP (colored solid line) methods. **a.** Changes in surface net SW fluxes averaged over the Arctic Ocean are divided into each radiative component by the PRP and APRP methods (**b-e**). **f.** The residual is calculated by subtracting the sum of all radiative components in the PRP and APRP methods from the model outputs.

Figure 4.4. Schematic for changes in surface SW fluxes. **a.** The surface albedo effect in a clear-sky. The changes in SWCRE (**b-e**) are estimated by the sum of **b.** albedo-cloud masking effect, **c.** albedo-cloud reflecting effect, **d.** cloud amount change, and **e.** cloud reflectivity change from extended APRP method.

Figure 4.5. Average monthly maps of changes in surface SWCRE (W/m^2) in response to increases in CO_2 from **a.** CMIP multi-model mean outputs, **b.** APRP calculations, and **c.** residual by subtracting the sum of APRP calculations from the model outputs. Months are averaged during the sunlight season after an abrupt global quadrupling of CO_2 concentrations from the corresponding pre-industrial control climatology for 54 CMIP models (23 for CMIP5 and 31 for CMIP6).

ULSAN NATIONAL INSTITUTE OF SCIENCE AND TECHNOLOGY

Figure 4.6. Same as in Fig 4.5. **a.** Changes in surface net SW fluxes (δSWNET) are divided into changes in **b.** clear-sky (δSWCLR) and **c.** cloud radiative effect (δSWCRE). Changes in SWCRE are further decomposed by **d.** albedo-induced term (δSWCRE-ALB) and **g.** cloud properties-induced term (δSWCRE-CP). Albedo-induced changes in SWCRE include **e.** albedo-cloud making effect (δSWCRE-ALBM) and **f.** albedo-cloud reflecting effect (δSWCRE-ALBR). Cloud properties-induced changes in SWCRE include **h.** cloud amount change (δSWCRE-CMT) and **i.** cloud reflectivity change (δSWCRE-CREF) from APRP calculation.

Figure 4.7. The plot of results from 54 CMIP models (Table 4.1) after an abrupt quadrupling of CO_2 concentrations from the corresponding pre-industrial control climatology. The attribution of the inter-model spread of changes in surface SWCRE (W/m^2) to the inter-model spread in the following components: albedo-cloud making effect (δSWCRE-ALBM), albedo-cloud reflecting effect (δSWCRE-ALBR), cloud amount change (δSWCRE-CMT) and cloud reflectivity change (δSWCRE-CREF) averaged over the Arctic Ocean during the sunlit season (i.e., March through September) from APRP calculation. The CMIP models are colored according to the changes in surface SWCRE (circles for CMIP5 and squares for CMIP6). The correlation coefficients of each component and the sum of all components from APRP calculation ($\delta SWCRE_{APRP}$) to the δSWCRE are marked separately for CMIP5 and CMIP6 at the bottom of the plot. The correlation coefficient in bold indicates it reaches the significance level of 0.05.

Figure 4.8. The scatter plot between the liquid water path (LWP, kg/m2) and cloud reflectivity (unitless) calculated by the APRP method. Circles and squares denote the results from CMIP5 and CMIP6, respectively, in yearly historical runs (Table 4.1) averaged over the Arctic Ocean during the sunlit season (i.e., March through September). Coloring from red to blue color is sorted in the ascending order of cloud reflectivity effect (SWCRE-CREF) in Figure 4.10.

Figure 4.9. Time series of the **a.** SWCRE (W/m^2), **b.** surface albedo (%), **c.** cloud amount (fraction %), and **d.** cloud reflectivity (%). The solid line shows the multi-model mean; the envelope represents +/– one standard deviation bounds for CMIP5/6 models.

Figure 4.10. Attribution of the inter-model spread of surface SWCRE (W/m^2) to the inter-model spread in the following components: albedo-cloud making effect (SWCRE-ALBM), albedo-cloud reflecting effect (SWCRE-ALBR), cloud amount effect (SWCRE-CMT) and cloud reflectivity effect (SWCRE-CREF) in the Arctic Ocean averaged for the sunlit season (March through September). Both CMIP models (Table 4.1) and reanalysis datasets are analyzed for the period from 1980 to 2014 (CMIP5 products are made over 1980-2015 by merging historical runs 1980-2005 with RCP 4.5 2005-2014) with the data interpolated to a common 1°×1° grid. The CMIP models are colored according to the surface SWCRE (circles for CMIP5 and squares for CMIP6) and the EAR5 (starts) and MERRA2 (cross) results are juxtaposed on the right. The correlation coefficients of each component to the SWCRE are

ULSAN NATIONAL INSTITUTE OF SCIENCE AND TECHNOLOGY

marked separately for CMIP5 and CMIP6 at the bottom of the plot. The correlation coefficient in bold indicates it reaches the significance level of 0.05. Note that the APRP calculation in Figure 4.10 sets the multi-model mean of CMIP5/6 as the reference climate state and marks indicate deviations in individual models and reanalysis from the reference states.

Figure 5.1. Response of time- and zonal-mean (a) temperature (K, shading), (b) zonal wind (m/s, shading) and (c) mean meridional streamfunction response (10^9 kg/s, shading). Solid black contours in (a) denote the forcing region. The black contours in (b) indicate the control climatology, with westerlies in solid and easterlies in dashed at a contour interval of 5 m/s. The black contours in (c) indicate the control climatology, with a clockwise circulation in solid and a counter-clockwise circulation in dashed at a contour interval of 5.5×10^{10} kg/s. Results from L990 (first column), L800 (second column), L700 (third column), and L550 (fourth column). Hatched regions indicate statistically insignificant values at the 95 % confidence level based on a two-sided t-test.

Figure 5.2. (a) The vertically-integrated prescribed heating (Q in Eq.5.1) and the zonal- and time-mean response of (b) OLR and (c) surface temperature for the reference set of experiments. (d) The OLR change resulting from an increase in temperature of 1 K at each layer (W/m^2/K/100 hPa) averaged over 60-90°N. The temperature kernel in GRaM (black) is compared with that in other models: CESM-CAM3 (green, Shell et al., 2008), CESM-CAM5 (yellow, Pendergrass et al., 2018), HadGEM (orange, Smith and Christopher 2018), EAR-Interim (red, Huang et al., 2017), GFDL-AM2 (purple, Soden et al., 2008) and Aquaplanet GFDL-AM2 (blue, Feldl et al., 2017), separately for all-sky (solid) and clear-sky (dashed). The surface component of the kernel (W/m^2/K) is indicated by the black diamond for GRaM, by squares and triangles for other models under all-sky and clear-sky conditions, respectively, with the same color-coding as for the atmospheric temperature kernel.

Figure 5.3. (a) The imposed heat flux (F_Q, black solid line), anomalous vertically-integrated atmospheric energy transport (δF_A, solid color-coded lines), and a flux corresponding to anomalous TOA radiation (δF_R, dashed color–coded lines) for the reference set of experiments with the same color coding as in Fig. 5.2b. (b) The response of the jet position, defined as the centroid latitude of 900 hPa zonal-mean zonal wind between 30°-60°N, normalized by the forcing amplitude as a function of atmospheric compensation C_A (%) averaged over 30°-60°N. (c) The response of the ITCZ position, defined as the centroid latitude of zonal-mean precipitation between 10°S-10°N normalized by the forcing amplitude, as a function of atmospheric compensation C_A (%) averaged over 10°S-10°N. The experiments with a varying forcing amplitude are differentiated by adjusting the marker size. The reference experiments are demarcated by black edge.

Figure 5.4. Same as Fig. 5.1 but for AM2 in (left) L990 and (right) L650.

Figure 5.5. Zonal and time mean response of (a) net TOA radiation and (b) clear-sky TOA radiation in L990 (solid) and L650 (dashed) for AM2. Units are W/m^2.

ULSAN NATIONAL INSTITUTE OF
SCIENCE AND TECHNOLOGY

List of tables

Table 3.1. Overview of all experiments. Unless indicated otherwise, clouds evolve freely.

Table 4.1. Descriptions of CMIP5, and CMIP6 models used in Chapter

ULSAN NATIONAL INSTITUTE OF
SCIENCE AND TECHNOLOGY

Chapter 1. Introduction

1.1. Motivation

The Arctic is a fast-changing region to climate change. Recently, the Arctic surface temperature warmed two to three times faster than the global average, so-called Arctic amplification (AA) (Arrhenius 1896; Manabe and Wetherald, 1975; Stuecker et al., 2018; Taylor et al., 2021). The AA not only carries a substantial effect on the local ecosystem (e.g., sea ice melt and sea-level rise) in the Arctic region but also potentially contributes to extreme weather events in mid-latitudes (Meredith et al., 2019; Francis and Vavrus, 2012).

Even though climate models robustly present the AA from CO_2 radiative forcing, there exists a large spread of AA projections across the Coupled Model Intercomparison (CMIP) models. The spreads are shown in the AA index—the increase in Arctic surface temperature normalized by the change in global mean surface temperature—ranging from a factor of two to a factor of four times (Boeke and Taylor, 2018). From surface budget analysis, the models that transfer more energy from summer to fall/winter contribute a more extensive AA (Boeke and Taylor, 2018; Feldl et al., 2020; Chung et al., 2020). Especially, significant shortwave absorption in summer is related to surface albedo feedback while Arctic clouds damp the positive surface albedo feedback (Sledd and L'Ecuyer, 2019; Alkama et al., 2020; Choi et al., 2020). This implies the predictability of surface albedo and clouds in the Arctic is essential to understanding uncertainty in the Arctic surface energy budget (Alkama et al., 2020; Choi et al., 2020). Besides the ice-albedo feedback, various inter-connected feedbacks contribute to AA such as an increase in atmospheric energy transport as a remote process (Alexeev et al., 2005; Cai, 2005; Chung and Räisänen, 2011). Several modeling studies estimate that the amount of Arctic warming due to remote processes could range from 50-80% of warming (Taylor et al., 2021).

Along with the uncertainty in AA intensity and its various controlling mechanisms, the significant divergence of the vertical structure of AA is found in models and reanalysis data. For instance, most model simulations confine Arctic warming to the lower troposphere but reanalysis data renders extended warming over the upper troposphere which is generally absent in models (Cohen et al., 2020). The disagreement on the intensity and vertical pattern of AA between CMIP models and reanalysis indicates our lack of understanding of the physical mechanisms underlying AA. Additionally, identifying the vertical warming patterns in AA is crucial because recent studies have shown that warming higher in the Arctic atmosphere more effectively perturbs the atmospheric circulation outside of the Arctic (He et al., 2020; Labe et al., 2020).

In this thesis, we further investigate and decompose feedback that can explain the mechanisms of AA and its remote effect, aiming to improve our understanding of the Arctic climate change

ULSAN NATIONAL INSTITUTE OF
SCIENCE AND TECHNOLOGY

considerably. This introductory chapter starts with the inter-connected feedback mechanisms (section 1.2) and the importance of the shortwave energy budget in Arctic climate projections (section 1.3). Also, diverged conclusions on the potential influence of the Arctic on climate at mid-latitude (section 1.4) are introduced and finally the research objectives are outlined (section 1.5).

ULSAN NATIONAL INSTITUTE OF
SCIENCE AND TECHNOLOGY

1.2. Inter-connected feedback mechanisms in the Arctic

Recent work has established AA as a coupled ocean-sea ice-atmosphere process (Chung et al., 2020; Taylor et al. 2021). The suite of coupled processes can be classified into local (within Arctic) and remote (non-Arctic) mechanisms, based upon the forcing source. Among multiple driving processes in Figure 1.1, surface albedo feedback is broadly regarded as a local leading driver to AA (Arrhenius, 1896; Manabe and Wetherald, 1975; Screen et al., 2012). To be specific, the melting of sea ice and snow in response to global warming decreases the surface albedo, enhancing the absorption of solar radiation at the Arctic surface. The shortwave absorption in summer is stored in the ocean and the ocean releases heat in fall/winter through surface heat fluxes, thereby contributing to AA (Sejas et al., 2014; Feldl et al., 2020; Chung et al., 2020). However, AA is found even in simulations in the absence of the surface albedo feedback (Alexeev et al., 2005; Langen et al., 2012). This implies that processes other than the locally induced surface albedo feedback are operative, such as an increase in atmospheric energy transport as a remote process (Fig. 1.1). Furthermore, the challenge to understanding the local and remote processes to AA is the inter-connected multiple processes in nature (Screen et al., 2012; Taylor et al., 2021). For instance, the increased poleward energy transport would likely increase heat and moisture in the Arctic, thereby affecting other local feedbacks such as cloud/water vapor response and accelerating sea ice loss. Therefore, the inherent complexity of the Arctic system poses significant challenges to our ability in distinguishing the importance of individual feedback mechanisms. At present, coupled feedbacks controlled by the local and remote drivers in the Arctic are exclusively investigated through 1) mechanism denial experiments where a physical process (e.g., sea ice albedo and cloud) is locked (Graversen and Wang 2009), 2) idealized simulations with the spatial distribution of forcing such as latitudinal prescribed surface heat flux (Park et al., 2018) or CO_2 increases (Stuecker et al., 2018) which are designed to quantify the roles of local and remote processes play in AA, and 3) radiative energy budget decomposition including radiative kernel technique which allows to separate individual radiative feedback contribution (Soden et al., 2008; Pithan and Mauritsen., 2014; Stuecker et al., 2018; Feldl et al., 2020). Based on the various diagnostic method above, we need integrated research to suggest fundamental physical process for Arctic climate change.

ULSAN NATIONAL INSTITUTE OF
SCIENCE AND TECHNOLOGY

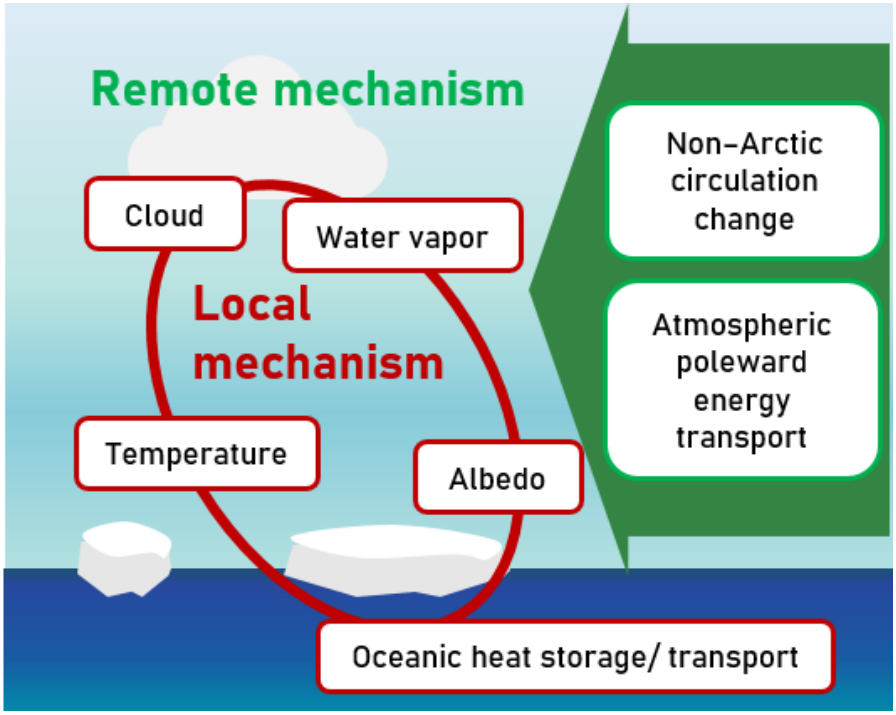

Figure 1.1. Summary for the local and remote mechanisms of AA.

ULSAN NATIONAL INSTITUTE OF
SCIENCE AND TECHNOLOGY

1.3. Importance of shortwave surface energy budget in the Arctic

As previously mentioned, the CMIP models produce a considerable inter-model spread in their projection of the AA and the largest inter-model spread is found in sea ice retreat regions following massive amounts of heat exchange at the surface (Boeke and Taylor, 2018). In particular, the shortwave feedback modulated by sea ice and clouds is the strongest in summer when the sea ice loss and sunlight are most extensive. However, the greatest Arctic warming with the significant model disagreement occurs in winter (Pithan and Mauritsen, 2014; Boeke and Taylor, 2018; Cohen et al., 2020) due to the seasonal energy transfer from summer to fall/winter in the ocean mixed layer processes (Feldl et al., 2020; Chung et al., 2020). This highlights that the surface flux diagnostics should be investigated to explain the driving mechanisms of AA and its seasonality (Boeke and Taylor, 2018). Furthermore, the relationship between Arctic sea ice and clouds strongly modulates radiative energy fluxes at the surface (Kay et al., 2008; Cesana et al., 2012; Karlsson and Svensson, 2013; Alkama et al., 2020; Choi et al., 2020) where Arctic clouds are implicated as a major uncertainty for the future cryosphere (Vavrus, 2004; Karlsson and Svensson, 2013; Sledd and L'Ecuyer, 2019; Alkama et al., 2020). The contemporary climate models exhibit the overall cloud radiative damping effect, especially in shortwave component when sea ice extent decreases in the presence of clouds over the Arctic. Therefore, we need to understand and quantify the surface shortwave radiative effect over the Arctic, focusing on the seasonality and cloud response of Arctic warming to reduce the uncertainty of AA projection.

ULSAN NATIONAL INSTITUTE OF
SCIENCE AND TECHNOLOGY

1.4. Diverged conclusions on the potential influence of the Arctic on climate at mid-latitude

In recent years, modeling and observation studies had substantial disagreements on whether AA is influencing mid-latitude weather or not. This necessitates modeling to observational evidence and mechanisms that may link Arctic warming and severe weather events in midlatitudes. Francis and Vavrus (2012) speculate that Arctic surface warming perturbs atmospheric circulation, driving the extremely cold winters in midlatitudes. The modeling study with prescribing sea ice concentration also supports that less sea ice condition with AA produces more frequent blocking events which are responsible for more cold-air advection to Eurasia (Mori et al., 2014). However, Blackport and Screen (2020) show the tendencies of AA-to-midlatitude linkage no longer continue in the longer term, updated to winter 2019/20. Moreover, large ensemble members from sea-ice perturbation simulations in Peings et al. (2021) have shown inconsistent mid-latitude responses from different 100-member subsets, implicating the substantial influence of internal variability in AA-to-midlatitude linkage. Thus, the AA and mid-latitude linkage is still challenging because of a lack of evidence to support it and contradictory results in previous studies.

Along with the uncertainty in AA-to-midlatitude linkage, several studies claim that the linkage is sensitive to the depth of vertical Arctic warming. In detail, upper-tropospheric warming rather than lower-tropospheric warming in the Arctic strengthens the linkage between AA-to-midlatitude (He et al., 2020; Labe et al., 2020). It means that deep Arctic warming may be crucial in the Arctic-to-midlatitude linkage with the fact that the near-surface intensification of AA, aligning with local feedback such as sea ice loss is insufficient for a mid-latitude response (He et al., 2020; Labe et al., 2020). However, the mechanism of atmospheric circulation sensitivity to changes in the vertical structure of Arctic warming is not yet understood.

ULSAN NATIONAL INSTITUTE OF
SCIENCE AND TECHNOLOGY

1.5. Research objectives and outline

The goal of this study can be to examine the mechanisms and remote impacts of Arctic amplification. To achieve the goal, the study adopted idealized modeling to first capture the essential dynamical processes in lower complexity models that could be applicable in higher complexity models. Then, the result is further investigated by feedback diagnostic frameworks.

The key research objectives of the thesis are:

1. To disentangle the inter-connected mechanism of AA with the targeted experiments
2. To quantify the role of shortwave cloud radiative effect in the Arctic
3. To understand remote impacts of AA depending on the vertical structure of Arctic warming

The thesis is outlined below:

- ✓ In Chapter 2, we describe a suite of comprehensive feedback diagnostic frameworks (e.g., atmospheric energy budget, PRP method, radiative kernel technique, and extended APRP which is a newly developed shortwave decomposition). The decomposition of feedback processes quantifies the process contribution to AA and its remote effect.
- ✓ In Chapter 3, the inter-connected mechanisms of AA are investigated by the idealized model simulations. We present the sensitivity of polar amplification to varying insolation conditions. Interestingly, even in the absence of surface albedo feedback, the surface warming pattern in response to $2xCO_2$ can be polar amplified. This is because of the large polar static stability and increase in atmospheric energy transport. We further confirm the role of the shortwave cloud radiative effect on polar amplification with cloud locking simulations. This chapter is published in *Climate Dynamics* (Kim et al., 2018).
- ✓ In Chapter 4, the new decomposition method focusing on the shortwave cloud radiative effect at the Arctic surface is introduced. Then, the cause of the inter-model spread in the shortwave cloud radiative effect across the CMIP model outputs is investigated. The comparison of diagnostics among CMIP models reveals the relationship between surface albedo and cloud in the shortwave cloud radiative effect at the Arctic surface.
- ✓ In Chapter 5, the study addresses the question of how the remote effects of polar warming depend on its vertical structure. This study uses a series of experiments in which thermal forcing is applied at different vertical levels over the polar region. We find that the warming further from the surface is more effective at perturbing the remote climate, such as the extratropical jet and Hadley circulation, than the near-surface warming. This suggests that Arctic warming may have more far-reaching impacts in the near future as the Arctic transitions

ULSAN NATIONAL INSTITUTE OF
SCIENCE AND TECHNOLOGY

to an ice-free summer season and there is less near-surface warming. This chapter is published in *Geophysical Research Letters* (Kim et al., 2021).

- ✓ In Chapter 6, we provide a summary and discussion of the thesis.

ULSAN NATIONAL INSTITUTE OF
SCIENCE AND TECHNOLOGY

Chapter 2. Feedback diagnostic frameworks

Understanding the changes in atmospheric radiative fluxes due to the multiple feedbacks (e.g., surface albedo, temperature, water vapor, and cloud feedback) requires isolating individual feedback contributions. In this thesis, we decompose the feedbacks using a suite of feedback diagnostic frameworks, thereby investigating the mechanisms of the Arctic amplification and its remote effect. This complementary chapter focuses on describing a variety of feedback decomposition methods used to conduct this research.

2.1. Partial radiative perturbation

Partial radiative perturbation (PRP) was firstly introduced by Wetherald and Manabe (1988) to estimate individual feedback contributions. PRP calculates the change in TOA (top of the atmosphere) flux by replacing a single variable from the perturbed climate into the control climate (e.g., double CO_2 climate to the control climate) with an offline radiative transfer model.

The PRP produces the direct response of various feedbacks most accurately while the method neglects the coupling effect in feedbacks, thereby assuming that all fields are uncorrelated. In this regard, the two-way PRP method is recommended by Colman and McAvaney (1997) with the advantage of removing the decorrelation perturbation. Firstly, the substitution of radiation relevant variables from perturbed climate (ptr) such as doubling CO_2 climate into control climates (ctl) produces radiation perturbation, $\delta_{\mathrm{ptr-ctl}}R_x$ for filed x (that is, forward) where x is a single variable such as temperature, humidity, gases, and surface albedo (Klocke et al., 2013). After that, the substitution of radiation relevant variables from control climates (ctl) into perturbed climate (ptr) produces radiation perturbation, $\delta_{\mathrm{ctl-ptr}}R_x$ (that is, backward). Then, the final radiation perturbation is given by

$$\frac{\delta_{\mathrm{ptr-ctl}}R_x - \delta_{\mathrm{ctl-ptr}}R_x}{2}. \tag{2.1}$$

The PRP method is more complex to implement than the other methods because the repeated run of an offline radiative transfer model is computationally expensive. Also, the method becomes increasingly inaccurate when different radiative transfer codes are applied for different models (Klocke et al., 2013).

ULSAN NATIONAL INSTITUTE OF
SCIENCE AND TECHNOLOGY

2.2. Radiative kernel technique

The radiative kernel technique (Soden et al., 2008; Pendergrass et al., 2018) is a simple method for calculating climate feedbacks. It is similar to the PRP method, so the radiative kernel can be alternatively applied across different models with fewer calculations in which the kernel depends only on the radiative algorithm and the base climate state. The technique decomposes individual feedback into the radiative kernel ($\frac{\partial R}{\partial x_i}$) and climate change anomaly from actual model variables (Δx) where x is single variable such as temperature, water vapor, and surface albedo. Here, the radiative kernel is a different response of the radiative fluxes to standard change in each climate variable. For example, the temperature kernel indicates the radiative response to incremental increases in temperature of 1K at each atmospheric layer or at the surface, holding all other components (e.g., water vapor, cloud, and albedo) fixed. Then, the differential response of radiation (ΔR) to changes in each variable could be decomposed as:

$$\Delta R_i = \frac{\partial R}{\partial x_i} \Delta x$$

Despite the radiative kernel technique can be easily applied to quantify the contributions from the different feedback processes (Pithan and Mauritsen, 2014; Stuecker et al., 2018; Feldl et al., 2020), the kernel technique is generally less accurate than the PRP method. To be specific, spurious differences in radiative kernels may arise when a different control climate is used (e.g., the control climate of a GCM and observation) is used (Thorsen et al., 2018).

ULSAN NATIONAL INSTITUTE OF
SCIENCE AND TECHNOLOGY

2.3. Approximate Partial Radiative Perturbation method

For the shortwave fluxes, Approximate PRP (APRP) (Taylor et al., 2007) method is developed. The APRP method accurately reproduces PRP estimation for the shortwave at TOA with reduced practical difficulties in PRP by using a one-layer radiation model instead of an offline radiative transfer model. The one-layer radiation model is the product of seven radiative parameters (i.e., atmospheric absorption and reflection, surface albedo assessed in both the clear and overcast skies, and a cloud area fraction). Based on the simplified shortwave radiative model, APRP requires a modest amount of model outputs that are commonly archived from climate model simulations. The APRP method is also applicable to the surface SW fluxes following Kim et al. (2022):

$$\delta SW = \delta SW_{s} + \delta SW_{\alpha} + \delta SW_{cld} + \delta SW_{ncld} \quad (2.3)$$

The δSW represents the changes in shortwave flux with the subscripts S, α, cld, and ncld being the contribution from the insolation, surface albedo, cloud, and non-cloud radiative properties, respectively.

In the Arctic, there is a large uncertainty to changes in the surface shortwave radiation budget in the summertime, which also hesitates the predictability of Arctic climate change. In this thesis, we further break down the conventional APRP method focusing on the Arctic surface shortwave budget. To be specific, the extended APRP method will allow us to decompose the response of the SW flux at the Arctic surface along with contributions from the changes in surface albedo, cloud (e.g., albedo-cloud masking effect, albedo-cloud reflecting effect, cloud amount change, and cloud reflectivity change), and non-cloud radiative properties.

ULSAN NATIONAL INSTITUTE OF
SCIENCE AND TECHNOLOGY

Chapter 3. Sensitivity of Polar Amplification to Varying Insolation Conditions

As introduced in Chapter 1.1 and 1.2, most state-of-the-art climate models disagree on the magnitude and spatial pattern of polar amplification. Many previous studies have been trying to disentangle the feedback mechanism for a better understanding of Arctic climate change, but the processes are hard to quantify explicitly. In this chapter, we will adopt targeted idealized model simulations for understanding the fundamental physical process of polar amplification. Then, by applying the radiative kernel technique introduced in Chapter 2.2 and the cloud locking experiments, we will identify the important role of cloud radiative response on polar amplification.

3.1. Background

Various feedback mechanisms within the climate system are suggested to contribute to polar amplification. Among them, the surface albedo feedback is widely accepted to play a leading role (Arrhenius, 1896; Manabe and Wetherald, 1975; Screen et al., 2012). With global warming, melting of sea ice and snow decreases the surface albedo, enhancing the absorption of solar radiation, thereby contributing to warming the polar surface. However, the polar surface warming response is amplified even in simulations with no surface albedo feedback (Alexeev et al., 2005; Langen et al., 2012). This indicates that mechanisms other than the locally induced surface albedo feedback are at play, such as changes in atmospheric energy transport (Alexeev et al., 2005; Cai, 2005; Chung and Räisänen, 2011), cloud feedbacks (Vavrus, 2004), and lapse rate feedback (Pithan and Mauritsen, 2014).

The lapse rate feedback associated with the vertical profile of atmospheric warming has been proposed to be the dominant contributor to polar amplification (Manabe and Wetherald, 1975; Graversen and Wang, 2009; Pithan and Mauritsen, 2014). In the tropics with deep convection, the vertical temperature profile closely follows a moist adiabat, thereby producing greater warming in the upper troposphere than at the surface. This top-heavy warming profile is effective at radiating longwave radiation to space, so that less surface warming is needed to balance a given radiative forcing. In the polar region, moist convection is inhibited due to a large static stability. The inversion layer keeps near-surface air from being mixed with the air aloft, leading to a bottom-heavy warming profile that is ineffective at producing large outgoing longwave radiation, hence, requiring a larger surface warming to balance a given radiative forcing (Manabe and Wetherald, 1975; Tjernström and Graversen, 2009; Graversen and Wang, 2009). Since the lapse rate feedback is negative in the tropics and positive in the polar region, it contributes to inducing the polar amplified surface warming pattern. Note, however, that the high-latitude lapse rate feedback needs to be distinguished from the tropical lapse rate feedback. The vertical temperature profile in the tropical troposphere is determined locally by a moist adiabat, whereas the static stability of high latitudes can be modulated by changes in the atmospheric energy transport due to some remote radiative forcing. This sensitivity of high-latitude lapse rate to forcing is

ULSAN NATIONAL INSTITUTE OF SCIENCE AND TECHNOLOGY

explained in terms of a forcing-dependent lapse rate feedback (Cronin and Jansen, 2016).

Other mechanisms for polar amplification include the longwave radiative feedback associated with an increase in water vapor and cloud cover (Winton, 2006; Graversen and Wang, 2009). Complications arise as cloud cover affects the efficacy of surface albedo feedback (Kay et al., 2012). A reduced cloud cover enhances the albedo feedback (Hofer et al., 2017), whereas the effect of changes in surface albedo in the overcast regions would be obscured by reflective clouds. Enhanced poleward heat transport by the atmosphere and/or ocean has also been identified as a factor that contributes to the polar surface warming amplification (Holland and Bitz, 2003; Cai, 2005; Chung and Räisänen, 2011). To examine the relative contribution of each mechanism, various feedback analysis has been applied (Taylor et al., 2011a; 2011b; Pithan and Mauritsen, 2014). Also, a number of studies utilize idealized experiments with models of varying complexity from simple energy balance models or box models (Alexeev et al., 2005; Cai, 2005; Merlis and Henry, 2017) to comprehensive GCMs (Chung and Räisänen, 2011; Graversen and Burtu, 2016). However, it is still difficult to cleanly isolate processes controlling polar amplification because multiple mechanisms act locally as well as interact remotely with each other (Graversen et al., 2014).

The seasonal differences in multiple mechanisms give rise to a pronounced seasonality in the polar surface warming. Both models and observations feature the largest polar surface warming in winter and smallest in summer (Wetherald and Manabe, 1981; Lu and Cai, 2009; Bintanja et al., 2012; Sejas et al., 2014). This is counterintuitive as sea ice reductions and the associated ice albedo feedback are strongest in summer. Instead, it is explained by an increase in winter oceanic heat loss in response to the loss of summer ice cover (Screen and Simmonds, 2010; Cohen et al., 2012). Reduced sea ice extent in summer enhances the solar absorption at the subsurface ocean (Perovich et al., 2008), which is released to the atmosphere in autumn and winter by radiative and turbulent fluxes because the air temperatures are lower than the ocean surface (Serreze et al., 2009; Inoue and Hori, 2011). An alternative explanation for the amplified polar winter warming is that the surface thermal inversion during cold seasons intensifies the polar surface warming through downward longwave radiation (Bintanja et al., 2012).

The pronounced seasonality in polar amplification casts doubt on the validity of idealized studies under the annual-mean insolation. For instance, Alexeev et al. (2005) demonstrate clear polar amplification in the absence of surface albedo feedback under annual-mean insolation. However, the experiments with a seasonal cycle in Feldl et al. (2017a), where the strength of the surface albedo feedback is manipulated, suggest that surface warming is relatively uniform in the experiment with the negligible surface albedo feedback. The contrasting results raise the question of the role of the inclusion of a seasonal cycle on polar amplification. A series of seminal work by Manabe indicate that the polar amplification is less pronounced in the simulation with a seasonal cycle than the simulation with annual-mean insolation because of the lack of surface albedo feedback during the summer (Wetherald and

ULSAN NATIONAL INSTITUTE OF SCIENCE AND TECHNOLOGY

Manabe 1981; Manabe et al., 1991; 1992). In this study, we attempt to understand the disparate mechanisms of polar amplification under various insolation conditions in the absence of a surface albedo feedback.

3.2. Data and methodology

We employ an atmospheric general circulation model, AM2 developed at the Geophysical Fluid Dynamics Laboratory (GFDL), which participated in Coupled Model Intercomparison Project (CMIP) 3 and CMIP5 (Freidenreich et al., 2004). The model is run at a horizontal resolution of 2 latitude x 2.5 longitude and 24 vertical levels. The atmosphere is coupled to an aquaplanet slab ocean with a depth of 10 m. The surface temperatures are allowed to drop below freezing temperature without forming any sea ice, thus disabling the surface albedo feedback. The reference integration with 348 ppm of CO_2 concentration is perturbed by a CO_2 doubling. Both reference ($1xCO_2$) and perturbed ($2xCO_2$) integrations are forced by different insolation conditions: perpetual equinox (denoted as EQN), annual-mean insolation (denoted ANN), or with a seasonal cycle (denoted as SEA). In SEA, the eccentricity is set to zero so that the Earth has a perfectly circular orbit with no perihelion. All experiments are run for 45 years with 20 years of spin up.

3.2.1. Prescribed cloud radiative feedback

As previous studies pointed to the important roles played by clouds, SEA and ANN are simulated with prescribed clouds in order to cleanly examine the effect of cloud adjustments on polar amplification. A randomly chosen 1-year time series of the 3D cloud water mixing ratio, cloud ice mixing ratio, and cloud fractional area in the respective $1xCO_2$ experiment is prescribed at every 3 hours in the radiative scheme for both $1xCO_2$ and $2xCO_2$ experiments. The prescribed cloud experiments of SEA and ANN are denoted as SEAFC and ANNFC, respectively. In addition, we perform SEA with clouds prescribed over a limited area to contrast the role of cloud radiative effect in the tropics and the polar region. The experiment with prescribed clouds over 30°S-30°N is denoted as SEAFC_TRO, and that with prescribed clouds poleward of 60°S/N as SEAFC_POL.

Experiment	EQN	SEA	SEAFC	SEAFC_POL	SEAFC_TRO	ANN	ANNFC
Insolation	Perpetual equinox	Seasonal cycle	Seasonal cycle	Seasonal cycle	Seasonal cycle	Annual mean	Annual mean
Prescribed cloud	None	None	90°S-90°N	Poleward of 60°S/N	30°S-30°N	None	90°S-90°N

Table 3.1. Overview of all experiments. Unless indicated otherwise, clouds evolve freely

ULSAN NATIONAL INSTITUTE OF SCIENCE AND TECHNOLOGY

3.2.2. Radiative kernel technique in slab ocean model

To examine the relative importance of various feedbacks, we apply the radiative kernel method of calculating climate feedbacks (Soden et al., 2008; Feldl and Roe, 2013a; 2013b). The change in TOA net radiation (ΔR) can be decomposed into climate feedbacks and forcing by a Taylor series expansion in surface temperature change (ΔT_s):

$$\Delta R = \sum_i \lambda_i \Delta T_s + \Delta R_f + \varepsilon \quad (3.1)$$

All terms in Eq. (3.1) are functions of latitude and month. The first term on the right-hand side represents the combined climate feedbacks where λ is calculated from radiative kernels in Feldl et al. (2017a). It includes Planck, lapse rate, water vapor, and cloud feedbacks. The R_f term represents the radiative forcing of a CO_2 doubling. Among various radiative forcing definitions, we use the fixed-SST forcing method (Hansen et al., 2005; Feldl and Roe, 2013b). For example, the R_f term for prescribed cloud experiments (SEAFC) is calculated with the SST prescribed to the zonal-mean monthly profiles of SEAFC and clouds prescribed to their zonal-mean profiles of SEA at every 3 hours as in the prescribed cloud experiments. The residual ε is higher-order terms in the Taylor series expansion, which reflect nonlinearities within individual process or nonlinear interactions among different processes. Analysis on the climate feedbacks is offered in Section 3.3.4.

3.3. Results

3.3.1. Polar amplification in aquaplanet

Figure 3.1a compares the surface temperature response to 2xCO_2 in EQN, ANN, and SEA. The three aquaplanet experiments with different insolation conditions exhibit vastly different global climate sensitivity, defined as the global mean surface temperature response to 2xCO_2: 3.1 K, 2.3 K, and 2.5 K in EQN, ANN, and SEA, respectively. All experiments exhibit a lower global climate sensitivity than that in Feldl and Roe (2013a) of 4.7 K due to the lack of a surface albedo feedback. The higher global climate sensitivity in EQN relative to the other two experiments results from stronger polar amplification. In EQN, the surface poleward of 70° is warmed by 6.1 K, 70 % more than the global-mean response, whereas the contrast is only 20 % in ANN. In SEA, the latitudinal profile of the surface warming response is nearly flat, indicative of no polar amplification. This stark contrast is influenced by differences in the vertical temperature profiles at high latitudes in the respective control climates due to the varying insolation condition.

ULSAN NATIONAL INSTITUTE OF SCIENCE AND TECHNOLOGY

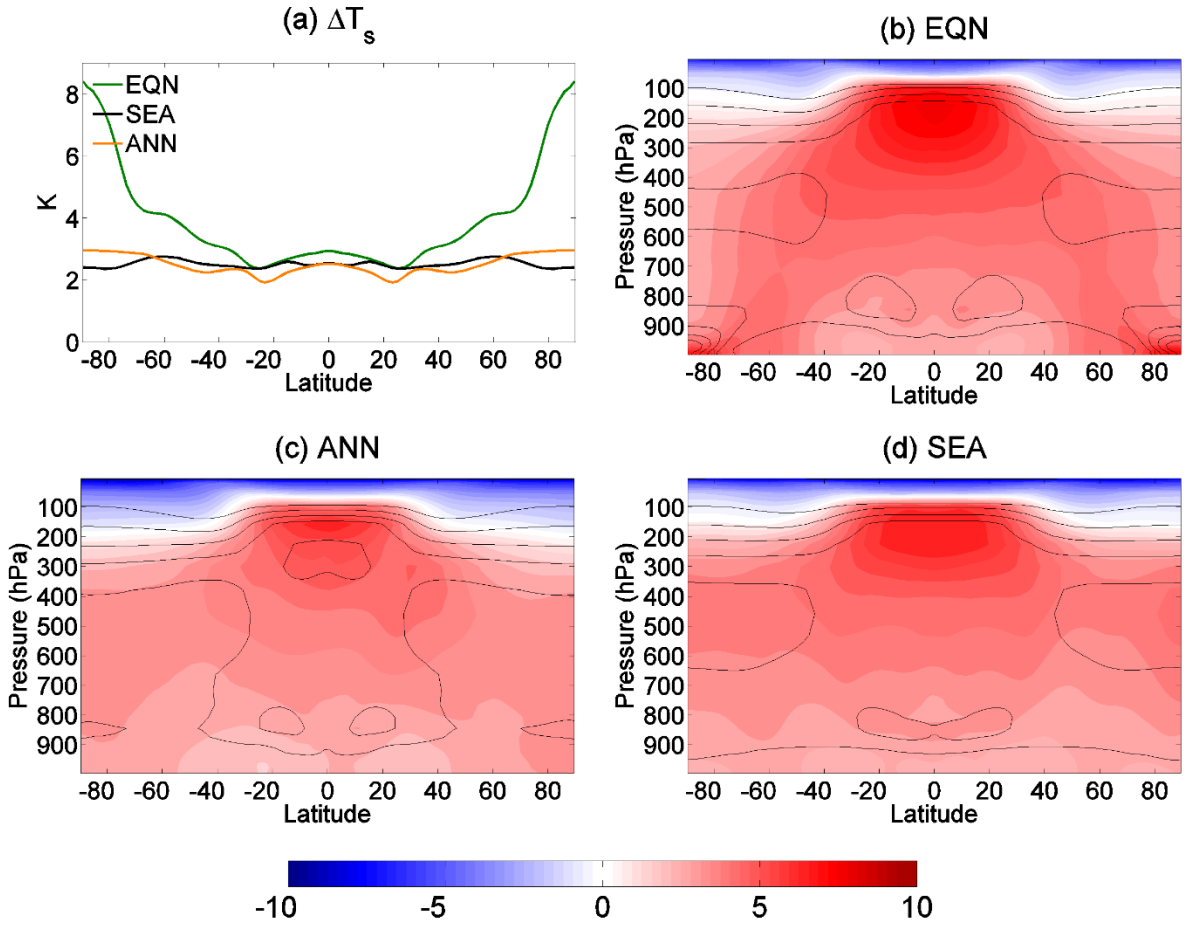

Figure 3.1. (a) Zonal- and time-mean surface temperature response (K) in 2xCO_2. (b-d) Shading indicates the zonal- and time-mean temperature response (K) in 2xCO_2 and contours indicate the static stability (with an interval of 0.4℃/100m) in 1xCO_2, defined as $\frac{d\theta}{dz} = -\frac{\rho g}{(RT)} \times \frac{d\theta}{dp}$ following Graversen and Wang (2009), in (b) EQN, (c) ANN, and (d) SEA.

ULSAN NATIONAL INSTITUTE OF
SCIENCE AND TECHNOLOGY

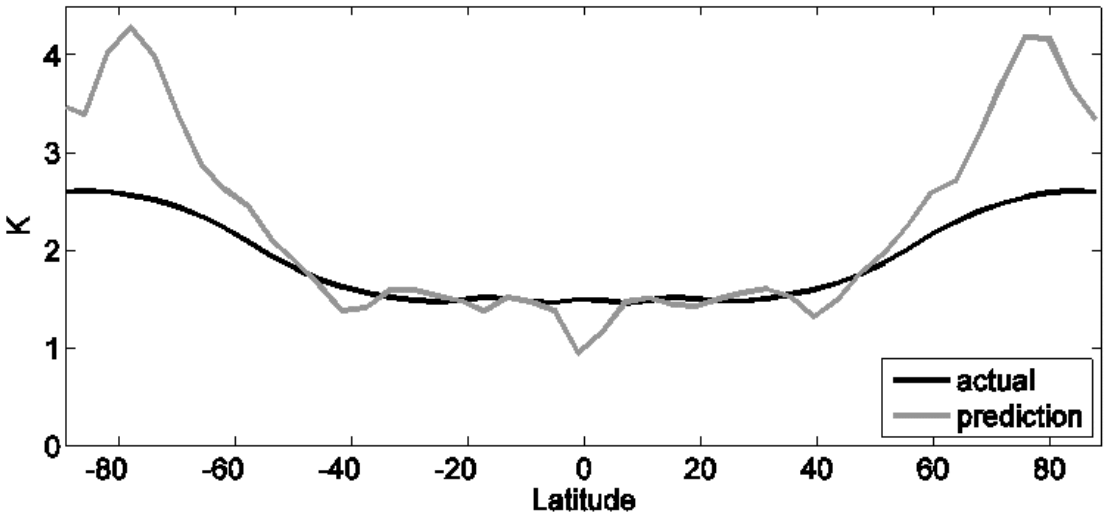

Figure 3.2. A comparison of actual surface temperature response in SEAFC (black) and its prediction by removing the cloud feedback contribution (blue in Fig. 3.9a) from the surface temperature response in SEA (gray).

The polar region in EQN exhibits a large static stability near the surface (Fig. 3.1b) because of the year-round near zero solar radiation reaching the polar region under equinox. The large stability in the boundary layer in EQN leads to a surface trapped warming, hence, more amplified than in other experiments through the positive lapse rate feedback (Fig. 3.2). In contrast, both ANN and SEA do not exhibit any maxima in static stability near the surface in the polar region (Figs. 3.1c-d), leading to a slightly negative lapse rate feedback there (Fig. 3.2). For reference, Figure 3.2 compares the contribution of lapse rate feedback to the surface temperature response in the three experiments. It is the distinctive insolation pattern in EQN that greatly stabilizes the polar region to induce a bottom-heavy structured warming, resulting in strong polar amplification even without any sea ice. On the other hand, the ANN and SEA experiments in the absence of surface albedo feedback exhibit a small static stability in the polar region that leads to negative lapse rate feedback. In more comprehensive models with sea ice, the cold sea-ice cover gives rise to a highly stable state, thereby trapping heat near the surface and enhancing the lapse rate feedback. As a result, the bottom-heavy warming profile is a common feature associated with polar amplification (Serreze et al., 2009; Screen et al., 2012).

Note that the observed inversion strength and temperature in the polar region are closer to those in EQN, rather than ANN or SEA (Pavelsky et al. 2011). Moreover, the observed polar atmospheric state resembles the EQN experiment more frequently than the ANN and SEA experiments, following the categorization of polar atmospheric regimes based on the lower tropospheric stability using satellite data in Taylor et al. (2015): the EQN experiment fits in the highly stable regime (whose frequency of

ULSAN NATIONAL INSTITUTE OF SCIENCE AND TECHNOLOGY

occurrence is 0.36) whereas the ANN and SEA experiments fit in the stable regime (whose frequency of occurrence is 0.28). However, it is worth noting that EQN resembles the observed state for the wrong reason: the static stability in EQN is large due to the year-round near zero solar radiation reaching the polar region whereas sea ice is responsible for the very stable polar region in the real world.

The polar warming patterns in ANN and SEA, with a peak warming in the mid-troposphere, are distinguished from those in EQN (Figs. 3.1b-d). In ANN and SEA, the warming response cannot be trapped near the surface, in the absence of any sea ice and surface albedo feedback, due to a weaker stability in the boundary layer compared to EQN. Even the stability in the winter time of SEA is not large enough to trap warming near the surface. Instead, the polar warming response is peaked in the mid-troposphere and is dispersed vertically, inducing a weak polar amplified warming at the surface. Previous work has suggested that the mid-tropospheric warming in the polar region is caused by an increase in atmospheric energy transport from lower latitudes (Graversen and Burtu, 2016; Screen et al., 2012). This assertion is supported by our result (Fig. 3.3a) that shows a high correlation of 0.67 between the anomalous total atmospheric energy transport (AET) at 70° and the mid-tropospheric warming magnitude averaged poleward of 70°. Note that the total AET is calculated indirectly from the energy budget for an atmospheric column: $\int_{-\frac{\pi}{2}}^{\varphi}(2\pi a^2 \cos\varphi\, R)\, d\varphi$ where φ is latitude, a is radius of the Earth, and R is the net TOA radiation. The mid-tropospheric warming can contribute to warming the polar surface through increasing the downward longwave radiation at the surface (Figs. 3.3c-d). An overall increase in the total AET at high latitudes is accomplished by an increase in latent heat transport by transient eddies (Fig. 3.3b). Partly compensating the enhanced total AET is the decrease in dry static energy transport resulting from a flattened temperature gradient.

For reference, most CMIP3 models project an increase in total AET equatorward of 70°N, but the models do not agree on the sign poleward of 70°N, despite a robust increase in the latent energy transport by transient eddies with global warming (Hwang et al., 2011). The increase in latent energy transport is expected because of an enhanced meridional humidity gradient, following the Clausius-Clapeyron relation (C-C relation), since water vapor increases preferentially in low latitudes due to an exponential increase of saturated humidity with temperature (Alexeev et al., 2005; Frierson et al., 2007; Graversen and Burtu, 2016). Uncertainty in the sign of total AET at high latitudes originates from a large multi-model spread in the degree of polar amplification. Models with stronger polar amplification exhibit a larger reduction in dry static energy transport, which in cases may overcompensate the increased latent energy transport, resulting in a reduced high-latitude total AET. Among CMIP3 models, the GFDL model, on which our model is based, is the one that projects the largest increase in the total AET throughout the globe. Feldl et al. (2017b) clearly demonstrates that the strength of surface albedo feedback modulates the ratio of latent to dry static energy transport in the extratropics. In the case with the strongest surface albedo feedback, the total AET is reduced due to an overcompensation by the

ULSAN NATIONAL INSTITUTE OF SCIENCE AND TECHNOLOGY

decrease in dry static energy transport resulting from strong polar amplification. In the case with the moderate to weak surface albedo feedback, the total AET increases due to the dominance of the increase in latent energy transport over the decrease in dry static energy transport. Our model that features no surface albedo feedback gives rise to an increase in the total AET in the extratropics, consistent with the low surface albedo feedback case in Feldl et al. (2017b).

The mid-tropospheric polar warming, in particular, is suggested to originate from the midlatitude near-surface warming that propagates along climatological moist isentropes (Laliberté and Kushner 2014). Our results show a strong linear relationship between the 850 hPa warming response averaged over 45-65° and the mid-tropospheric warming averaged poleward of 70° (R=0.85). Another origin for the mid-tropospheric polar warming could be warm equatorial air that is advected across the storm tracks by synoptic eddies and that subsides over the poles (Pauluis et al., 2008). The mid-tropospheric polar warming in our experiments is also strongly correlated with the warming response in the upper troposphere (100-300 hPa) equatorward of 20° (R=0.92). A subsequent study is needed to distinguish the contribution from the equatorial upper-troposphere and midlatitude near-surface to polar mid-tropospheric warming.

In summary, in an aquaplanet setup with no surface albedo feedback, the equinox condition gives rise to a highly stable boundary layer in the polar region to form a bottom-heavy structured warming, resulting in strong polar amplification through the positive lapse rate feedback. In contrast, under annual-mean or seasonally varying insolation, the static stability in the polar region is so small that the lapse rate feedback is negative. However, the mid-tropospheric polar warming, which possibly originates from the midlatitude near-surface warming and/or the tropical upper-tropospheric warming, may contribute to forming a weak polar amplification indirectly through the downward longwave radiation. In the next section, we demonstrate that the contrasting cloud response under the annual-mean and seasonally varying insolation is responsible for the varying degree of polar amplification in the two cases. In section 3.4, the role of atmospheric energy transport on polar amplification will be discussed more extensively by using the radiative kernel technique.

ULSAN NATIONAL INSTITUTE OF SCIENCE AND TECHNOLOGY

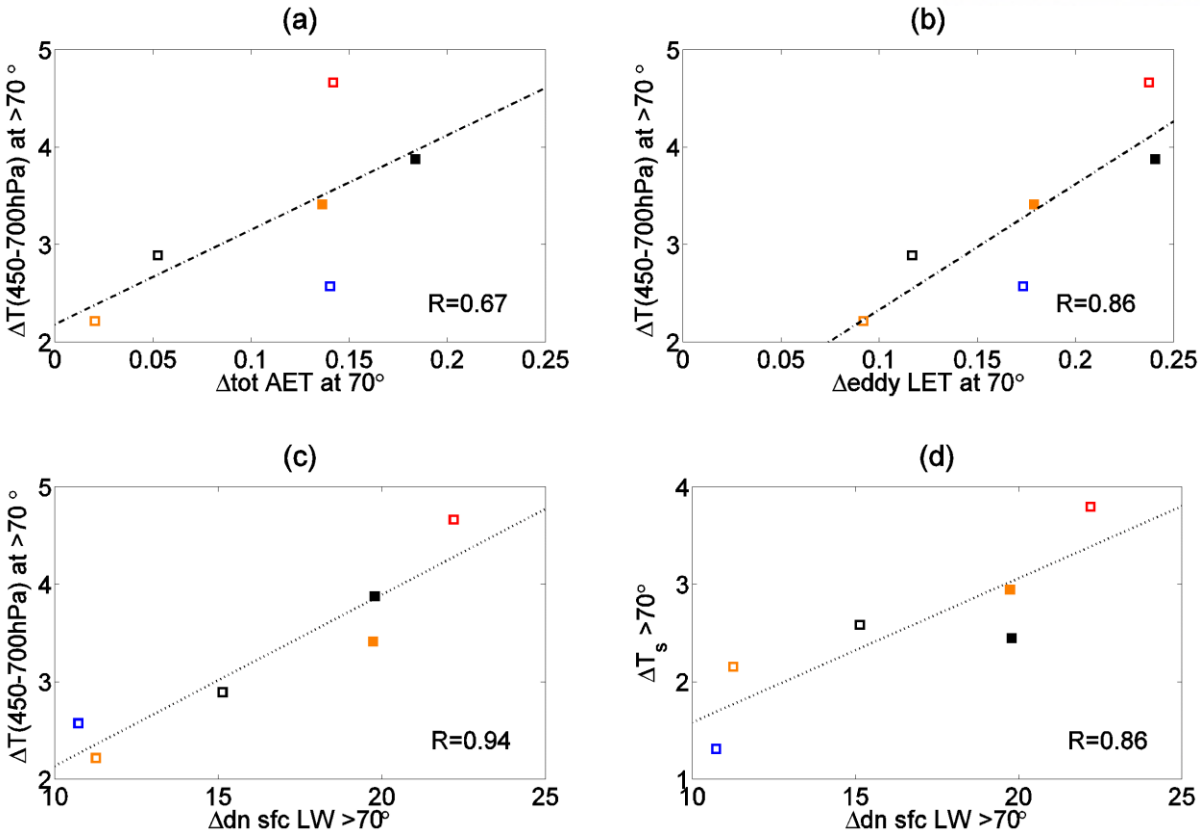

Figure 3.3. Changes in mid-tropospheric temperature (450-700 hPa) poleward of 70° (K) versus changes in (a) atmospheric energy transport at 70°, and (b) eddy latent energy transport at 70° (PW). Changes in downward longwave radiation at the surface poleward of 70° (W/m^2) versus changes in (c) mid-tropospheric temperature (450-700 hPa) and (d) surface temperature poleward of 70° (K). Simulations are color coded as in the legend of Fig. 3.4a. The open squares indicate the models with prescribed CRE.

ULSAN NATIONAL INSTITUTE OF SCIENCE AND TECHNOLOGY

3.3.2. Cloud response

In spite of the identical time-mean insolation, the degree of polar amplification is different between the models with annual-mean (ANN) and seasonally varying (SEA) insolation. To quantify the degree of polar amplification, we calculate polar amplification index (PAI), defined as the increase in surface temperature poleward of 70° normalized by the change in global mean surface temperature. The PAI is 1.19 in ANN and 1.02 in SEA.

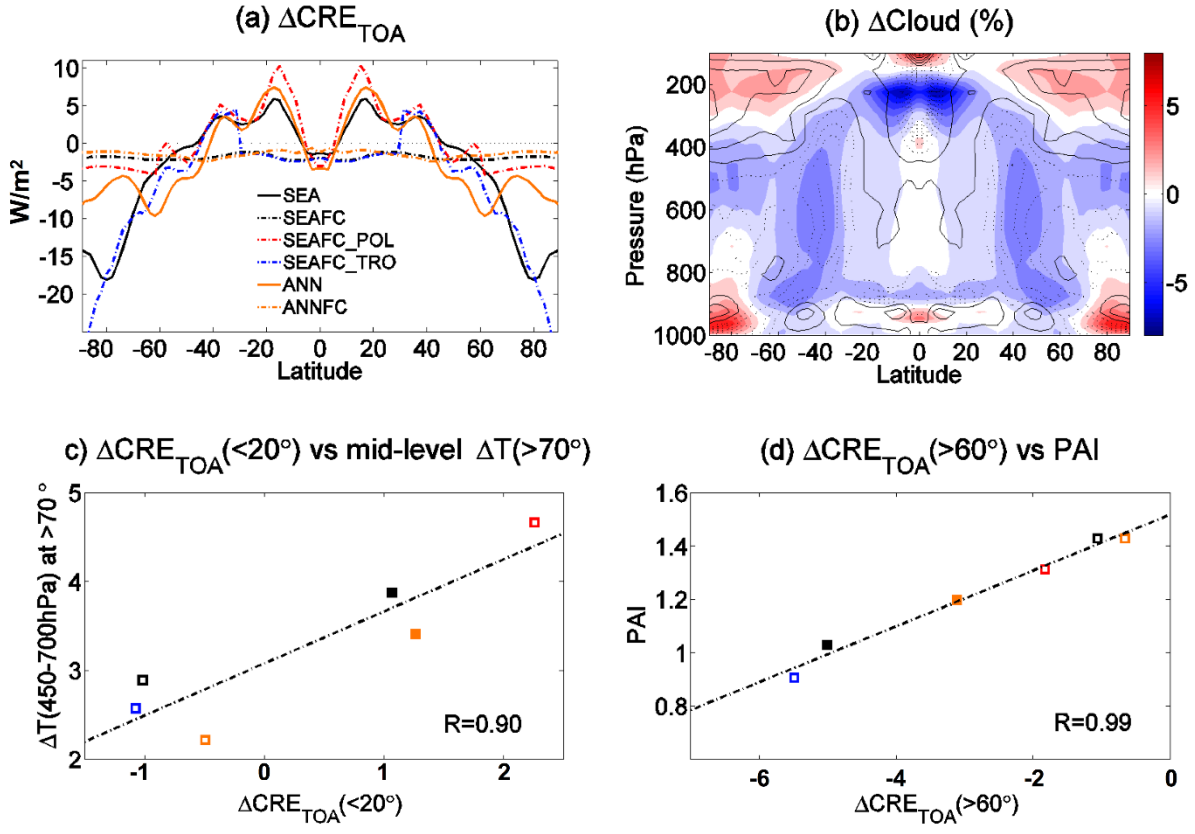

Figure 3.4. Zonal- and time-mean responses to 2xCO_2 in (a) cloud radiative effects at TOA (CRE_{TOA}; W/m^2) and (b) cloud fraction (%) in SEA (shading) and ANN (contour; interval is 1%). (c) Changes in mid-tropospheric temperature (450-700 hPa) poleward of 70° (K) versus area-mean CRE_{TOA} changes in the tropics (<20°; W/m^2). (d) Polar Amplification Index (PAI; unitless) versus area-mean CRE_{TOA} changes poleward of 60° (W/m^2). Simulations are color coded as in the legend of panel (a). The open squares indicate the models with prescribed CRE.

ULSAN NATIONAL INSTITUTE OF SCIENCE AND TECHNOLOGY

We find differences in the changes in top-of-atmosphere cloud radiative effects (CRE_{TOA}) between ANN and SEA (Fig. 3.4a; orange and black solid lines). In low latitudes, both models exhibit positive CRE_{TOA} changes, due to a reduction of overall cloud amount (Fig. 3.4b). In contrast, high latitudes in both models exhibit negative CRE_{TOA} changes due to an increase in low-level cloud amount, associated with increased relative humidity. However, the mid-to-upper level cloud amount decreases since the relative humidity decreases there in association with the mid-tropospheric peak warming. The cloud amount changes in Figure 3.4b are consistent with previous studies (Vavrus, 2004; Langen et al. 2012; Feldl et al. 2017a). Increased liquid water path over mid to high latitudes associated with warming can also contribute to enhancing the negative CRE_{TOA} in the extratropics (Ceppi et al., 2016). SEA exhibits a larger CRE_{TOA} cooling response poleward of 65° relative to ANN, which is consistent with the weaker polar amplification in SEA.

To confirm that the differences in CRE_{TOA} changes are responsible for the varying PAI in ANN and SEA, we examine a corresponding prescribed cloud model that is described in Section 2.1. When clouds are prescribed in SEA (denoted as SEAFC), the whole globe is warmed less except near the poles (Fig. 3.5a; black solid and dash-dot lines). The contrast is largest in the tropics, leading to strong polar amplification in SEAFC (PAI = 1.42). Stronger polar amplification in SEAFC relative to SEA can be also identified by comparing Figure 3.1d with Figure 3.5b. The CAM3 aquaplanet simulation with a seasonal cycle in Langen et al. (2012) that has weak cloud feedbacks exhibits a similar degree of polar amplification to our SEAFC. The prescribed cloud model of ANN (denoted as ANNFC) exhibits the same degree of polar amplification as SEAFC with PAI = 1.42. The latitudinal profile of surface temperature response between ANNFC and SEAFC is indeed very similar (Fig. 3.5a; orange dash-dot and black dash-dot lines). Thus, the prescribed cloud models help to confirm that the contrast in the degree of polar amplification in ANN and SEA is the result of differences in the CRE_{TOA} response. The reason for the differences in the CRE_{TOA} response in ANN and SEA is discussed in Section 3.3.

ULSAN NATIONAL INSTITUTE OF SCIENCE AND TECHNOLOGY

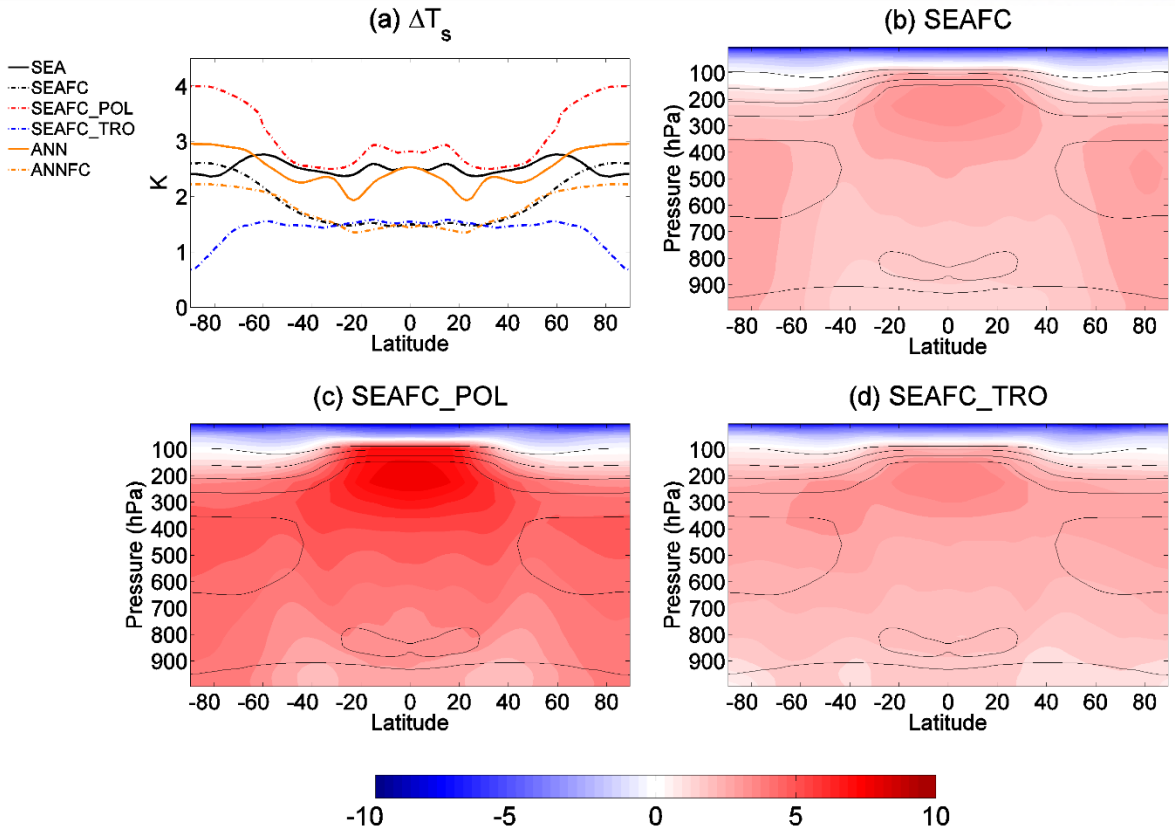

Figure 3.5. (a) Same as in Figure 3.1a, but for different simulations as noted in the legend (b-d)**.** Same as in Figure 3.1b-d, but for (b) SEAFC, (c) SEAFC_POL, and (d) SEAFC_TRO.

To better understand the role of cloud response on polar amplification, we additionally examine a partially prescribed cloud version of SEA. When clouds are allowed to respond in the tropics while being prescribed in the polar region (SEAFC_POL), the tropical surface warming is enhanced relative to SEAFC (Fig. 3.5a; red dash-dot and black dash-dot lines) as the CRE_{TOA} changes cause warming in the low latitudes (Fig. 3.4a). The enhanced tropical warming leads to strong polar amplification, despite an absence of surface trapped warming (Fig. 3.5c). Rather, there is a mid-tropospheric peak in the polar warming as in SEA and ANN that is associated with weak polar amplification. Thus, one can deduce that it is the negative CRE_{TOA} change in the polar region that counteracts polar amplification in SEA and ANN. Conversely, when the clouds are allowed to respond in the polar region while being prescribed in the tropics (SEAFC_TRO), the degree of tropical surface warming is similar to SEAFC but the polar surface warming is significantly damped (Fig. 3.5a; blue dash-dot and black dash-dot lines) due to the negative CRE_{TOA} change in the polar region (Fig. 3.4a). SEAFC_TRO presents only a weak upper tropospheric warming in the tropics (Fig. 3.5d), which then leads to a weak mid-tropospheric warming at the pole that is unable to cause any polar amplification at the surface. Indeed, the PAI in SEAFC_TRO is smaller than 1 (PAI = 0.90). Although the CRE response in the polar region is negative

ULSAN NATIONAL INSTITUTE OF SCIENCE AND TECHNOLOGY

in both SEA and SEAFC_TRO, SEA exhibits a larger polar amplification than SEAFC_TRO because of positive CRE_{TOA} change in the tropics.

The partially prescribed cloud models add insight into the mechanism of polar amplification in the absence of surface albedo feedback. In response to $2xCO_2$, the tropical surface warming is amplified by the positive CRE_{TOA} changes. The warming response in the tropics is then maximized in the upper troposphere due to the moist adiabatic adjustment. In proportion to the magnitude of tropical warming, the poleward atmospheric energy transport increases to cause the mid-tropospheric polar warming. Hence, the CRE_{TOA} increase in the tropics is highly correlated with the mid-tropospheric polar warming (Fig. 3.4c), which in turn contributes to polar surface warming through downward longwave radiation. The polar surface warming is, however, partially diminished by negative CRE_{TOA} changes in high latitudes. In our model, the negative local CRE_{TOA} changes overwhelm the effect of mid-tropospheric polar warming, thereby completely damping polar amplification in either SEA or ANN. Indeed, Figure 3.4d shows that a larger negative polar CRE_{TOA} change is accompanied by weaker polar amplification. The CRE_{TOA} changes poleward of 60° are almost perfectly correlated with the PAI. In contrast, the tropical CRE_{TOA} change correlates poorly with the PAI ($R = -0.02$) since the tropical CRE_{TOA} change has only an indirect impact on polar amplification through the mid-tropospheric polar warming. Another potential reason for the poor correlation is that the tropical CRE_{TOA} change accompanies warming not only in the polar region but also in the tropics, hence, it is difficult to create a large change in the meridional gradient. Therefore, the polar CRE_{TOA} change is a more controlling factor for the degree of polar amplification than the tropical CRE_{TOA} change.

3.3.3. Seasonality of polar amplification

To identify what causes the differences in the CRE response between ANN and SEA, we turn to the monthly response of SEA. In the polar region, the low-level cloud (defined as 680-1000 hPa) amount increases in the warm season (i.e., August-September-October for the Northern Hemisphere (NH)), while it decreases in the cold season (i.e., February-March-April for NH) (Fig. 3.6a). The low-level cloud amount reduction in the cold season is somewhat overestimated, but the overall feature is consistent with the CMIP3 ensemble projections (Vavrus et al., 2009). Our model calculates the cloud amount based on relative humidity following the prognostic scheme of Tiedtke (1993). Hence, the vertical profile of cloud fraction changes closely follows that of relative humidity (Figs. 3.7a-b). The relative humidity in the polar region increases below 600 hPa in the warm season whereas it decreases throughout the troposphere, except near the surface, in the cold season (Fig. 3.7b). This contrast results from the distinctive seasonality in the vertical warming pattern (Fig. 3.7c), which possibly is caused by the seasonal differences in the mean circulation pattern. A strong descending motion in the cold season lowers the altitude of mid-tropospheric peak in polar warming and spreads the warming response to lower level (Fig. 3.7c). The consequent lower tropospheric warming in the polar region decreases the

ULSAN NATIONAL INSTITUTE OF
SCIENCE AND TECHNOLOGY

relative humidity, leading to a reduction of low-level cloud amount. Conversely, a weak ascending motion in the warm season elevates the altitude of the mid-tropospheric peak in polar warming, spreading the warming response to higher level (Fig. 3.7c). Despite a smaller warming response in the warm season below 450 hPa, the amount of specific humidity increase is larger in the warm season than the cold season due to the C-C relation (Fig. 3.7d), which contributes to an increase of relative humidity there. As a result, the polar region exhibits an increase in the low-level warm season cloud amount. Partly due to the nonlinear relationship between vapor pressure and temperature, the increase of low-level cloud amount in the warm season is greater than the decrease in the cold season, so that the annual-mean low-level cloud amount increases in the polar region in SEA (Fig. 3.6a). In contrast, the time-mean response of ANN exhibits a reduction of the low-level cloud amount in the polar region (Fig. 3.6a).

ULSAN NATIONAL INSTITUTE OF
SCIENCE AND TECHNOLOGY

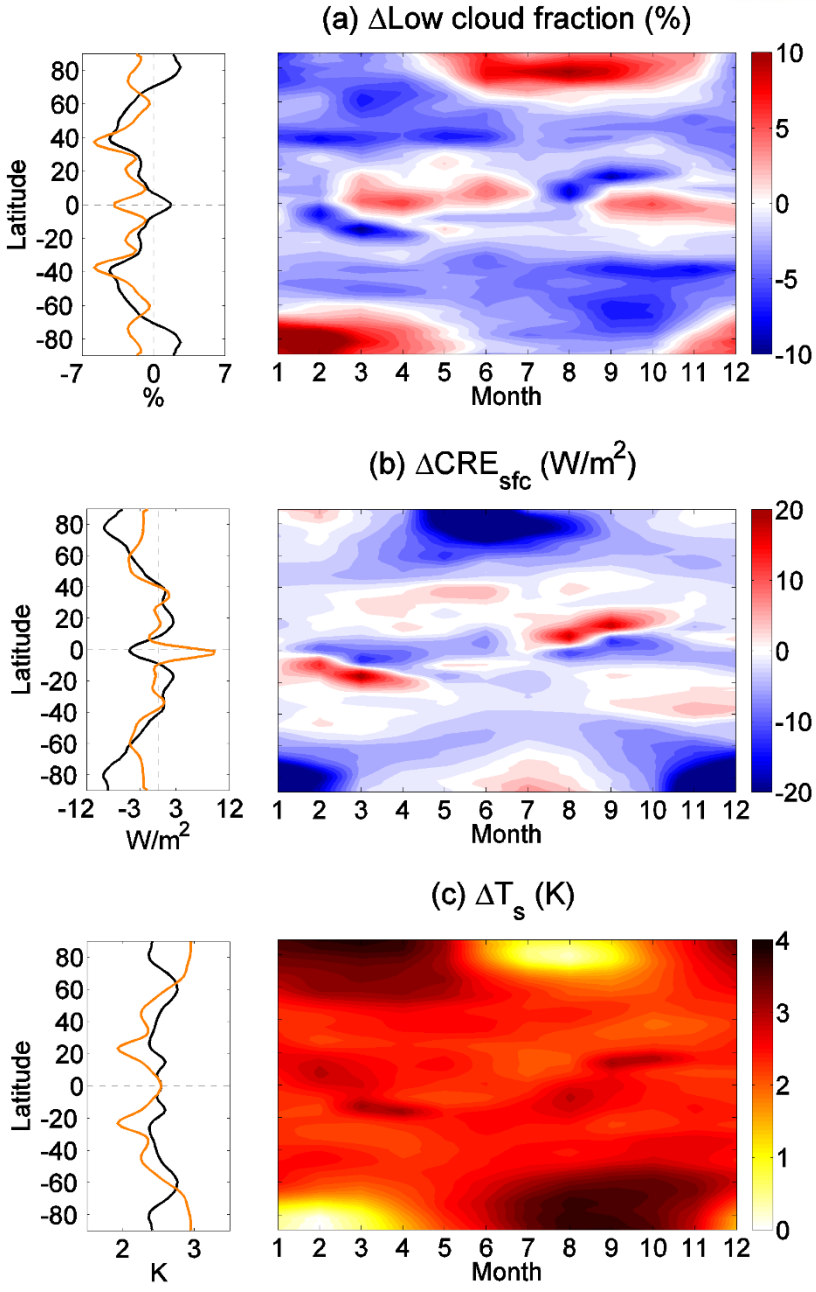

Figure 3.6. (Top) low cloud fraction (%), (middle) cloud radiative effects at the surface (W/m^2), and (bottom) surface temperature (K). In the left column, black and orange lines are the annual averages of zonal-mean responses for SEA and ANN, respectively. The right column indicates the monthly zonally averaged responses in SEA.

ULSAN NATIONAL INSTITUTE OF
SCIENCE AND TECHNOLOGY

As a result of the increase in low-level cloud amount in the polar warm season, there is a large negative change in CRE at the surface (denoted as CRE_{sfc}) that counteracts the polar surface warming response (Fig. 3.6b). The negative CRE_{sfc} response in the northern high latitudes peaks from May to July when the greatest insolation reaches the North Pole. Changes in cloud amount in the dark months have only a limited impact on radiative fluxes, hence, the increase of northern high-latitude low-level cloud amount from September to November is accompanied by negligible CRE_{sfc} response (Fig. 3.6a-b). The large seasonality in the polar CRE_{sfc} response results in polar surface warming with a distinct seasonality (Figs. 3.6c and 8). The polar surface warming response lags the CRE_{sfc} response by two to three months due to the time it takes to heat up the ocean mixed layer. The monthly variation of polar surface warming in Figure 3.6c indicates that the warming is most amplified in cold season (i.e., March in the North Pole and August in the South Pole) while being most damped in warm season (i.e., August in the North Pole and February in the South Pole). That is, the largest negative tendency of surface temperature response exists in June in the North Pole and November in the South Pole, respectively, corresponding to the timing of the largest negative CRE_{sfc} response. This is because the CRE_{sfc} response corresponds to the time tendency of surface temperature response.

ULSAN NATIONAL INSTITUTE OF
SCIENCE AND TECHNOLOGY

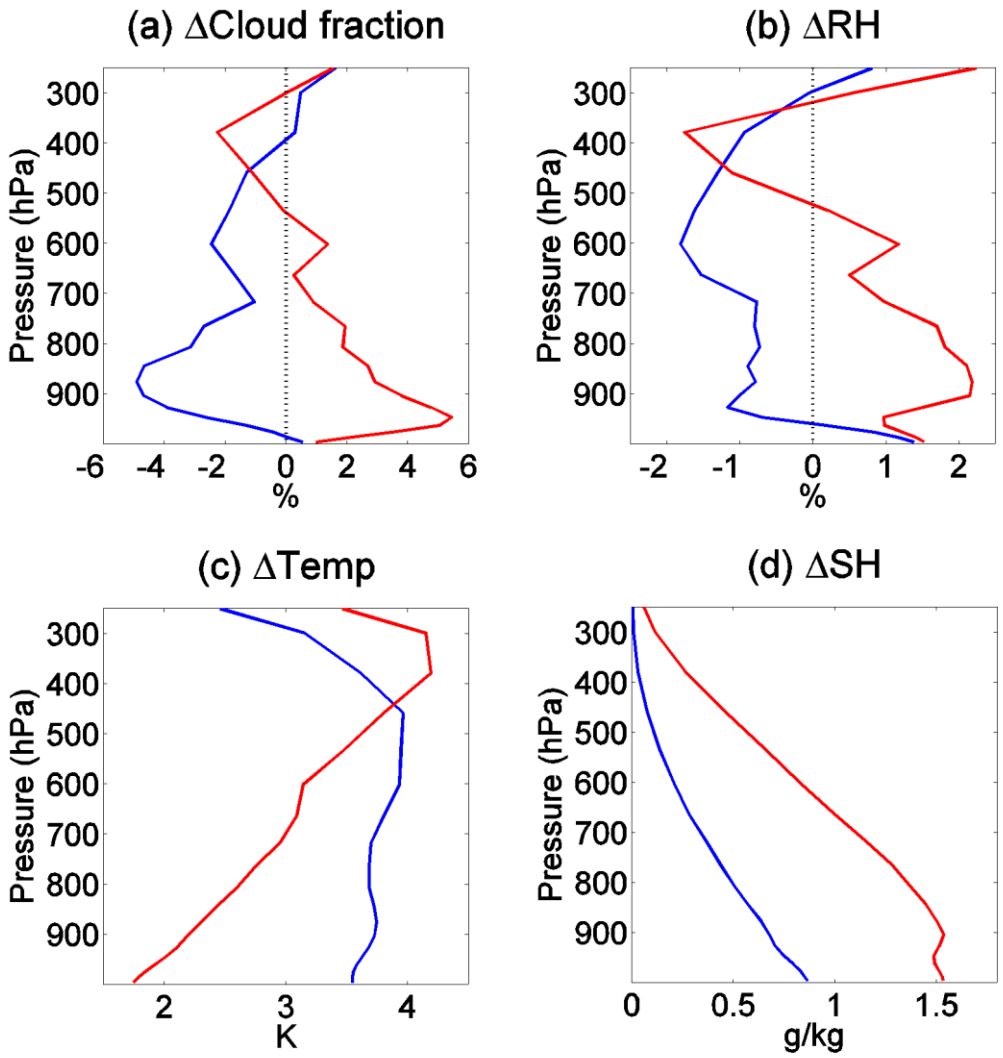

Figure 3.7. Changes in (a) cloud fraction (%), (b) relative humidity (%), (c) temperature (K), and (d) specific humidity (g kg^{-1}) averaged over poleward of 60°N for the August-September-October (red), and February-March-April (blue) in SEA.

ULSAN NATIONAL INSTITUTE OF SCIENCE AND TECHNOLOGY

Comparison of monthly PAI between SEA and SEAFC in Figure 3.8 clearly shows that polar amplification is weakest in the warm season in SEA due to the large negative change in CRE_{sfc}. The PAI is larger in SEAFC than in SEA throughout the year, despite negligible CRE_{sfc} response in the polar region in the cold season (Fig. 3.6b). This is because the whole globe is generally warmed less in SEAFC (Fig. 3.5a), leading to a larger PAI for the same degree of polar warming. The results indicate that the strong seasonality of local CRE_{sfc} response, which originates from the intrinsic large seasonality of insolation in the polar region, is responsible for the seasonality of polar amplification in SEA. In more comprehensive models with sea ice, the temperature inversions occur in the boundary layer in the cold season, effectively contributing to strong winter polar amplification through the lapse rate feedback (Bintanja et al., 2011; Pavelsky et al., 2011; Pithan and Mauritsen, 2014). In our simulations with no sea ice, it is the weak CRE_{sfc} response that leads to the enhanced polar amplification in winter.

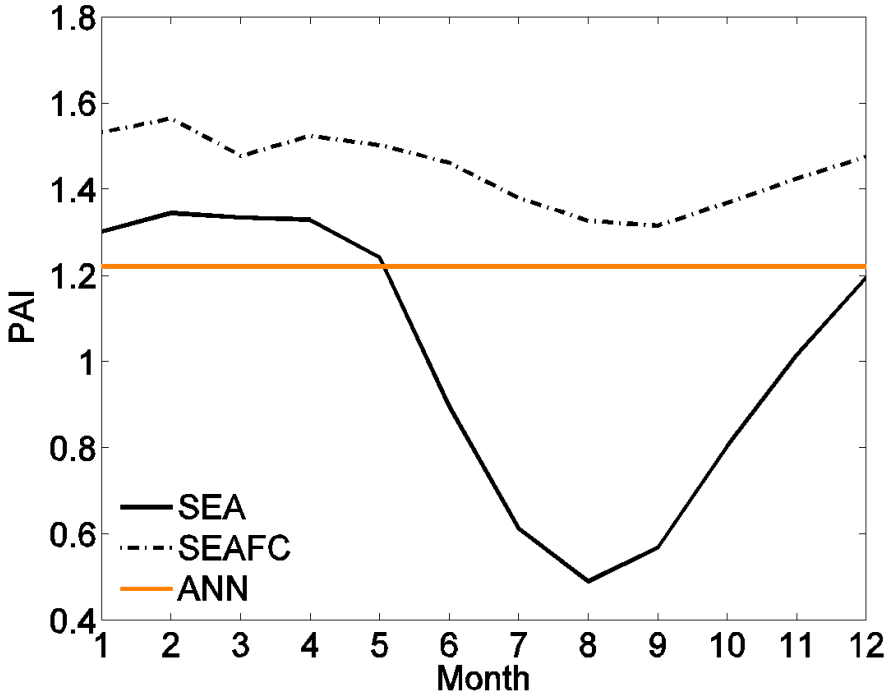

Figure 3.8. Monthly Polar Amplification Index (PAI; unitless) in SEA (black solid), SEAFC (black dashed), and ANN (orange solid) for the NH.

In ANN, there is a small negative CRE_{sfc} response in the polar region, despite a reduction of low-level cloud amount (Figs. 3.6a-b), which is presumably due to the increase of liquid water path (Ceppi et al., 2016). On the other hand, the annual-mean SEA exhibits a large negative CRE_{sfc} response in the polar region due to its nonlinear response with season (Fig. 3.6b). As a result, the PAI in ANN is larger than the annual-mean PAI in SEA (Fig. 3.8). Note that the strength of lapse rate feedback between SEA

ULSAN NATIONAL INSTITUTE OF
SCIENCE AND TECHNOLOGY

and ANN is similar because of the similar time-mean static stability in the respective control climate (Figs. 3.1c-d).

3.3.4. Feedbacks and remote effects

The radiative kernel technique enables a linear decomposition of climate response into the relative contributions from individual feedbacks. In particular, we utilize the radiative kernel technique to examine the role of the meridional structure of feedbacks, heat transport, radiative forcing, and possibly nonlinearities in controlling the meridional profile of surface temperature response. Following Feldl and Roe (2013a), Eq. (3.1) is reorganized to solve for the zonal-mean surface temperature response, by normalizing the terms in the energy balance by the global-mean Planck feedback ($\overline{\lambda_p}$):

$$\Delta T_s = \frac{1}{\overline{\lambda_p}}(\Delta R - (\lambda_p' \Delta T_s + \sum_i \lambda_{NP_i} \Delta T_s) - \Delta R_f) \tag{3.2}$$

In Eq. (3.2), $\lambda_p{}'$ is the local deviation from the global-mean Planck feedback, and λ_{NP} is the non-Planck feedbacks including lapse rate, water vapor, and cloud feedbacks. Note that there is no surface albedo feedback in our experiments. These individual contributions are presented in Figure 3.9 which are mostly consistent with previous studies in Taylor et al. (2013) and Feldl et al. (2017a). The sum of all terms (gray line) reproduces the actual response (black line), suggesting only a small nonlinearity in both SEA and SEAFC, thereby allowing us to examine the relative importance of individual contributions to the meridional pattern of surface warming. The Planck feedback is calculated from the surface temperature response applied uniformly with height in the troposphere. Following the Stefan-Boltzmann law, the outgoing longwave radiation increases with temperature, so that the Planck feedback cools the warm tropics and warms the high latitudes (violet in Fig. 3.9). The Planck feedback profile is nearly the same between SEA and SEAFC because their control climate states are similar.

ULSAN NATIONAL INSTITUTE OF
SCIENCE AND TECHNOLOGY

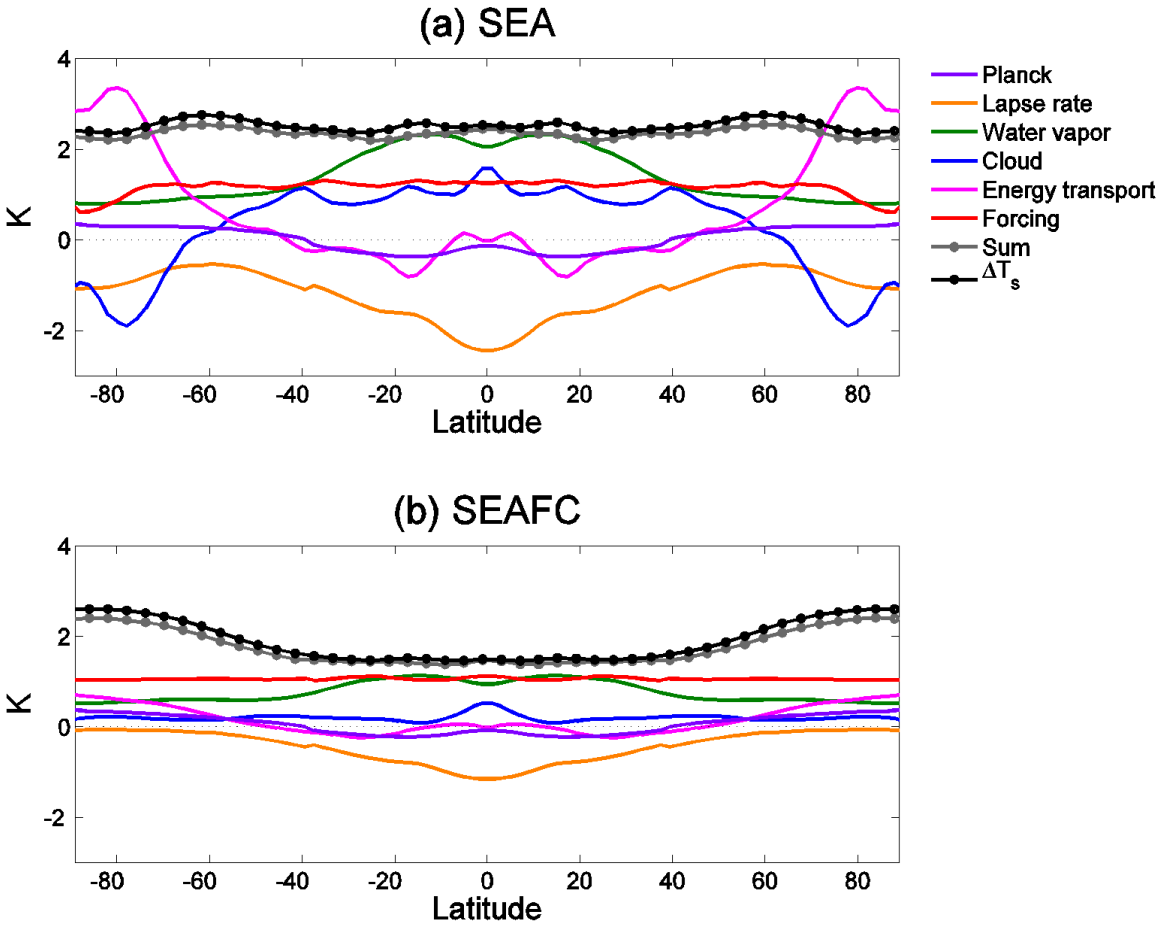

Figure 3.9. Zonal- and time-mean partial temperature changes (K) attributed to 2xCO_2 forcing (red), Planck (violet), transport (pink), water vapor feedback (green), cloud feedback (blue), and lapse rate feedback (orange), weighted by the global-mean Planck feedback following Feldl and Roe (2013). The sum of colored lines is shown in grey circled lines and the total surface temperature change, shown as black solid and dash-dot in Figure 3.5a, in black circled lines. (a) SEA and (b) SEAFC.

As discussed in Section 3.2, the cloud feedback (blue line) is positive in the tropics and negative in the polar region in SEA, while it nearly vanishes in SEAFC. Note that the masking effects are eliminated from CRE_{TOA} changes when calculating the kernel's cloud feedback, so the two terms are slightly different (contrast Fig. 3.4a and Fig. 3.9a). One may attempt to predict the surface temperature response pattern in SEAFC by removing the cloud feedback contribution from the total response in SEA. However, this prediction is imperfect (Fig. 3.10) because the large differences in cloud feedback in SEA and SEAFC influence other feedbacks.

The cloud feedback primarily strengthens the equator-to-pole energy imbalance in SEA, so that the resultant energy transport term is greater in SEA relative to SEAFC. The energy transport term

ULSAN NATIONAL INSTITUTE OF SCIENCE AND TECHNOLOGY

exhibits a pattern of low-latitude cooling and high-latitude warming (pink in Fig. 3.8), consistent with an increase of energy transport (Fig. 3.2a). The larger increase in energy transport in SEA contributes to a larger polar warming compared to SEAFC. This explains why the SEAFC prediction by removing the cloud feedback contribution from the SEA response overestimates the actual degree of polar amplification in SEAFC (Fig. 3.10).

The lapse rate feedback is associated with the vertical structure of atmospheric warming (Bintanja et al., 2012). It generally serves as a negative feedback in the tropics that exhibit a top-heavy warming profile, while it serves as a positive feedback in the polar region that exhibits a bottom-heavy warming profile (Serreze et al., 2009; Screen et al., 2012; Pithan and Mauritsen, 2014). However, in our experiments, the lapse rate feedback is globally negative (orange in Fig. 3.9), consistent with the low-albedo simulation in Feldl et al. (2017a). The lapse rate feedback in the polar region is positive only in EQN (Fig. 3.2). This is because the lower tropospheric static stability in all experiments other than EQN is not large enough to form an inversion in the polar region, due to the absence of surface albedo feedback. Instead of a bottom-heavy warming, the polar region in SEA presents the peak warming in the mid-troposphere in association with an increase of energy transport from the low latitudes (Fig. 3.1d). The negative lapse rate feedback in the polar region is larger in SEA than in SEAFC. This is because of a pronounced mid-tropospheric peak warming in SEA that is induced by a correspondingly larger increase in the energy transport (pink in Fig. 3.9) resulting from the cloud feedback that enhances the energy imbalance between the tropics and the extratropics. The negative lapse rate feedback cannot induce any warming in the polar region. However, its negative effect is larger in the tropics than in the polar region in both SEA and SEAFC, thereby contributing to the meridional pattern of polar amplification.

The positive cloud feedback in the tropics results in the warmer tropics, thereby strengthening the positive water vapor feedback (green) in SEA relative to SEAFC. The $2xCO_2$ forcing (red) in both SEA and SEAFC produces more warming in the low latitudes than in the high latitudes. The forcing term in SEAFC is more meridionally flat, consistent Huang et al. (2016) where cloud effects are shown to contribute to creating forcing inhomogeneity. The forcing contribution in SEA is comparable to that shown in Feldl et al. (2017a; see their Fig. 8). These cloud feedback, water vapor feedback, and forcing act to enhance the meridional temperature gradient, while the remaining terms such as the Planck feedback, lapse rate feedback, and energy transport terms act to induce polar amplification. Even though the energy transport term and lapse rate feedback lead to greater polar amplification in SEA than in SEAFC, the negative cloud feedback in the polar region effectively damps the polar surface warming in SEA. Conversely, there is little change in the energy transport in SEAFC due to the absence of cloud feedback, but the lapse rate feedback leads to polar amplification. As a result, there is only a weak signature of polar amplification in SEA whereas SEAFC exhibits a clear indication of polar

ULSAN NATIONAL INSTITUTE OF SCIENCE AND TECHNOLOGY

amplification. The feedback analysis corroborates the discussion in Section 3.2.

In models with a surface albedo feedback, the temperature feedback (both Planck and lapse rate feedback) is the most important contributor to the amplified warming response in the polar region (Pithan and Mauritsen 2014). In the absence of a surface albedo feedback, our aquaplanet simulation with a seasonal cycle highlights an important role played by the energy transport (Fig. 3.9; pink line). An increase of energy transport induces a mid-tropospheric peak warming in the polar region, which in turn leads to the lapse rate feedback to be negative. Thus, the energy transport term can contribute to polar amplification through the mid-tropospheric peak warming, but can counteract polar amplification by making the lapse rate feedback negative. The energy transport term generates polar warming at the expense of tropical cooling, in order to reduce the large equator-to-pole energy imbalance (i.e., heating in the tropics and cooling in the polar region), which is induced by the cloud feedback in SEA. Hence, in the case where large polar warming results from the energy transport, it is most likely that there exists a large negative feedback to cancel out the polar warming. Conversely, if there is small negative cloud feedback in the polar region, there is no need for an increase of energy transport. Hence, the sum of cloud feedback and energy transport term is expected to be almost meridionally flat. In the case of a smaller increase of energy transport, the mid-tropospheric peak warming will be less pronounced, and the lapse rate feedback in the polar region will be less negative. Since the lapse rate feedback is far more negative in the tropics, this may lead to greater polar amplification, as is the case of SEAFC. Pieced together, the energy transport increase itself can lead to polar warming through the mid-tropospheric warming but whether its effect ultimately contributes to polar amplification or not is highly uncertain due to its indirect impact on the lapse rate feedback.

3.4. Summary and discussion

In this paper, we adopt aquaplanet simulations coupled to a slab ocean under different insolation conditions to disentangle the mechanism for polar amplification in the absence of surface albedo feedback. The insolation condition is manipulated from the equinox (denoted as EQN) to the annual-mean (denoted as ANN) to the seasonally varying (denoted as SEA). We examine the pattern of surface warming in response to a doubling of CO_2 ($2xCO_2$).

The EQN experiment exhibits the most polar amplified warming, primarily due to the large static stability in the boundary layer (because no insolation reaches the pole throughout a year) that traps the warming response near the surface. Even though the static stability is not as large as in the real boreal winter Arctic with an inversion layer, the resultant bottom-heavy warming is responsible for a positive lapse rate feedback, which amplifies the polar surface warming. In contrast, the ANN and SEA experiments do not exhibit any maxima in static stability in the boundary layer, and the polar warming

ULSAN NATIONAL INSTITUTE OF SCIENCE AND TECHNOLOGY

response is maximized in the mid-troposphere, resulting in a negative lapse rate feedback in the polar region. This sensitivity of climate feedbacks on control climate has also been identified in comprehensive models (Hu et al. 2017). The mid-tropospheric polar warming can induce a weak polar surface warming through an increase of downward longwave radiative flux, but the polar surface warming in ANN is much weaker than in EQN. In SEA, the effect of mid-tropospheric warming on the surface is cancelled by a large negative CRE_{TOA} in the polar region, hence, there is no indication of polar amplification. Our result that EQN exhibits by far the strongest polar amplified surface warming pattern (3.5 times more polar amplified than in ANN) suggests that the positive lapse rate feedback is the most efficient mechanism for polar amplification. However, even in the absence of a positive lapse rate feedback, the surface warming pattern can be polar amplified as in ANN.

Polar amplification in ANN is induced by the mid-tropospheric polar warming, which is largely caused by condensational heating due to an increase of eddy latent heat transport at high latitudes. In particular, the near-surface midlatitude warming and/or the upper tropospheric tropical warming are suggested to be the origin of mid-tropospheric polar warming (Pauluis et al. 2008; Laliberté and Kushner 2014). The upper tropospheric warming in the tropics is amplified by the positive tropical CRE_{TOA} response, so that inhibiting the tropical CRE weakens the mid-tropospheric polar warming. In contrast, the polar CRE_{TOA} response is negative, so that inhibiting the polar CRE strengthens the polar surface warming. This influence of cloud adjustments on the degree of polar amplification suggests the need for better cloud parameterization in order to enhance the skill of climate models in simulating the polar amplification feature.

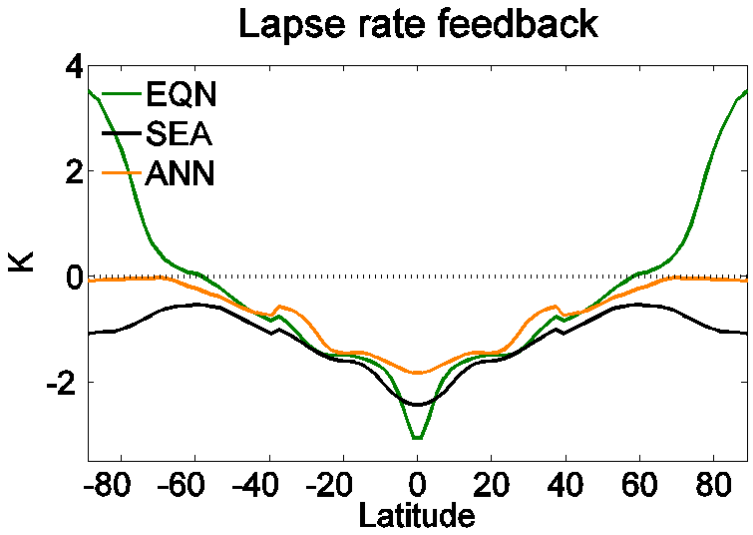

Figure 3.10. Zonal- and time-mean partial temperature changes (K) attributed to lapse rate feedback in EQN (green), SEA (black), and ANN (orange).

ULSAN NATIONAL INSTITUTE OF
SCIENCE AND TECHNOLOGY

In sum, the surface warming pattern in response to $2xCO_2$ can be polar amplified in the absence of surface albedo feedback, consistent with previous studies (Alexeev et al., 2005; Langen et al., 2012). We note that other mechanisms besides the surface albedo feedback, such as ocean heat uptake and storage, can contribute to the differences between our idealized simulations and more comprehensive models and observation. Similar to our experiments, the CAM3 aquaplanet simulation with a seasonal cycle in Langen et al. (2012), which has a weaker cloud feedback than our AM2, shows a similar degree and pattern of polar amplification to SEAFC (Fig. 3.5a). However, the annual-mean insolation experiment of Alexeev et al. (2005) shows much larger polar amplification due to a colder and more stable control climatology than our ANN. Polar surface warming is modulated by interactions among multiple climate feedbacks. For instance, the meridional profile of CRE response (which is positive in the tropics and negative in the polar region) gives rise to a larger tropical warming that induces a larger increase in eddy latent heat transport, thereby more effectively warming the mid-tropospheric polar region. This would tend to enhance the polar surface warming. The larger the negative polar CRE, the larger the increase in total atmospheric energy transport and the larger the polar surface warming. However, a large negative polar CRE also acts to directly counteract the polar surface warming. Thus, there is a competing effect between the atmospheric energy transport and local CRE. Furthermore, even though a larger mid-tropospheric warming is expected to contribute to surface warming, its effect on the lapse rate feedback is negative by inducing a top-heavy warming rather than a bottom-heavy warming (Singh et al., 2017). Another complication arises from the large compensation between latent energy transport and dry static energy transport. A larger polar surface warming would be induced by a larger increase in latent energy transport, which would be accompanied by a larger reduction in dry static energy transport that would in turn act to reduce the polar surface warming. However, the change in dry static energy transport cannot perfectly compensate for the increased latent energy transport (Merlis and Henry, 2017). This implies that a more controlled experiment is needed to identify how one feedback interacts with other feedbacks and energy transport, and what determines the degree of their compensation.

ULSAN NATIONAL INSTITUTE OF
SCIENCE AND TECHNOLOGY

Chapter 4. The decomposition of changes in the Arctic shortwave cloud radiative effects

In Chapter 3, the shortwave cloud radiative effect (SWCRE) has a significant role in the magnitude and seasonality of polar amplification. In this chapter, we assess the changes in SWCRE under global warming by analyzing CMIP models and feedback diagnostic frameworks. First, we will introduce the effective method to decompose the changes in SWCRE at the Arctic surface. Then, we will investigate the spread of changes in SWCRE across the CMIP models. Through the CMIP model analysis based on a newly introduced decomposition method, we will identify changes in SWCRE at the Arctic surface.

4.1. Background

In recent decades, the Arctic has undergone significant changes with extensive changes in shortwave (SW) radiation at the surface with rapidly declined sea ice in summer (Boeke and Taylor, 2018). Melting of sea ice and snow in response to global warming leads to a reduction in the surface albedo, thereby increasing the tremendous amount of SW absorption at the Arctic surface – feedback known as surface albedo feedback (Arrhenius, 1896; Manabe et al., 1992; Serreze et al., 2009). The decline in sea ice and the associated positive surface albedo feedback are strongest in summer when the maximum insolation reaches the Arctic. Then, the substantial SW absorption in summer is stored in the subsurface and the ocean releases heat and moisture in fall/winter through turbulent fluxes (Wetherald and Manabe, 1981; Lu and Cai, 2009; Bintanja et al., 2012; Sejas et al., 2014; Feldl et al., 2020; Chung et al., 2020). This seasonal energy transfer from summer to fall/winter is the main driver of amplified Arctic warming. Therefore, quantifying the changes in SW budget at the Arctic surface in summer, which is the primary energy source of Arctic warming, is essential to the projection of the Arctic climate change (Boeke and Taylor, 2018; Feldl et al., 2020).

In contrast to the increasing importance of surface albedo feedback, there is little attention to the Arctic clouds, albeit with considerable inter-model spread (Karlsson and Svensson 2013; Alkama et al. 2020). This is because of the insignificant cloud response to summer sea ice loss (Kay and Gettelman, 2009; Kay and L'Euyer, 2009; Choi et al., 2020). However, Arctic clouds play an important role in modulating surface radiative energy fluxes under Arctic warming. In response to global warming, the contemporary climate models exhibit the negative SW cloud radiative effect (CRE) over the Arctic Ocean. This is done by intensifying SW reflection through the increase in low cloud amount and optical depth during summer (Vavrus, 2004; Vavrus et al., 2009; Langen et al., 2012; Feldl et al., 2017a; Ceppi et al., 2016) Moreover, the cloud masking effect – the presence of clouds masks the surface albedo change – offsets the positive SW effect by surface albedo feedback. The significant negative SWCRE from cloud masking is shown over the Arctic Ocean even though the cloud fraction is steady from 1982

ULSAN NATIONAL INSTITUTE OF
SCIENCE AND TECHNOLOGY

to 2018 (Choi et al., 2020).

Understanding the changes in the SW fluxes and especially clarifying the SWCRE requires separating the contributions of these drivers. Partial radiative perturbation (PRP) (Wetherald and Manabe 1988) firstly calculates the change in radiative fluxes in the most accurate way by a repeated run of the offline radiative transfer model but the PRP method is computationally expensive. Alternatively, the radiative kernel (Soden et al. 2008) can be easily applied across different models with demanding fewer computations but the kernel technique becomes increasingly inaccurate when a different control climate (e.g., the control climate of a GCM and observation) is applied (Thorsen et al., 2018). Also, indirectly calculated CRE (Charlock and Ramanathan, 1985) in the radiative kernel technique – the difference between clear-sky and total-sky radiative fluxes (that is, CRE) is subtracted by the kernel-derived cloud masking effect – limits the further decomposition of CRE. Therefore, in shortwave decomposition, Approximate PRP (APRP) method is developed (Taylor et al., 2007). The APRP accurately reproduces PRP estimation for SW at TOA and surface (Kim et al., 2022) with reduced practical difficulties in PRP by using a simplified model instead of a repeated run of an offline radiative transfer model.

In this study, we will further break down the conventional APRP method described by Taylor et al. (2007) and Kim et al. (2022), focusing on the Arctic surface SW budget. The extended APRP method will allow us to decompose the response of the SW flux at the Arctic surface along with contributions from the changes in surface albedo, cloud (e.g., albedo-cloud masking effect, albedo-cloud reflecting effect, cloud amount change, and cloud reflectivity change), and non-cloud radiative properties. Here, the extended APRP method will be validated by the PRP method using the simulations with Community Earth System Model (CESM) and Parallel Offline Radiative Transfer (PORT) tool in CESM. Finally, we apply the extended APRP method to quantify the inter-model spread of the CMIP projection of SWCRE which is a poorly understood element of the Arctic climate system.

ULSAN NATIONAL INSTITUTE OF SCIENCE AND TECHNOLOGY

4.2. Data and methodology

4.2.1. Offline radiation calculation

We employ the Community Earth System Model version 2 (CESM 2), with Community Atmosphere Model version 6 (CAM6; Danabasoglu et al., 2020) as its atmosphere component, the Parallel Ocean Program version 2 (POP2; Smith et al., 2010) as its ocean component, and the Community Land Model version 5 (CLM5; Lawrence et al., 2019) as its land component at nominal 1° horizontal resolutions and 32 vertical layers in the atmosphere. CESM2 is the latest version of the CESM as a part of the Coupled Model Intercomparison Project version 6 (CIMP6; Eyring et al., 2016).

We perform two fully coupled CESM2 model simulations with CO_2 concentration prescribed which are identical to those that participated in the CMIP6 (e.g., piControl and abrupt-4xCO_2): one with a pre-industrial CO_2 concentration as a control and the other one with a quadruple CO_2 concentration from the pre-industrial level. The simulations with the last year of equilibrium state (e.g., 2000 years of the pre-industrial run and 150 years of quadrupling CO2 forcing run restarted from the pre-industrial run) are used to generate high-frequency instantaneous radiation fields for both the control and the quadrupling CO_2 simulations. To quantify the individual feedback contributions to SW radiative fluxes over the Arctic, offline radiation calculations using the Parallel Offline Radiative Transfer tool (PORT; Conley et al., 2013) substitute a single property in high-frequency radiation fields at a time. Here, we adopt the two-way PRP method to remove the decorrelation perturbation that has errors from two correlated fields. Firstly, the two-way PRP (Colman and McAvaney, 1997) produces radiation perturbation $\delta_{4-1}R_x$ for filed x (that is, forward) by replacing radiation-relevant variables from 4xCO_2 into 1xCO_2 climates. After that, the substitution of radiation-relevant variables from 1xCO_2 into 4xCO_2 climates produces radiation perturbation $\delta_{1-4}R_x$ (that is, backward) where x is a single variable such as cloud properties, surface albedo, water vapor, gases, aerosols, and CO_2. Then, the final radiation perturbation is calculated as

$$\frac{\delta_{4-1}R_x - \delta_{1-4}R_x}{2}. \tag{4.1}$$

For instance, $\delta_{4-1}R_{\text{cloud}}$ represents the difference in radiative fluxes between the control and perturbed climate, where cloud properties field from 1xCO_2 climate is substituted into abrupt 4xCO_2 while the other properties keep the same fields in 1xCO_2.

ULSAN NATIONAL INSTITUTE OF SCIENCE AND TECHNOLOGY

4.2.2. Extend APRP method for the Arctic surface SWCRE

The APRP method developed by Taylor et al. (2007) separates individual contributions to changes in the TOA fluxes of SW radiation. The method is also applied at the surface using a single-layer radiation model (Kim et al., 2022). In this simplified model which consists of the radiative properties–surface albedo (α), scattering (γ), and absorption (μ)–, the ratio of incident surface flux to the insolation ($Q_s^{\downarrow}$) is given by

$$Q_s^{\downarrow}(\alpha, \gamma, \mu) = \frac{SW_{\downarrow}^{SFC}}{S}, \tag{4.2}$$

where $\mathrm{SW}_{\downarrow}^{\mathrm{SFC}}$ is incident surface SW flux and S is incident solar radiation. The surface albedo (α) can be computed using surface upward and downward SW flux:

$$\alpha = \frac{\mathrm{SW}_{\uparrow}^{\mathrm{SFC}}}{\mathrm{SW}_{\downarrow}^{\mathrm{SFC}}}.$$

For given $Q_s^{\downarrow}$ and α, the net surface SW flux is

$$\mathrm{SW}_{\mathrm{net}}^{\mathrm{SFC}} = \mathrm{SW}_{\downarrow}^{\mathrm{SFC}} - \mathrm{SW}_{\uparrow}^{\mathrm{SFC}} = \mathrm{Q_s}(1-\alpha)S. \tag{4.3}$$

Then, a change in the SW flux at the surface is given by

$$\delta\mathrm{SW}_{\mathrm{net}}^{\mathrm{SFC}} = \delta[\mathrm{Q_s}(1-\alpha)S] = \mathrm{Q_s}(1-\alpha)\delta S - \mathrm{Q_s}S\delta\alpha + (1-\alpha)S\delta\mathrm{Q_s}. \tag{4.4}$$

Note that Eqs. (4.1)-(4.4) are given by equations (A4)-(A3) of Kim et al. (2022).

The change, δ represents the difference between two states such as 1xCO_2 and 4xCO_2 climates in this study. This indicates that we can ignore the changes in solar insolation because the increased CO_2 does not influence on variations in solar insolation. For brevity, we neglect the superscript SFC and define SW as the surface SW fluxes. Then, Eq. (4.4) can be rewritten in terms of the changes in $Q_s^{\downarrow}$ and α:

$$\delta\mathrm{SW}_{\mathrm{net}} = -\mathrm{Q_s}S\delta\alpha + (1-\alpha)S\delta\mathrm{Q_s}. \tag{4.5}$$

Next, we further break down the original APRP method in (Taylor et al., 2007) to compare the CRE (Charlock and Ramanathan, 1985). The change in the SW cloud radiative effect (SWCRE) is calculated by taking the subtraction of the clear-sky from the net-sky flux:

ULSAN NATIONAL INSTITUTE OF SCIENCE AND TECHNOLOGY

$$\delta SW_{CRE} = \delta SW_{net} - \delta SW_{clr,} \tag{4.6}$$

with seven radiative properties $(\mathrm{clt}, \alpha_{clr}, \alpha_{cld}, \mu_{clr}, \mu_{cld}, \gamma_{clr}, \gamma_{cld})$ calculated by using Eq. A (10) of Kim et al. (2022), δSW_{CRE} is defined as

$$\delta SW_{CRE} = -SQ_{s,CRE}\delta\alpha + S(1-\alpha)\left[\frac{\partial Q_s}{\partial \alpha_{cld}}\delta\alpha_{cld} + \frac{\partial Q_s}{\partial clt}\delta clt + \frac{\partial Q_s}{\partial \mu_{cld}}\delta\mu_{cld} + \frac{\partial Q_s}{\partial \gamma_{cld}}\delta\gamma_{cld}\right], \tag{4.7}$$

where $Q_{s,CRE}$ is calculated by δSW_{CRE} instead of $\delta SW_{net.}$ The SW flux at the clear-sky, δSW_{clr} is then given by

$$\delta SW_{clr} = -SQ_{s,clr}\delta\alpha + S(1-\alpha)\left[\frac{\partial Q_s}{\partial \alpha_{clr}}\delta\alpha_{clr} + \frac{\partial Q_s}{\partial \mu_{clr}}\delta\mu_{clr} + \frac{\partial Q_s}{\partial \gamma_{clr}}\delta\gamma_{clr}\right]. \tag{4.8}$$

where Q_{clr} is calculated by δSW_{clr} instead of $\delta SW_{net.}$

This extended APRP method can quantify the changes in SWCRE (δSW_{CRE}) in Eq. (4.7) by splitting albedo-cloud masking effect (δSWCRE-ALBM, $-Q_{s,CRE}S\delta\alpha$), albedo-cloud reflecting effect (δSWCRE-ALBR, $S(1-\alpha)\frac{\partial Q_s}{\partial \alpha_{cld}}\delta\alpha_{cld}$), cloud amount change (δSWCRE-CMT, $S(1-\alpha)\frac{\partial Q_s}{\partial clt}\delta clt$), and cloud reflectivity change (δSWCRE-CRF, $S(1-\alpha)\frac{\partial Q_s}{\partial \gamma_{cld}}\delta\gamma_{cld}$). The term perturbed by a fraction μ for atmospheric absorption is neglected in this study due to its small contribution.

4.2.3. Datasets

We examine the monthly mean data of model simulations from CMIP (the Coupled Model Intercomparison Project) Phases 5 and 6. To evaluate the SWCRE changes in response to the increases in CO_2 concentration, we use the CMIP simulations that are forced with the preindustrial control simulations (piControl) and the quadrupling of atmospheric CO_2 (abrupt-4 × CO_2). We use the results from up to 54 model simulations depending on data availability for specific variables and the time-averaged data of 120 to 150 years for both piControl and abrupt-4xCO_2 simulations. Also, we only consider the first available ensemble member for each model. The CMIP models analyzed in this study are listed in Table 4.1. Additionally, we use the CMIP5 with historical runs 1980-2005 and RCP4.5 2006-2100. The corresponding climate model outputs from CMIP6 are also used by merging historical runs from 1980 up to 2014 with SSP245 from 2014 up to 2100. As a proxy for observations, we analyze

ULSAN NATIONAL INSTITUTE OF SCIENCE AND TECHNOLOGY

two reanalysis datasets, the fifth generation of European Centre for Medium-Range Weather Forecasts (ECMWF) reanalysis (ERA5; Hersbach et al., 2020) and Modern-Era Retrospective analysis for Research and Applications, Version 2 (MERRA-2; Gelaro et al., 2017). Both ERA5 and MERRA-2 are compared with the CMIP models for the same period (1980-2014).

Table 4.1. Descriptions of CMIP5/6 models used in Chapter 4

Model Type	Model Number	Model name	Institution	PiControl abrupt-4xCO2	PiControl RCP4.5
cmip5	1	ACCESS1-0	CSIRO and BOM, Australia	Yes	Yes
	2	ACCESS1-3	CSIRO and BOM, Australia	Yes	Yes
	3	bcc-csm1-1	BCC, CMA, China	Yes	Yes
	4	bcc-csm1-1-m	BCC, CMA, China	Yes	Yes
	5	BNU-ESM	BNU, China	Yes	Yes
	6	CanESM2	CCCma, Canada	Yes	Yes
	7	CCSM4	NCAR, USA	Yes	Yes
	8	CESM1-BGC	DOE NCAR, USA	No	Yes
	9	CESM1-CAM5	DOE NCAR, USA	No	Yes
	10	CESM1-FASTCHEM	DOE NCAR, USA	No	Yes
	11	CNRM-CM5	CNRM and CERFACS, France	Yes	Yes
	12	CNRM-CM5-2	CNRM and CERFACS, France	Yes	Yes
	13	CSIRO-Mk3-6-0	CSIRO in collaboration with the QCCCE, Austrailia	Yes	Yes
	14	FIO-ESM	FIO,China	No	Yes
	15	GFDL-CM3	NOAA GFDL, USA	Yes	Yes
	16	GFDL-ESM2G	NOAA GFDL, USA	Yes	Yes
	17	GFDL-ESM2M	NOAA GFDL, USA	Yes	Yes
	18	GISS-E2-H	NASA/GISS, USA	No	Yes
	19	GISS-E2-H-CC	NASA/GISS, USA	No	Yes
	20	GISS-E2-R	NASA/GISS, USA	No	Yes
	21	GISS-E2-R-CC	NASA/GISS, USA	No	Yes
	22	HadGEM2-CC	MOHC, UK	No	Yes
	23	HadGEM2-ES	MOHC, UK	No	Yes
	24	IPSL-CM5A-LR	IPSL, France	Yes	Yes
	25	IPSL-CM5A-MR	IPSL, France	Yes	Yes
	26	IPSL-CM5B-LR	IPSL, France	Yes	Yes
	27	MIROC5	AORI, NIES, and JAMSTEC, Japan	Yes	Yes
	28	MIROC-ESM	AORI, NIES, and JAMSTEC, Japan	Yes	Yes
	29	MIROC-ESM-CHEM	AORI, NIES, and JAMSTEC, Japan	No	Yes
	30	MPI-ESM-LR	MPI-M, Germany	Yes	Yes
	31	MPI-ESM-MR	MPI-M, Germany	Yes	Yes
	32	MPI-ESM-P	MPI-M, Germany	No	Yes
	33	MRI-CGCM3	MRI, Japan	Yes	Yes
	34	NorESM1-M	NCC, Norway	Yes	Yes
	35	NorESM1-ME	NCC, Norway	No	Yes
	36	icnm4	INM, Russia	Yes	Yes

ULSAN NATIONAL INSTITUTE OF SCIENCE AND TECHNOLOGY

Model Type	Model Number	Model name	Institution	PiControl abrupt-4xCO_2	PiControl SSP245
cmip6	1	ACCESS-CM2	CSIRO and ARCCSS, Australia	No	Yes
	2	ACCESS-ESM1-5	CSIRO and ARCCSS, Australia	No	Yes
	3	AWI-CM-1-1-MR	AWI, Germany	Yes	Yes
	4	AWI-ESM-1-1-LR	AWI, Germany	No	Yes
	5	BCC-CSM2-MR	BCC, China	Yes	Yes
	6	BCC-ESM1	BCC, China	Yes	Yes
	7	CESM2	NCAR, USA	Yes	Yes
	8	CESM2-FV2	NCAR, USA	Yes	Yes
	9	CESM2-WACCM	NCAR, USA	Yes	Yes
	10	CESM2-WACCM-FV2	NCAR, USA	Yes	Yes
	11	CIESM	THU,China	No	Yes
	12	CMCC-CM2-HR4	CMCC,Italy	No	Yes
	13	CMCC-CM2-SR5	CMCC,Italy	Yes	Yes
	14	CNRM-CM6-1	CNRM and CERFACS, France	No	Yes
	15	CNRM-CM6-1-HR	CNRM and CERFACS, France	Yes	Yes
	16	CNRM-CM6-1	CNRM and CERFACS, France	Yes	Yes
	17	CanESM5	CCCma, Canada	Yes	Yes
	18	E3SM-1-0	DOE E3SM-Project, USA	Yes	Yes
	19	E3SM-1-1	DOE E3SM-Project, USA	No	Yes
	20	E3SM-1-1-ECA	DOE E3SM-Project, USA	No	Yes
	21	EC-Earth3	EC-Earth consortium	No	Yes
	22	EC-Earth3-Veg	EC-Earth consortium	No	Yes
	23	FGOALS-f3-L	CAS, China	Yes	Yes
	24	FGOALS-g3	CAS, China	Yes	Yes
	25	GFDL-CM4	NOAA GFDL, USA	Yes	Yes
	26	GFDL-ESM4	NOAA GFDL, USA	No	Yes
	27	GISS-E2-1-G	NASA/GISS, USA	Yes	Yes
	28	GISS-E2-1-G-CC	NASA/GISS, USA	No	Yes
	29	GISS-E2-1-1-H	NASA/GISS, USA	Yes	Yes
	30	GISS-E2-2-G	NASA/GISS, USA	Yes	Yes
	31	HadGEM3-GC31-LL	MOHC, UK	No	Yes
	32	HadGEM3-GC31-MM	MOHC, UK	No	Yes
	33	IITM-ESM	CCCR-IITM, India	No	Yes
	34	INM-CM4-8	INM, Russia	Yes	Yes
	35	INM-CM5-0	INM, Russia	Yes	Yes
	36	IPSL-CM6A-LR	IPSL, France	Yes	Yes
	37	KACE-1-0-G	NIMS-KMA, Korea	No	Yes
	38	KIOST-ESM	KIOST, Rebuplic of korea	Yes	Yes
	39	MIROC-ES2L	AORI, NIES, and JAMSTEC, Japan	No	Yes
	40	MIROC6	AORI, NIES, and JAMSTEC, Japan	Yes	Yes
	41	MPI-ESM-1-2-HAM	MPI-M, Germany	Yes	Yes
	42	MPI-ESM1-2-HR	MPI-M, Germany	Yes	Yes
	43	MPI-ESM1-2-LR	MPI-M, Germany	Yes	Yes
	44	MRI-ESM2-0	MRI, Japan	Yes	Yes
	45	NESM3	NUIST, China	Yes	Yes
	46	NorCPM1	NCC, Norway	No	Yes
	47	NorESM2-LM	NCC, Norway	Yes	Yes
	48	NorESM2-MM	NCC, Norway	No	Yes
	49	SAM0-UNICON	SNU, Republic of korea	Yes	Yes
	50	TaiESM1	RCEC, Taiwan	Yes	Yes
	51	UKESM1-0-LL	MOHC, UK	No	Yes

ULSAN NATIONAL INSTITUTE OF SCIENCE AND TECHNOLOGY

4.3. Results

4.3.1. Model projections of changes in Arctic surface SWCRE

We analyze the changes in SWCRE averaged over the Arctic Ocean from 23 CMIP5 and 31 CMIP6 model outputs (Fig. 4.1a), where SWCRE is calculated by taking the difference between net and clear-sky downward SW flux at the surface. The climate models project the significant negative SWCRE changes to quadrupled CO_2, thereby effectively damping the total changes in the net surface energy budget over the Arctic Ocean, but the models disagree on the magnitude of changes in SWCRE. Both CMIP5 and CMIP6 exhibit a large inter-model range from -37 to -13 W/m^2 for CMIP5 (-34 to -13 W/m^2 for CMIP6) in sunlight season (i.e., March through September)–the magnitude and spread of SWCRE response at the Arctic surface are strongest in sunlight season when the solar insolation is maximized in the Arctic region. Moreover, an improvement from CMIP5 to CMIP6 does not narrow the inter-model differences, indicating that we still have a lack of understanding of SWCRE prediction for estimating the SW energy budget at the Arctic surface.

The possible factor that partially explains the changes in SWCRE of the Arctic surface is the cloud amount change (Vavrus, 2004; Vavrus et al., 2009; Langen et al., 2012; Feldl et al., 2017a). For example, increases in cloud amount enhance the amount of SW reflected back from the clouds, thereby reducing the transmitted amount of SW at the surface. Note that the anomaly of cloud amount under greenhouse forcing is highly model-dependent (Vavrus, 2004). As expected, the CMIP models display a statistically significant correlation between changes in Arctic SWCRE and Arctic cloud amount in summer (correlation coefficient with a maximum of -0.66 for CMIP5 and -0.54 for CMIP6 in July). Figure 4.1b shows the changes in cloud amount averaged over the Arctic Ocean under abruptly quadrupled CO_2. The Arctic cloud amount mostly increases every month in CMIP5 with considerable model spread. In CMIP6, the range of changes in Arctic cloud amount across models is dramatically narrowed, with decreasing cloud amount, particularly on the high-end. However, the significant changes in Arctic cloud amounts from CMIP5 to CMIP6 are not reflected in the spread of SWCRE changes (Fig. 4.1a). This discrepancy is supported by several studies that the negative SWCRE in response to CO_2 increases is observed due to the sea ice loss despite the steady cloud amount (Karlsson and Svensson 2013; Alkama et al. 2020; Choi et al., 2020). Instead of cloud amount change, the negative SWCRE response is highly correlated with the decrease of surface albedo, which corresponds to the correlation coefficient with a maximum of 0.91 for CMIP5 (0.96 for CMIP6) in April. This implies that various controlling factors to influence changes in Arctic SWCRE should be quantified by feedback diagnostic frameworks.

ULSAN NATIONAL INSTITUTE OF
SCIENCE AND TECHNOLOGY

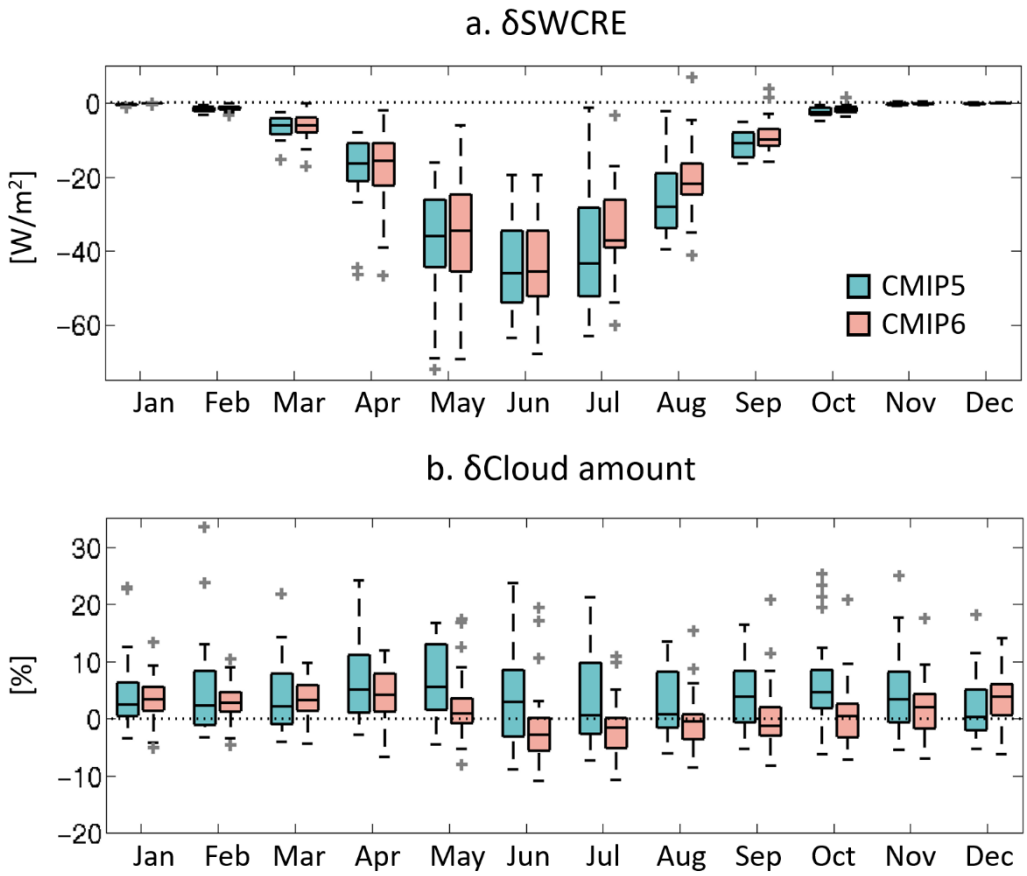

Figure 4.1. The box-and-whisker plots of results from 54 CMIP models (Table 4.1) after an abrupt quadrupling of CO_2 concentrations from the corresponding pre-industrial control climatology. The bars indicate the spread of changes in **a.** surface SWCRE (W/m^2) and **b.** cloud amount (%) averaged over the Arctic Ocean during the sunlit season (i.e., March through September). Extreme outliers, presented by the grey cross marks, are defined as points beyond three times the interquartile range from the edge of the box.

ULSAN NATIONAL INSTITUTE OF
SCIENCE AND TECHNOLOGY

4.3.2. Validation of extended APRP method: focusing on the Arctic surface SWCRE

To understand the changes in SWCRE at the Arctic surface, we further decompose the SWCRE with the extended APRP method. In this section, we aim to validate the extended APRP method by PRP method to understand the results of changes in SWCRE in CMIP models (see the 4.2. Data and methodology for details).

The changes in net surface SW fluxes calculated by PRP method (Fig. 4.2.a) accurately estimate the changes in SW outputs from models with a reasonable error (Fig. 4.2.f). The positive change seen at net surface SW is dominated by substantial increased SW absorption at the Arctic surface and is mostly explained by surface albedo feedback due to the declined sea ice (Figure 4.2.b). The albedo-related SW changes in clear sky account for 216% (84 W/m^2) of changes in net SW fluxes while the sum of albedo-related SW changes in CRE (Fig. 4.2.c) and cloud-related SW changes (i.e., changes in cloud amount, particle size, and liquid/ice water path; Fig. 4.2.d) is negative with a portion of -108% ($-42 W/m^2$) averaged over the Arctic Ocean during the sunlight season. The SW changes with extra properties including the water vapor, aerosols, gases, and CO_2 play negligible roles in changing the SW fluxes.

A comparison of PRP and APRP methods applied to response in quadrupling CO_2 experiments is summarized in Figure 4.3. The surface SW responses in extended APRP agree remarkably well with values using the PRP method. In addition, the APRP method also reproduces well the SW model output with a negligible error shown by the subtracting sum of the APRP method from the model output (Fig. 4.3f). Note that we modify the coefficient in the conventional APRP method in Taylor et al. (2007) based on the comparison of PRP method–the ratio of upward beam absorptivity to downward beam absorptivity (a) is replaced from 0 to 0.3 and the ratio of upward beam reflectivity to downward beam reflectivity (b) is replaced from 1 to 0.7 which are physically reasonable values supported by Winton et al. (2005). The modification of the coefficient improves the accuracy to separate the cloud-related δSW term in the extended APRP method compared with PRP calculation (Fig. 4.3d). The general features in the APRP method resemble the results from SW decomposition by PRP method: the albedo-related SW anomalies in clear-sky (Fig. 4.3b) show substantial amount of SW absorption at the Arctic surface while the albedo-related SW anomalies in CRE dampen the former impacts (Fig. 4.3c), which account for roughly half of the albedo-related SW anomalies in clear-sky.

ULSAN NATIONAL INSTITUTE OF
SCIENCE AND TECHNOLOGY

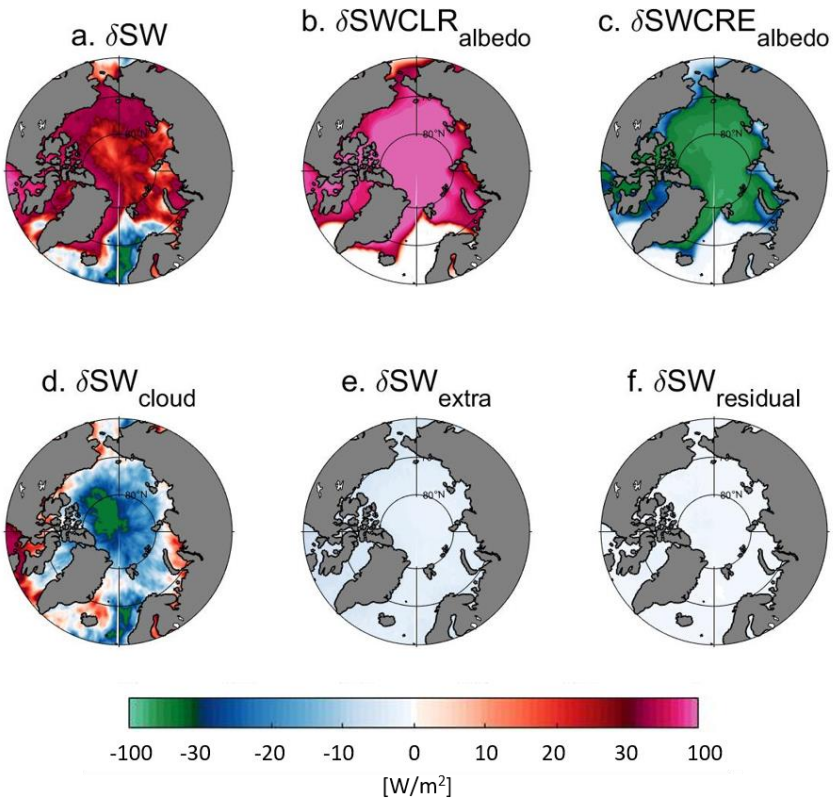

Figure 4.2. Average monthly maps of changes in surface SW radiation budget (W/m^2) in response to increases in CO_2 from the CESM2 model simulations calculated by the PRP method. Months are averaged during the sunlight season. **a.** Changes in surface net SW fluxes attributed to changes in **b.** surface albedo in clear-sky, **c.** surface albedo in CRE, **e.** cloud properties, and **d.** extra components such as water vapor, gases, and aerosols. **d.** The residual of the SW fluxes between the sums of all radiative components in the PRP method and model outputs.

ULSAN NATIONAL INSTITUTE OF
SCIENCE AND TECHNOLOGY

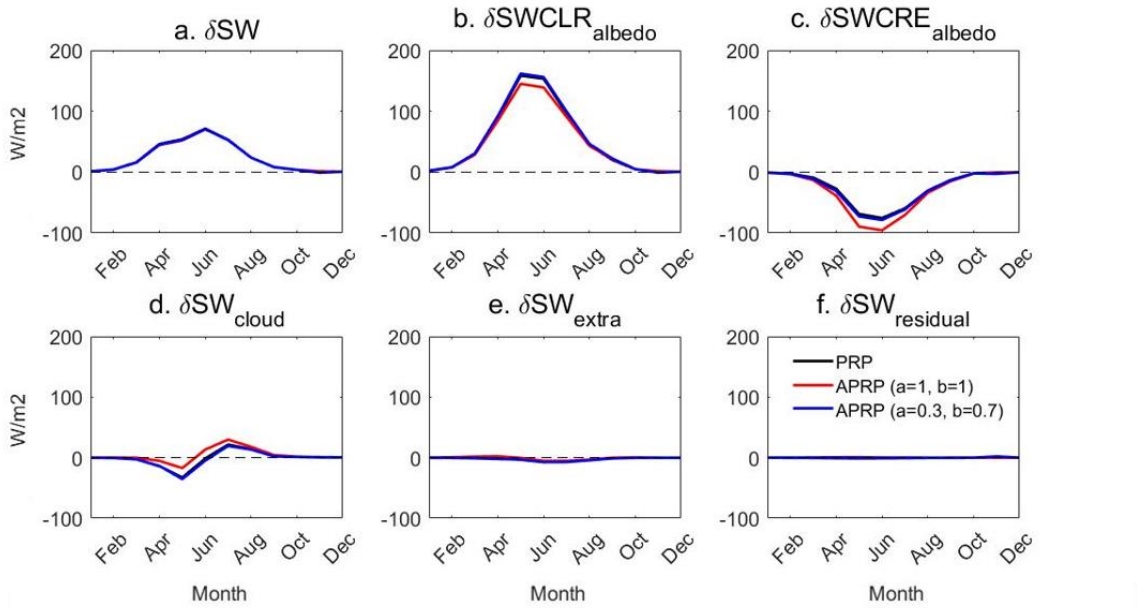

Figure 4.3. Monthly changes in surface net SW fluxes (W/m^2) in response to increases in CO_2 from the CESM2 model simulations calculated by the PRP (black solid line) and APRP (colored solid line) methods. **a.** Changes in surface net SW fluxes averaged over the Arctic Ocean are divided into each radiative component by the PRP and APRP methods (**b-e**). **f.** The residual is calculated by subtracting the sum of all radiative components in the PRP and APRP methods from the model outputs.

With this confirmation, we can quantify the negative changes in SWCRE on the Arctic surface with the following feedback mechanisms. Figure 4.4a depicts the surface albedo feedback between pre-industrial ($1xCO_2$, left panel) and CO_2 quadrupling ($4xCO_2$, right panel) climates. The reduction in surface albedo in response to CO_2 increases induces a considerable amount of extra SW absorption at the Arctic surface (Figs. 4.2a,b and 4.3a,b). Within the context of the surface albedo feedback, we define the albedo-cloud masking effect as SWCRE-ALBM (Sledd and L'Ecuyer 2019; Alkma et al., 2020; Choi et al., 2020, see also the 4.2. Data and methodology for details). The negative change of SWCRE-ALBM arises from the stronger positive surface albedo feedback in clear-sky than in all-skies–all skies contain the reduced incoming SW flux by the cloud reflection (Fig. 4.4a vs. Fig. 4.4b). The secondary term of albedo-related SWCRE, Albedo-cloud reflecting effect (Fig. 4.4c, δSWCRE-ALBR) can be explained by the following processes. Because the lower surface albedo in warmer climates reduces upward SW fluxes at the surface, the cloud reflects less SW fluxes back to the surface, thus decreasing SW fluxes at the surface after being reflected by clouds. Both δSWCRE-ALBM and δSWCRE-ALBR terms can be determined by changes in surface albedo without cloud change. Then, the sensitivity of

ULSAN NATIONAL INSTITUTE OF
SCIENCE AND TECHNOLOGY

δSWCRE to Arctic cloud properties is estimated by increase/decrease in cloud amount (δSWCRE-CMT, Fig. 4.4d) and cloud reflectivity (δSWCRE-CREF, Fig. 4.4e). An increase in cloud amount tends to increase the amount of reflected SW fluxes by clouds, yielding a negative SW cloud feedback. Moreover, the negative SW feedback in high latitudes is mainly associated with the optical thickness of clouds governed by cloud microphysics, where the changes in liquid/ice water path alter the brightness and reflectivity of clouds (Ceppi et al., 2016).

For the CMIP model analysis, Figure 4.5 demonstrates that our extended APRP method successfully reproduces the magnitude and spatial pattern of projected Arctic SWCRE in CMIP model outputs–CMIP models present a noticeable decrease in SWCRE for the multi-model mean (Fig. 4.5a), which coincides well with those estimated by APRP method (Fig. 4.5b) with small differences (Fig. 4.5c). Accordingly, in terms of model spread, there is a good agreement between the model δSWCRE and the sum of all components from the APRP method (Fig. 4.7) with high correlation values of 0.97 for CMIP5 and 0.96 for CMIP6 during the sunlight season. This indicates that the APRP method can be used to explain the magnitude and inter-model spread of changes in SWCRE at the Arctic surface.

ULSAN NATIONAL INSTITUTE OF SCIENCE AND TECHNOLOGY

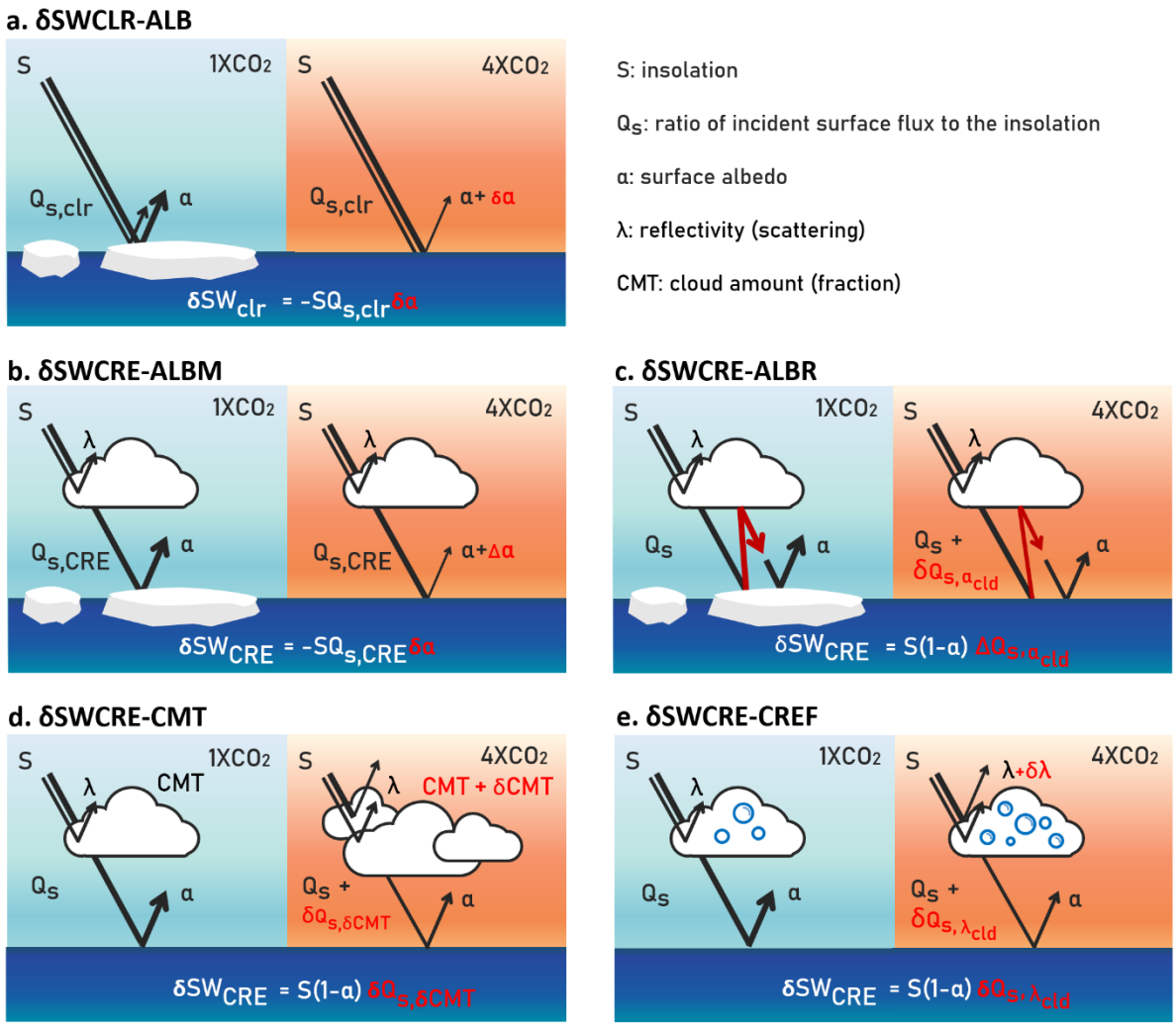

Figure 4.4. Schematic for changes in surface SW fluxes. **a.** The surface albedo effect in a clear-sky. The changes in SWCRE (**b-e**) are estimated by the sum of **b.** albedo-cloud masking effect, **c.** albedo-cloud reflecting effect, **d.** cloud amount change, and **e.** cloud reflectivity change from extended APRP method.

ULSAN NATIONAL INSTITUTE OF SCIENCE AND TECHNOLOGY

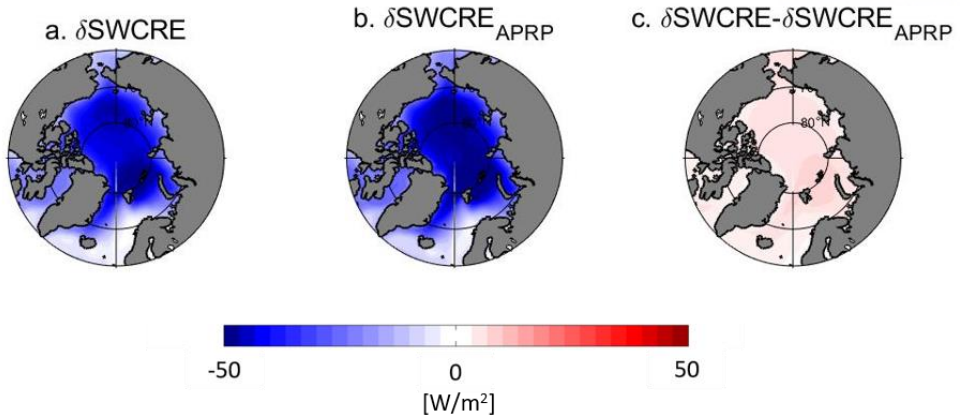

Figure 4.5. Average monthly maps of changes in surface SWCRE (W/m^2) in response to increases in CO_2 from **a.** CMIP multi-model mean outputs, **b.** APRP calculations, and **c.** residual by subtracting the sum of APRP calculations from the model outputs. Months are averaged during the sunlight season after an abrupt global quadrupling of CO_2 concentrations from the corresponding pre-industrial control climatology for 54 CMIP models (23 for CMIP5 and 31 for CMIP6).

ULSAN NATIONAL INSTITUTE OF SCIENCE AND TECHNOLOGY

4.3.4. Inter-model spread in projected Arctic surface SWCRE

In response to quadrupling CO_2, CMIP5/6 models exhibit an increase in multi-model mean SW absorption by 17 W/m^2 (Fig. 4.6a) which comes roughly 244% from positive surface albedo feedback in clear-sky (Fig. 4.6b) and is in turn offset by −144% due to decrease in SWCRE (Fig. 4.6c). Using Eq. (4.7) in the APRP method, we decompose the changes in SWCRE as a sum of albedo- and cloud-related changes in SWCRE (Fig. 4.6d-i). First, albedo-related changes in SWCRE (Fig. 4.6d) is −23 W/m^2 consisting of −19 W/m^2 due to the albedo-cloud masking effect (Fig. 4.6e) and −4W/m^2 due to the albedo-cloud reflecting effect (Fig. 4.6f). In particular, the albedo-cloud masking effect (or cloud damping effect) reduced surface albedo feedback by 42%. This magnitude is in accordance with previous studies: Alkama et al. (2020) find that clouds account for 47% of the net surface radiative impact of Arctic sea ice loss. Also, Sledd and L'Ecuyer (2019) attribute about half of the surface albedo feedback in TOA to cloud masking effect. Second, cloud-related changes in SWCRE (Fig. 4.6g) are made up of −6 wm^2 due to changes in cloud reflectivity (−5Wm^2, Fig. 4.6i) and cloud amount (Fig. 4.6h). A slightly negative value in Figure 4.6g indicates that an increase in cloud amount and optical depth enhances the SW reflection by cloud properties so that absorbed SW fluxes at the surface become more negative, but these effects are very small in the multi-model mean.

ULSAN NATIONAL INSTITUTE OF SCIENCE AND TECHNOLOGY

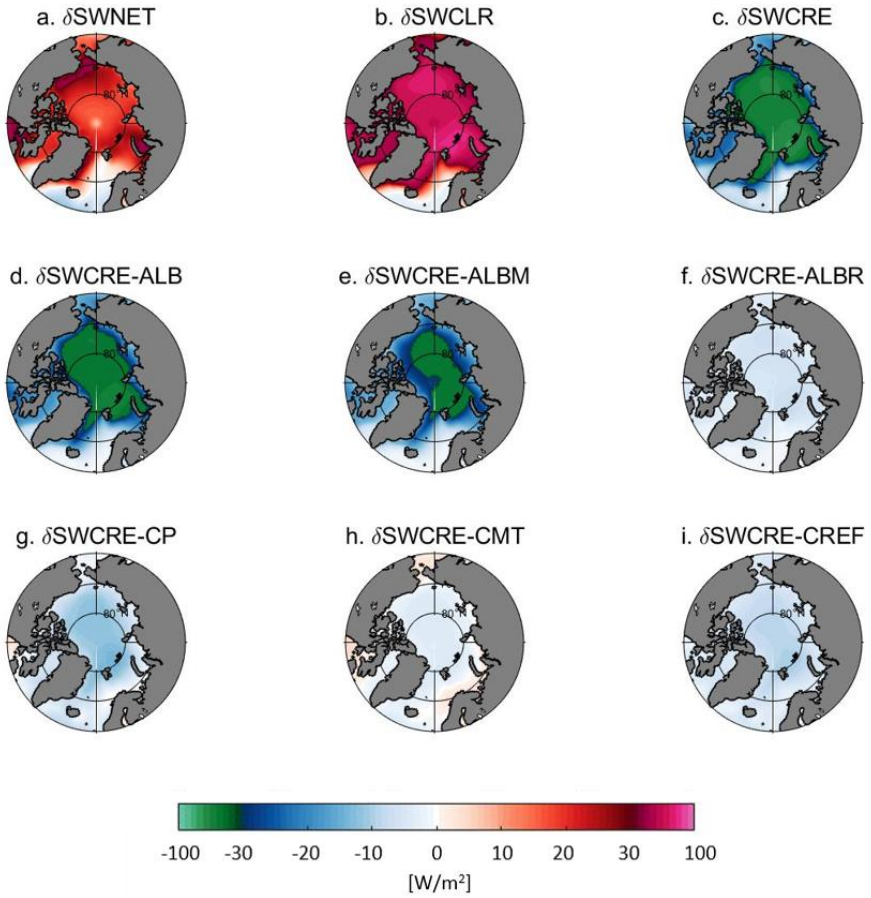

Figure 4.6. Same as in Fig 4.5. **a.** Changes in surface net SW fluxes (δSWNET) are divided into changes in **b.** clear-sky (δSWCLR) and **c.** cloud radiative effect (δSWCRE). Changes in SWCRE are further decomposed by **d.** albedo induced-term (δSWCRE-ALB) and **g.** cloud properties-induced term (δSWCRE-CP). Albedo-induced changes in SWCRE include **e.** albedo-cloud making effect (δSWCRE-ALBM) and **f.** albedo-cloud reflecting effect (δSWCRE-ALBR). Cloud properties-induced changes in SWCRE include **h.** cloud amount change (δSWCRE-CMT) and **i.** cloud reflectivity change (δSWCRE-CREF) from APRP calculation.

To reduce the model uncertainty in the surface radiation budget over the Arctic, it is crucial to investigate the causes of the inter-model spread in the projected Arctic SWCRE. In Figure 4.7, the considerable inter-model spread of changes in SWCRE originates mostly from the inter-model differences in the albedo-related terms, δSWCRE-ALBM and δSWCRE-ALBR, indicated by the high correlation of 0.76 for CMIP5 (0.73 for CMIP6) and 0.67 for CMIP5 (0.61 for CMIP6) respectively. The spreads in these albedo-related δSWCRE terms in CMIP5/6 are directly linked to the spread in surface albedo change (r= 0.90 to 0.96 during the sunlight season). Thus, this implies that the total inter-

ULSAN NATIONAL INSTITUTE OF SCIENCE AND TECHNOLOGY

model spread of changes in SWCRE can be attributed to model differences in albedo change by controlling albedo-related δSWCRE terms (i.e., δSWCRE-ALBM and δSWCRE-ALBR).

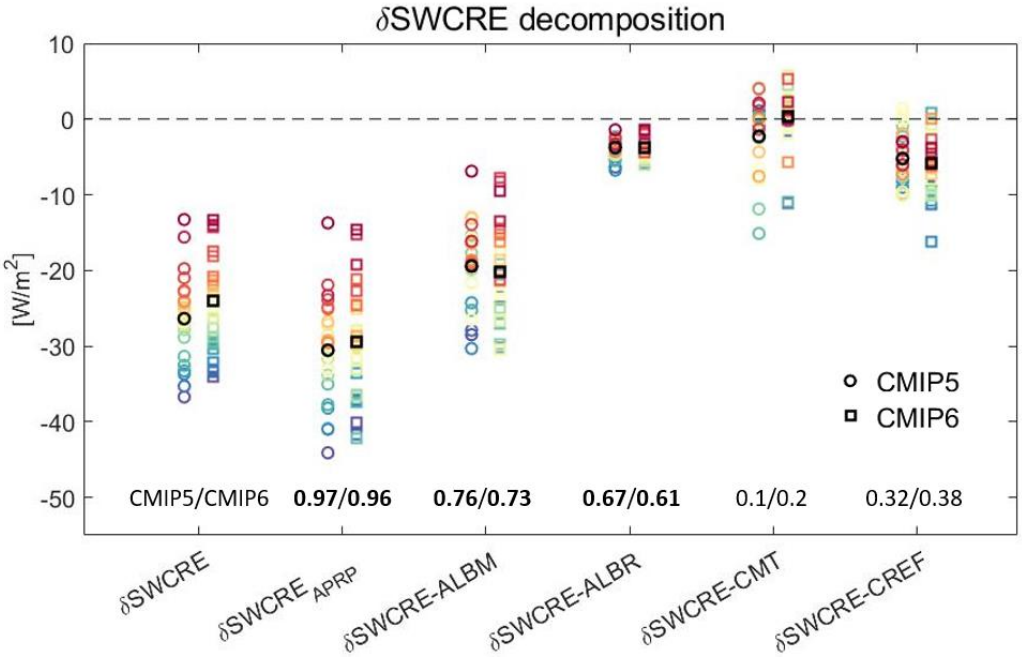

Figure 4.7. The plot of results from 54 CMIP models (Table 4.1) after an abrupt quadrupling of CO_2 concentrations from the corresponding pre-industrial control climatology. The attribution of the inter-model spread of changes in surface SWCRE (W/m^2) to the inter-model spread in the following components: albedo-cloud making effect (δSWCRE-ALBM), albedo-cloud reflecting change (δSWCRE-ALBR), cloud amount change (δSWCRE-CMT) and cloud reflectivity change (δSWCRE-CREF) averaged over the Arctic Ocean during the sunlit season (i.e., March through September) from APRP calculation. The CMIP models are colored according to the changes in surface SWCRE (circles for CMIP5 and squares for CMIP6). The correlation coefficients of each component and the sum of all components from APRP calculation ($\delta SWCRE_{APRP}$) to the δSWCRE are marked separately for CMIP5 and CMIP6 at the bottom of the plot. The correlation coefficient in bold indicates it reaches the significance level of 0.05.

ULSAN NATIONAL INSTITUTE OF SCIENCE AND TECHNOLOGY

Although the model differences in albedo change play an essential role in determining the inter-model spread of changes in SWCRE, we additionally analyze the spread of changes in SWCRE due to the changes in cloud properties. Both changes in cloud amount and reflectivity have only a small impact on the spread of changes in SWCRE. We find that δSWCRE-CMT is highly correlated with the cloud amount change across models (r =0.94 to 0.98 during the sunlight season) as expected in its definition in Eq. (4.7). However, most of the inter-model spread in δSWCRE-CREF is due to differences in mean state cloud properties, especially in liquid water path (LWP) rather than its change (r=0.48 in LWP and r=0.04 in δLWP). According to idealized tests of a cloud microphysics scheme (Gettelman, 2015), the changes in cloud reflectivity (also referred to as cloud albedo, γ_{cld}) depend on the slope of the relationship between cloud reflectivity and LWP ($d\gamma_{\mathrm{cld}}/dLWP$). Figure 4.8 confirms this relationship with yearly LWP from the historical run in cimip5/6 models. At low liquid water paths, the changes in cloud reflectivity are sensitive to LWP, indicating that a small perturbation of low LWP will have a significant effect on changes in cloud reflectivity. Therefore, models showing lower LWP in present-day produce a larger increase in cloud reflectivity in response to quadrupling CO_2. This explains why the spread of changes in cloud reflectivity is driven by the present-day across-model spread in the LWP.

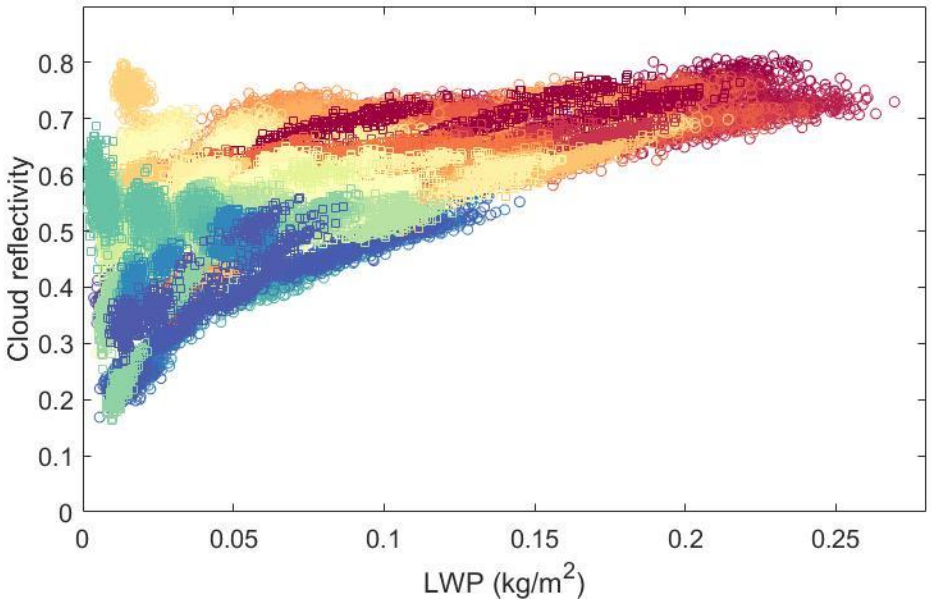

Figure 4.8. The scatter plot between the liquid water path (LWP, kg/m2) and cloud reflectivity (unitless) calculated by the APRP method. Circles and squares denote the results from CMIP5 and CMIP6, respectively, in yearly historical runs (Table 4.1) averaged over the Arctic Ocean during the sunlit season (i.e., March through September). Coloring from red to blue color is sorted in the ascending order of cloud reflectivity effect (SWCRE-CREF) in Figure 4.10.

ULSAN NATIONAL INSTITUTE OF
SCIENCE AND TECHNOLOGY

4.3.5. Uncertainties of Arctic surface SWCRE in present-day

In response to quadrupling CO_2, we showed that changes in SWCRE over the Arctic surface are dominated by albedo-related SWCRE terms. Consistently, under the future scenario (RCP 4.5 for CMIP5 and SSP245 for CMIP6), CMIP models show a continuous decrease in SWCRE with the decrease in surface albedo (Fig. 4.9) while the cloud properties remain fairly constant in response to global warming. For this reason, the uncertainties in the rapid decreasing of surface albedo contribute to inter-model spread of changes in SWCRE. Although the spread of changes in cloud properties is small compared to the spread of changes in surface albedo, one interesting feature in Figure 4.9 is that models strongly disagree with cloud amount and reflectivity in present-day.

To investigate the source of uncertainties in the present-day SWCRE, we compare the CMIP models and reanalysis (ERA5 and MERRA2) with the extended APRP method by setting multi-model mean as the reference climate state and individual models and reanalysis as target climate states (Fig. 4.10). In the present-day (1980-2014), the large inter-model spread in SWCRE mostly originates from the difference in cloud reflectivity. In contrast to the results from the spread in the future projection of SWCRE, the contributions from albedo-related terms to the inter-model spread of SWCRE in the present-day are insignificant while the role of cloud properties, especially cloud reflectivity is notable. Therefore, our results highlight that uncertainties and bias of SWCRE in present-day model simulations substantially arise from the inaccurate parameterization of cloud amount and microphysics (Vavrus, 2004; English et al., 2015; Cesana et al., 2012; Kay et al., 2016).

ULSAN NATIONAL INSTITUTE OF
SCIENCE AND TECHNOLOGY

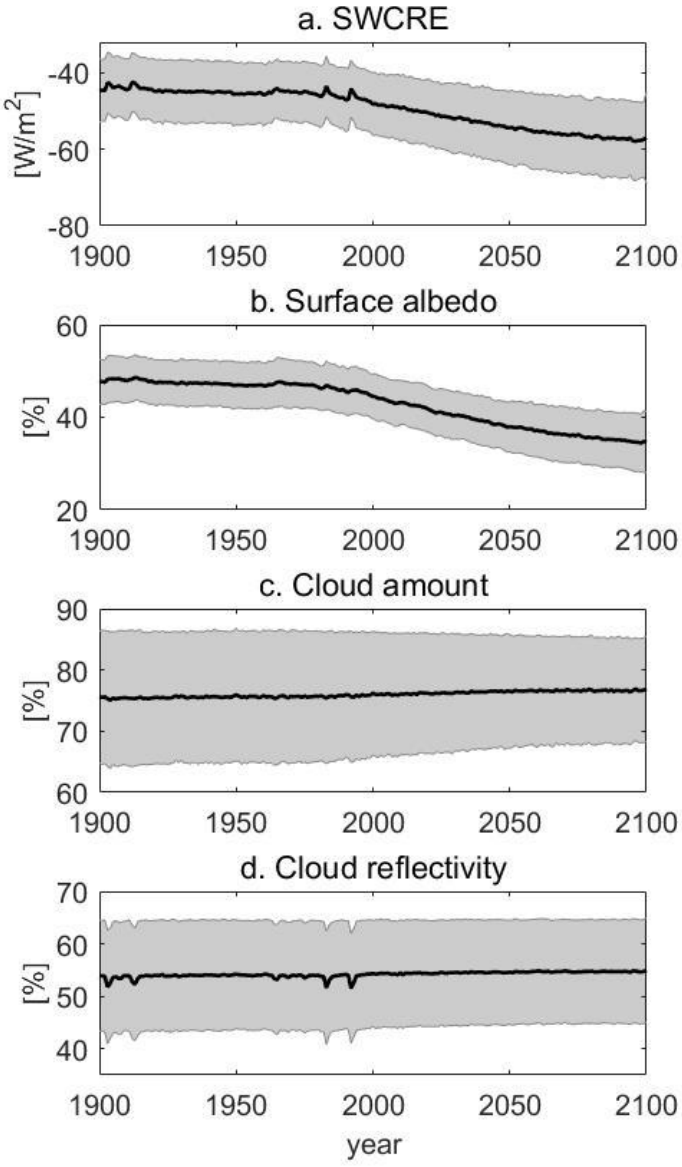

Figure 4.9. Time series of the **a.** SWCRE (W/m^2), **b.** surface albedo (%), **c.** cloud amount (fraction %), and **d.** cloud reflectivity (%). The solid line shows the multi-model mean; the envelope represents +/– one standard deviation bounds for CMIP5/6 models.

ULSAN NATIONAL INSTITUTE OF
SCIENCE AND TECHNOLOGY

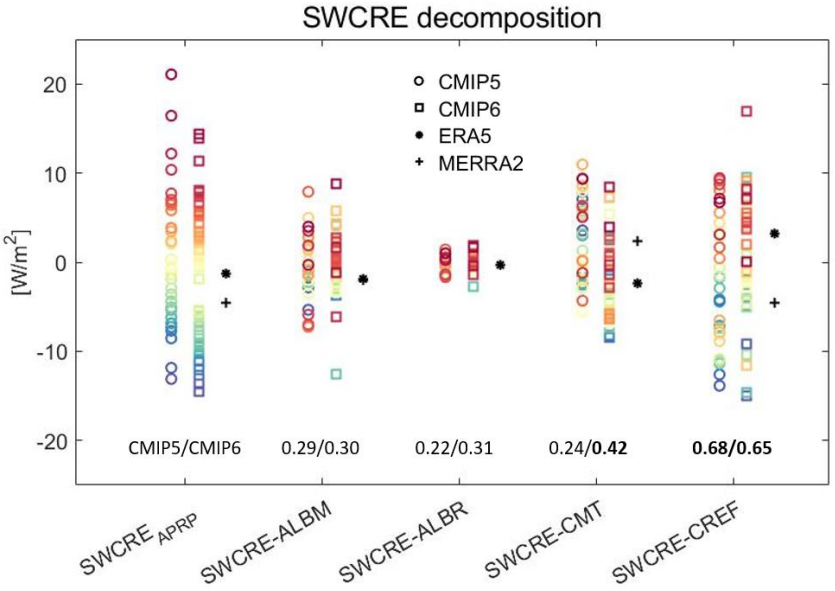

Figure 4.10. Attribution of the inter-model spread of surface SWCRE (W/m^2) to the inter-model spread in the following components: albedo-cloud making effect (SWCRE-ALBM), albedo-cloud reflecting effect (SWCRE-ALBR), cloud amount effect (SWCRE-CMT) and cloud reflectivity effect (SWCRE-CREF) in the Arctic Ocean averaged for the sunlit season (March through September). Both CMIP models (Table 4.1) and reanalysis datasets are analyzed for the period from 1980 to 2014 (CMIP5 products are made over 1980-2015 by merging historical runs 1980-2005 with RCP 4.5 2005-2014) with the data interpolated to a common 1°×1° grid. The CMIP models are colored according to the surface SWCRE (circles for CMIP5 and squares for CMIP6) and the EAR5 (starts) and MERRA2 (cross) results are juxtaposed on the right. The correlation coefficients of each component to the SWCRE are marked separately for CMIP5 and CMIP6 at the bottom of the plot. The correlation coefficient in bold indicates it reaches the significance level of 0.05. Note that the APRP calculation in Figure 4.10 sets the multi-model mean of CMIP5/6 as the reference climate state and marks indicate deviations in individual models and reanalysis from the reference states.

ULSAN NATIONAL INSTITUTE OF
SCIENCE AND TECHNOLOGY

4.5. Summary and discussion

In this study, we investigate the multi-model projections for SWCRE at the Arctic surface. Climate models project the significant negative changes in SWCRE with a large inter-model spread. The magnitude and model spread of the projected changes in SWCRE is the strongest in the Arctic Ocean during the sunlight season. To separate the changes in SWCRE into various contributions from each radiative process, the extended APRP method is used to calculate δSWCRE as the sum of δSWCRE-ALBM (albedo-cloud masking effect), δSWCRE-ALBR (albedo-cloud reflecting effect), δSWCRE-CMT (cloud amount change), and δSWCRE-CREF (cloud reflectivity change). The extended APRP applied at the surface, in a single layer model, is validated by the PRP method with offline radiation calculations. The calculations in the PRP method demonstrate that our extended APRP method reasonably decomposes the individual SWCRE feedback at the Arctic surface.

By masking and reflecting the impact of changes in surface albedo, the presence of Arctic clouds reduces the positive surface albedo feedback under clear-sky conditions. The albedo-related SWCRE terms (δSWCRE-ALBM and δSWCRE-ALBR) may explain up to roughly 42% of magnitude in δSWCRE and its inter-model spread. Consequently, our results demonstrate that changes in surface albedo play an important role in the magnitude and spread of δSWCRE over the Arctic surface. In addition, the model differences in present-day LWP instead of its changes explain the spread in δSWCRE-CREF. This emphasizes how well the climate models reproduce present-day cloud properties improve the uncertainty in changes in Arctic SWCRE by cloud properties. Finally, the study will allow for both a better attribution of simulated Arctic SWCRE–which presents a strong negative in surface radiative energy budget over the Arctic–and help our understanding of the fundamental physical processes of changes in SWCRE, thereby constraining uncertainties in future Arctic climate change.

ULSAN NATIONAL INSTITUTE OF
SCIENCE AND TECHNOLOGY

Chapter 5. Atmospheric circulation sensitivity to changes in the vertical structure of polar warming

In Chapter 3, we find the distinguishable vertical pattern of polar warming and this is a consequence of distinct physical mechanisms underlying polar amplification. As introduced in chapter 1.4, the possible linkage between the variation of vertical Arctic warming and that of remote response to Arctic warming is raised in several studies. In this chapter, we will examine the remote effect of Arctic warming with a different vertical structure through idealized experiments. In addition, the radiative kernels introduced in Chapter 2.2 will be computed to analyze the contributions of the vertical distribution of Arctic warming on radiative energy compensation, which accounts for anomalous atmospheric circulation changes in the non-Arctic regions.

5.1. Background

The greenhouse gas-induced surface warming is most amplified near the pole compared to the rest of the globe, a phenomenon known as polar amplification (Arrhenius, 1896; Cai, 2005; Holland and Bitz, 2003; Manabe et al., 1991; Solomon, 2007). The polar amplification has pronounced seasonality, being most prominent in winter when the warming is confined to near-surface due to limited vertical mixing from surface inversions (Bintanja et al., 2011). Conversely, the polar surface warming is weakest during summer with larger warming aloft than at the surface (Screen and Simmonds, 2010). The surface-based Arctic warming is largely caused by sea-ice loss (Kumar et al., 2010; Screen and Simmonds, 2010), whereas the warming aloft is accounted for by increased poleward energy transport associated with remote (non-Arctic) warming (Screen et al., 2012). Direct radiative forcing also contributes to an enhanced warming in the mid-troposphere in summer (Chung and Räisänen, 2011; Screen et al., 2012). Thus, despite the near-surface amplifying characteristic of polar amplification, significant warming is identified up to 400 hPa over the Arctic in most seasons during the historical period in multiple reanalyses and model simulations (Chung and Räisänen, 2011; Screen et al., 2012). Idealized experiments show that the vertical structure of CO_2-induced polar warming varies from surface trapped to deep (i.e., extending into the mid-troposphere) depending on the polar static stability in the control climate (Feldl et al., 2017; D. Kim et al., 2018).

Here, we address the question of whether the vertical structure of polar warming matters for its accompanying local and remote climatic effects. The near-surface Arctic warming induced by sea-ice loss has profound far-field effects, including a weakening and equatorward shift of the extratropical jet (Deser et al., 2015; Francis and Vavrus, 2012) and a meridional shift of the tropical precipitation (Chiang and Bitz, 2005; England et al., 2020; D. M. Smith et al., 2017). Arctic sea-ice loss was also suggested to be responsible for observed extreme cold weather events over Eurasia (e.g., Mori et al., 2014), but this has been argued against in recent literature (Blackport and Screen, 2021; Zappa

ULSAN NATIONAL INSTITUTE OF SCIENCE AND TECHNOLOGY

et al., 2021). Deep Arctic warming extending into the mid-troposphere has been proposed to be essential for the Arctic-to-midlatitude linkages; thus, Arctic sea-ice loss itself may be insufficient for inducing a midlatitude response due to its shallow near-surface warming (He et al., 2020; Labe et al., 2020). However, the mechanism by which the vertical extent of Arctic warming modulates Arctic-midlatitude teleconnections is not yet understood.

The sensitivity of remote climate response to the vertical structure of polar warming has been inferred from how the vertical temperature structure influences the eddy activity in previous studies. As a result of greenhouse warming, temperature gradients near the surface are reduced in northern winter, associated with Arctic amplification, whereas those in the upper troposphere are enhanced due to moist adiabatic adjustment in lower latitudes (e.g., Wu et al., 2011). Two schools of thought exist regarding the dominance of the two opposing changes: one suggests that the lower tropospheric temperature gradient has a stronger influence on extratropical jet activity based on the linear instability theory (Held and O'Brien, 1992; Pavan and Held, 1996); and the other argues for a central role played by the upper-tropospheric temperature gradient through changes in eddy phase speed (Chen et al., 2008) or associated with large baroclinicity concentrated in upper levels (Yuval and Kaspi, 2016). In a global warming scenario of a global coupled general circulation model (GCM), Wu et al. (2011) concluded that the storm track intensity is more determined by the upper rather than the lower tropospheric baroclinicity. It remains an open question if the effectiveness of polar warming at perturbing the remote climate such as the midlatitude jet and Hadley circulation depends on the vertical structure of polar warming.

In this study, we investigate the distinct remote effect of polar warming with a different vertical structure. In contrast to the previous literature that employed dry dynamical models to study the atmospheric circulation sensitivity to the location of diabatic heating (Baker et al., 2017; Butler et al., 2010; Yuval and Kaspi, 2016), we use moist GCMs that allow us to examine the tropical precipitation response. To gain the first-order physical understanding, a GCM with a gray radiation scheme is used that ignores water vapor- and cloud-radiative feedbacks (Frierson et al., 2006). We confirm the robustness of gray model results by examining a comprehensive atmospheric GCM in an identical aquaplanet slab-ocean framework.

5.2. Data and methodology

Experiments are conducted using the GRaM (gray radiation moist GCM) coupled to a 2.4-m mixed layer (Frierson et al. 2006). The model integrates the primitive equations using a spectral method at T42 resolution with 25 vertical levels. The solar flux approximates the annual-mean net shortwave flux at the top of the atmosphere with no absorption within the atmosphere, i.e., seasonality is absent. The infrared fluxes are only a function of temperature, i.e., there are no ice-, water vapor-, or cloud-

ULSAN NATIONAL INSTITUTE OF SCIENCE AND TECHNOLOGY

radiative feedbacks. The control experiment is run freely with no surface flux adjustment, and this control is perturbed by adding heating to the temperature tendency equation poleward of 65°N at different vertical levels (black contours in Fig. 5.1a). The experiments are named based on the lowest vertical level of prescribed heating. For example, L850 designates the experiment with prescribed heating between 850-700 hPa poleward of 65°N, where the peak heating occurs at 775 hPa with a value of 4.2 K/day. We may consider the lowest-level forcing case (L990) as mimicking the bottom-heavy warming associated with ice-albedo feedback, while the other three cases (L850, L700, and L550) may be considered the tropospheric warming induced by enhanced poleward energy transport, diffusion/advection from the surface warming, or local radiative changes (e.g., shifts in cloud altitude). The vertically-integrated heating magnitude is constrained to be independent of the forcing profile. Hence, the differences in the climate response across the experiments solely result from the altered vertical structure of polar warming. In the reference set of experiments, the vertically-integrated prescribed heating increases from zero equatorward of 65°N to a maximum of 50 W/m^2 at the pole (Fig. 5.2a), which amounts to a peak change in energy flux units of 0.57 PW (see Eq. 5.2). The sensitivity to the forcing amplitude is examined by modulating the forcing amplitude by $\pm$30 %.

We also employ a comprehensive general circulation model developed at the Geophysical Fluid Dynamics Laboratory (GFDL), Atmospheric Model, version 2 (AM2) (Anderson et al., 2004) to understand the effects of water vapor- and cloud-radiative feedbacks. It is run at a horizontal resolution of 2° latitude x 2.5° longitude and 24 vertical levels. The AM2 is coupled to a 2.4-m aquaplanet mixed layer and forced by the annual-mean insolation, as in GRaM. We only conduct L990 and L650 experiments with AM2 using the same forcing magnitude as in the reference set of GRaM experiments (Fig. 5.4a). The forcing depth in AM2 is increased to 300 hPa from 150 hPa in GRaM to avoid sharp temperature gradients that may lead to unrealistic cloud responses. All experiments in GRaM and AM2 are integrated for 40 years after 10 years of spinup without any surface flux adjustments. Although the Arctic region is perturbed in our experiments, we note that there is no distinction between Arctic and Antarctic because the lower boundary is a hemispherically symmetric aquaplanet. Hence, our results are not specific to Arctic but more generally relevant to polar regions.

5.3. Results

The temperature response profile progressively shifts from bottom-heavy to top-heavy as the heating altitude increases (Fig. 5.1a). Although the heating profile and amplitude are kept constant, for upper-level heating the warming response is more confined to the forcing area with a larger maximum amplitude at the forcing center, while the vertically averaged warming response remains similar at around 2 K for all experiments. Associated with the distinct temperature response profile at high-latitudes is the sensitivity of the global atmospheric circulation response to the vertical structure of polar

ULSAN NATIONAL INSTITUTE OF SCIENCE AND TECHNOLOGY

warming (Figs. 5.1b,c). In response to reduced meridional temperature gradients at any vertical level, the extratropical jet shifts equatorward (Fig. 5.1b), consistent with Butler et al. (2010) and Baker et al. (2017). In response to inter-hemispheric temperature contrasts, the rising branch of the Hadley circulation shifts northward, indicated by an anomalously counter-clockwise cross-equatorial circulation (Fig. 5.1c), consistent with Kang et al. (2009). These remote large-scale atmospheric circulation responses are more pronounced for polar warming at upper levels.

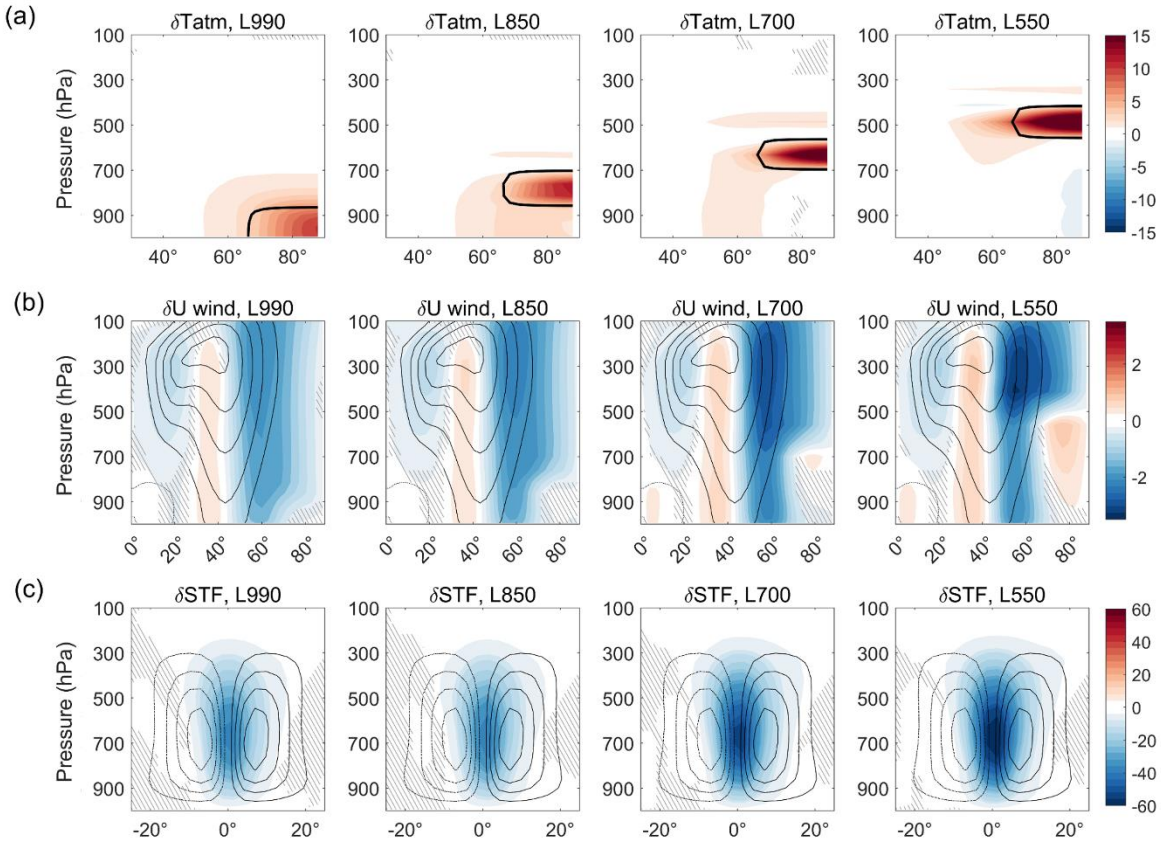

Figure 5.1. Response of time- and zonal-mean (a) temperature (K, shading), (b) zonal wind (m/s, shading) and (c) mean meridional streamfunction response (10^9 kg/s, shading). Solid black contours in (a) denote the forcing region. The black contours in (b) indicate the control climatology, with westerlies in solid and easterlies in dashed at a contour interval of 5 m/s. The black contours in (c) indicate the control climatology, with a clockwise circulation in solid and a counter-clockwise circulation in dashed at a contour interval of 5.5×10^{10} kg/s. Results from L990 (first column), L800 (second column), L700 (third column), and L550 (fourth column). Hatched regions indicate statistically insignificant values at the 95 % confidence level based on a two-sided t-test.

ULSAN NATIONAL INSTITUTE OF
SCIENCE AND TECHNOLOGY

The extratropical jet and Hadley circulation play an important role in transporting energy poleward. In the midlatitude, transient eddies are the dominant mechanism of energy transport (Peixoto and Oort, 1992) and consequently a poleward eddy-driven jet shift leads to an increase of poleward energy transport (Shaw and Voigt, 2016). In the tropics, the energy transport across the equator is determined by anomalous Hadley circulation, which responds to an inter-hemispheric energy asymmetry (Kang et al., 2008; Seo et al., 2014). Hence, we examine the atmospheric energy budget to understand the sensitivity of large-scale circulation to the vertical structure of polar warming. The steady-state energy budget for the atmospheric column is:

$$\delta\nabla \cdot F_{\mathrm{A}} - \delta R_{\mathrm{TOA}} = Q, \tag{5.1}$$

where F_{A} is the meridional transport of vertically-integrated moist static energy, R_{TOA} is the top-of-atmosphere (TOA) net radiation, and Q is the vertically-integrated prescribed heating. The δ denotes the difference between the perturbed and the control ($Q = 0$) experiments. Fig. 5.2a confirms that Q is identical for all perturbation experiments. Note that in GRaM the TOA radiation response is determined by the outgoing longwave radiation (OLR), which is a function of temperature only, as the shortwave radiation is a specified function of latitude. The OLR response closely follows the surface temperature response (Figs. 5.2b,c), so that lower-level heating is balanced more by changes in radiative cooling δR_{TOA} than in atmospheric energy transport divergence $\delta\nabla \cdot F_{\mathrm{A}}$ (Eq. 5.1).

ULSAN NATIONAL INSTITUTE OF
SCIENCE AND TECHNOLOGY

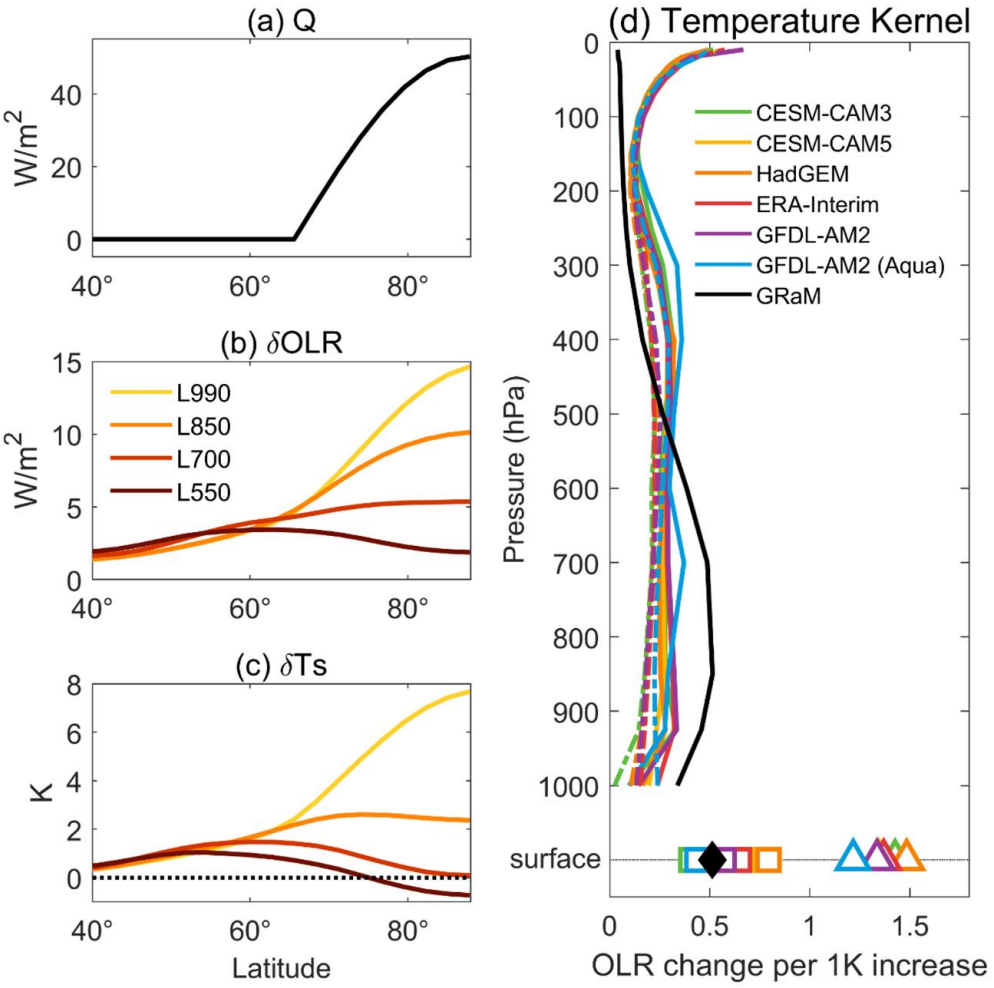

Figure 5.2. (a) The vertically-integrated prescribed heating (Q in Eq. 5.1) and the zonal- and time-mean response of (b) OLR and (c) surface temperature for the reference set of experiments. (d) The OLR change resulting from an increase in temperature of 1 K at each layer ($W/m^2/K/100$ hPa) averaged over 60-90°N. The temperature kernel in GRaM (black) is compared with that in other models: CESM-CAM3 (green, Shell et al., 2008), CESM-CAM5 (yellow, Pendergrass et al., 2018), HadGEM (orange, Smith and Christopher 2018), EAR-Interim (red, Huang et al., 2017), GFDL-AM2 (purple, Soden et al., 2008) and Aquaplanet GFDL-AM2 (blue, Feldl et al., 2017), separately for all-sky (solid) and clear-sky (dashed). The surface component of the kernel ($W/m^2/K$) is indicated by the black diamond for GRaM, by squares and triangles for other models under all-sky and clear-sky conditions, respectively, with the same color-coding as for the atmospheric temperature kernel.

ULSAN NATIONAL INSTITUTE OF SCIENCE AND TECHNOLOGY

The question then arises as to what causes the OLR response to be dominated by the surface temperature response rather than upper-tropospheric temperature response. We use the radiative kernel technique (Soden et al. 2008; see chapter 2.2) to examine the effect of the vertical temperature structure on the OLR. Figure 5.2d compares the temperature kernels averaged over 60°-90°N, which is the OLR response to incremental increases in temperature of 1 K at each vertical level and the surface, based on GRaM (black) as well as more comprehensive models (Shell et al., 2008; Feldl et al., 2017; Pendergrass et al., 2018; Smith and Christopher, 2018) and ERA-interim (Huang et al. 2017). For other models than GRaM, the kernel is calculated separately for clear-sky (dashed) and all-sky (solid) conditions.

All temperature kernels show that the surface temperature contribution to OLR change is larger than that from any individual 100-hPa thick atmospheric layer (Soden et al., 2008). The contrast is particularly strong under clear-sky conditions in comprehensive models (dashed lines versus triangles). While the GRaM has larger sensitivities of longwave fluxes to temperature changes below 500 hPa compared to more comprehensive models, it also features the strongest sensitivity at the surface (black line versus black diamond in Fig. 5.2d) owing to the large emissivity. Low sensitivities occur within the high-latitude atmosphere because the longwave fluxes are less sensitive to temperatures associated with the smaller sensitivity of the Planck emission at colder temperatures. Meanwhile, the dry polar atmosphere with small absorptivity enhances the longwave flux sensitivity at the surface. This results in the larger magnitude differences in sensitivities between the surface and atmospheric layers at higher latitudes, causing the surface temperature change to be critical for determining the OLR change. Thus, the near-surface polar heating induces the largest increase in OLR (Fig. 5.2b), which implies a smaller compensation from atmospheric energy transport $\delta\nabla \cdot F_{\mathrm{A}}$, according to Eq. 5.1.

To better quantify the dependence of $\delta\nabla \cdot F_{\mathrm{A}}$ on the vertical structure of polar warming, we express Eq. 5.1 in a flux form by subtracting the global average, integrating around the latitude circle, and integrating over the latitude from the South Pole:

$$\delta F_{\mathrm{A}} + \delta F_{\mathrm{R}} = -F_{\mathrm{Q}}, \tag{5.2}$$

where

$$F_{\mathrm{R}} \equiv -a^2 \int_{-\pi/2}^{\phi} \int_{0}^{2\pi} R_{\mathrm{TOA}} \; cos\phi d\lambda d\phi, \tag{5.3}$$

$$F_{\mathrm{Q}} \equiv -a^2 \int_{-\pi/2}^{\phi} \int_{0}^{2\pi} Q \;\; cos\phi d\lambda d\phi \,, \tag{5.4}$$

with ϕ the latitude, λ the longitude, and a the radius of Earth. Note that all flux terms (i.e., F_{A}, F_{R}, and F_{Q}) have the unit of PW. The prescribed Arctic heating Q implies a northward flux F_{Q}, as shown in Fig. 5.3a. The prescribed northward F_{Q} is compensated by atmospheric energy transport δF_{A} and TOA radiation δF_{R} that are both directed anomalously southward (Eq. 5.2 and Fig. 5.3a). The extent

ULSAN NATIONAL INSTITUTE OF SCIENCE AND TECHNOLOGY

to which the forcing is compensated by the atmospheric energy transport and TOA radiation is respectively measured by the atmospheric energy transport compensation $C_{\mathrm{A}} \equiv -\delta F_{\mathrm{A}}/F_{\mathrm{Q}}$ and the radiative compensation $C_{\mathrm{R}} \equiv -\delta F_{\mathrm{R}}/F_{\mathrm{Q}}$ (Kang et al., 2019). As the polar heating is applied at upper levels, the OLR response decreases due to the smaller local radiative kernel sensitivity and the weaker surface warming (Fig. 5.2), leading to a C_{R} reduction and a C_{A} increase (Fig. 5.3a).

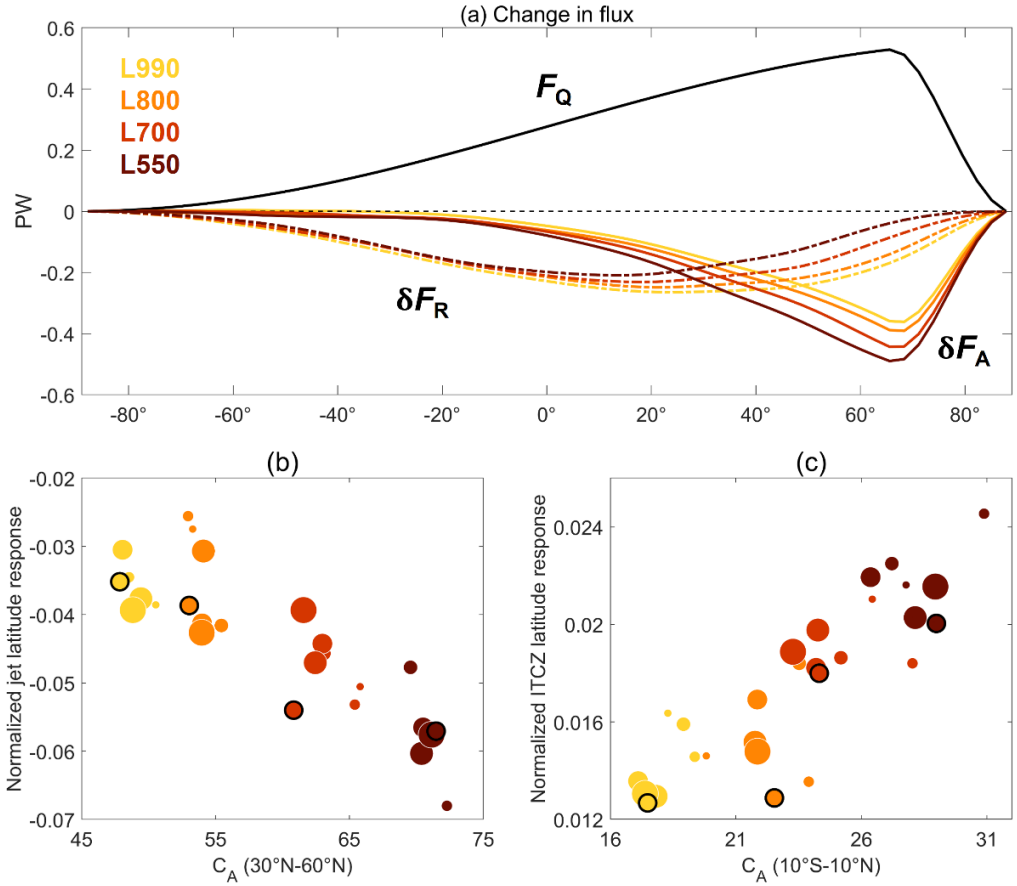

Figure 5.3. (a) The imposed heat flux (F_Q, black solid line), anomalous vertically-integrated atmospheric energy transport (δF_A, solid color-coded lines), and a flux corresponding to anomalous TOA radiation (δF_R, dashed color–coded lines) for the reference set of experiments with the same color coding as in Fig. 5.2b. (b) The response of the jet position, defined as the centroid latitude of 900 hPa zonal-mean zonal wind between 30°-60°N, normalized by the forcing amplitude as a function of atmospheric compensation C_{A} (%) averaged over 30°-60°N. (c) The response of the ITCZ position, defined as the centroid latitude of zonal-mean precipitation between 10°S-10°N normalized by the forcing amplitude, as a function of atmospheric compensation C_{A} (%) averaged over 10°S-10°N. The experiments with a varying forcing amplitude are differentiated by adjusting the marker size. The reference experiments are demarcated by black edge.

ULSAN NATIONAL INSTITUTE OF
SCIENCE AND TECHNOLOGY

The energy transport in the extratropics is mostly accomplished by eddies, so that a larger extratropical C_A implies a larger equatorward shift of extratropical jet position (Fig. 5.3b). Hence, the equatorward jet shift is more pronounced for upper-level polar heating (Figs. 5.1b and 5.4b). Conversely, the energy transport in the deep tropics is mostly accomplished by the mean Hadley circulation, so that a larger equatorial C_A infers a stronger cross-equatorial Hadley circulation and a larger shift in tropical rainfall. We measure the extent of tropical rainfall shift by the response of latitude centroid of zonal-mean precipitation between 10°S-10°N. The equatorial C_A increases with the vertical level of polar heating, leading to a stronger cross-equatorial Hadley circulation (Fig. 5.1c) and a larger northward shift of tropical rainfall (Fig. 5.3c). The equatorial C_A is in the range of 17-30 %, comparable to that in Seo et al. (2014). While the focus of Seo et al. (2014) is on the dependence of C_A on the latitudinal position of surface thermal forcing, our study reveals the sensitivity of C_A to the vertical level at which polar heating is imposed. Figures 5.3b and 5.3c further confirm the near-linearity of the response to the prescribed heating amplitude.

ULSAN NATIONAL INSTITUTE OF
SCIENCE AND TECHNOLOGY

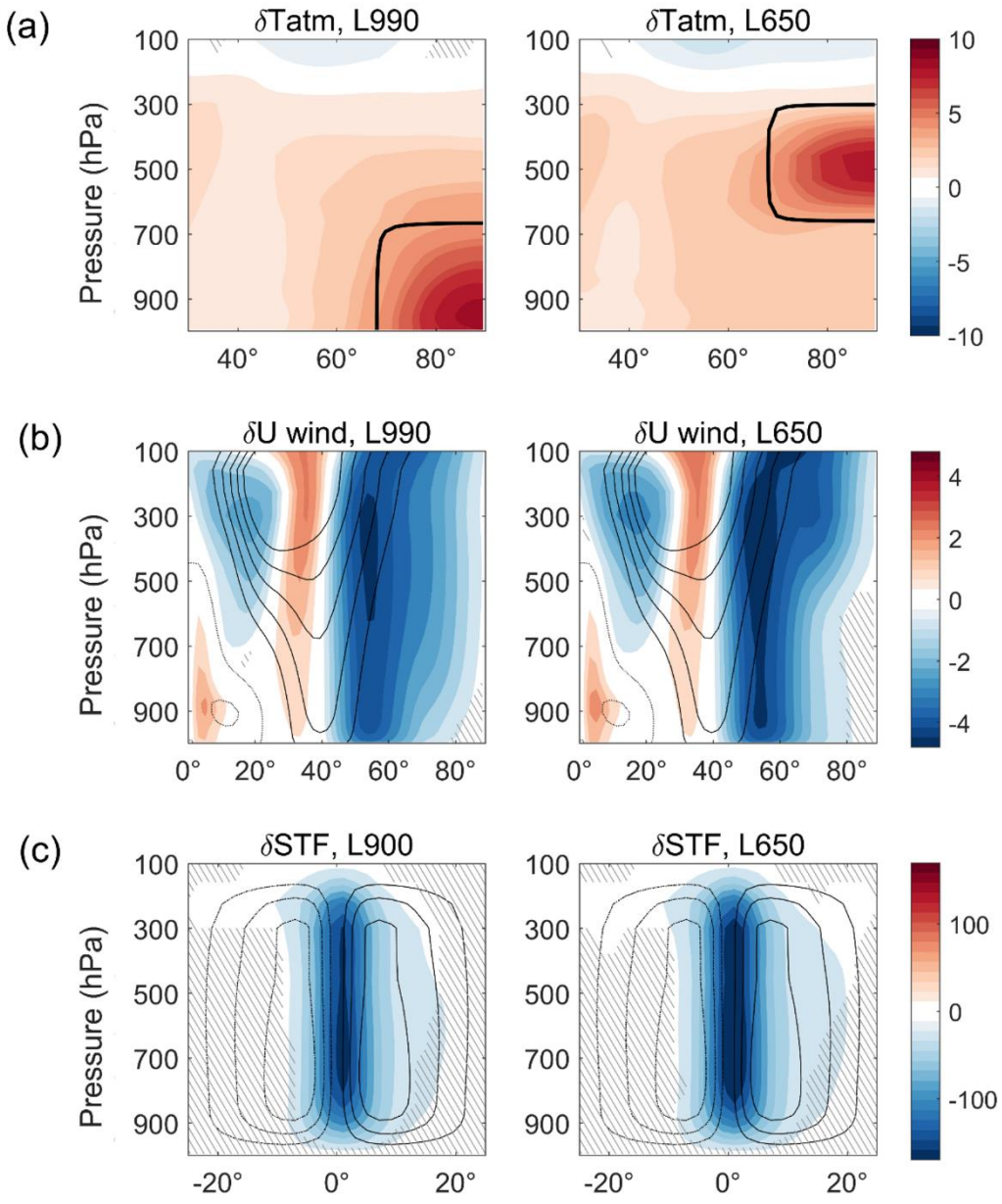

Figure 5.4. Same as Fig. 5.1 but for AM2 in (left) L990 and (right) L650.

ULSAN NATIONAL INSTITUTE OF SCIENCE AND TECHNOLOGY

The atmospheric compensation is greatly modulated by water vapor and cloud feedbacks (Kang et al., 2008; 2009; Clark et al., 2018), causing the sensitivity to the latitudinal position of surface thermal forcing to be distinct between GRaM and AM2 (Seo et al., 2014). The equatorial C_A decreases with the forcing latitude in GRaM, while the opposite tendency is found in AM2. However, the sensitivity to the vertical profile of polar heating is consistent between the two models (Figs. 5.1 and 5.4). The tendency for polar heatings to become more efficient in perturbing the remote climate the higher they are prescribed is also present in AM2 (Fig. 5.4): the mid-tropospheric polar heating induces a larger equatorward jet shift (Fig. 5.4b) and a stronger cross-equatorial Hadley circulation (Fig. 5.4c) than the near-surface polar heating. The sensitivity of TOA radiation response to the vertical level of polar heating is dominated by the clear-sky component (Fig. 5.5), with a larger clear-sky OLR response to the near-surface heating than to the mid-tropospheric heating owing to the dominance of surface contribution to OLR (blue line in Fig. 5.2d). As a result, the atmospheric compensation C_A increases as the polar heating is prescribed at higher levels: for mid-tropospheric and near-surface heating, respectively, C_A=181% and 163% when averaged over 10°S-10°N and C_A=63% and 51% when averaged over 30°N-60°N. The extratropical C_A in AM2 is comparable to that in GRaM, which ranges between 47% and 72%, with the same tendency to increase with the vertical level of polar heating (Fig. 5.3b). In contrast, the equatorial C_A in AM2 is noticeably larger than that in GRaM due to the positive water vapor feedback associated with a latitudinal shift of the intertropical convergence zone (Clark et al., 2018). The overcompensation by δF_A in the deep tropics further strengthens as the polar heating is imposed at higher levels, associated with a weaker negative TOA feedback in the polar forcing region.

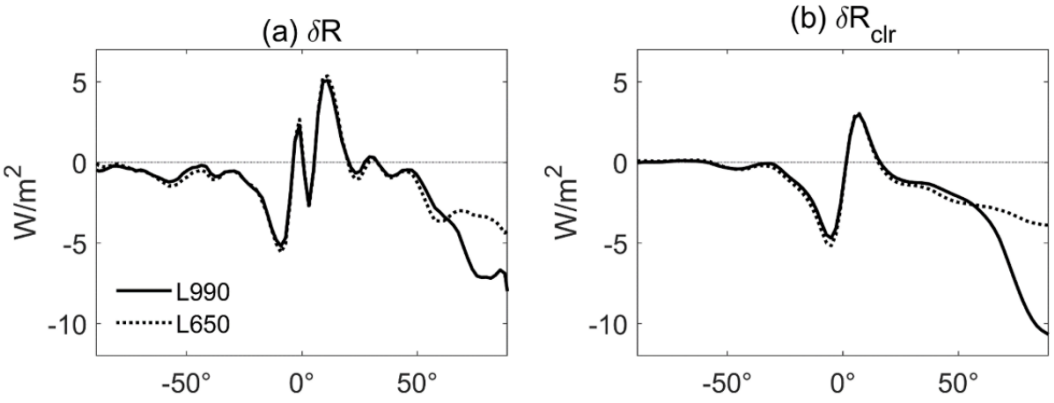

Figure 5.5. Zonal and time mean response of (a) net TOA radiation and (b) clear-sky TOA radiation in L990 (solid) and L650 (dashed) for AM2. Units are W/m^2.

ULSAN NATIONAL INSTITUTE OF
SCIENCE AND TECHNOLOGY

5.4. Summary and discussion

In this study, we examine the dependence of large-scale atmospheric circulations on the vertical structure of polar warming. In a series of aquaplanet slab ocean simulations with the gray radiation moist (GRaM) GCM and the comprehensive GFDL AM2, we impose the same amount of heating at different vertical levels poleward of 65°N. Regardless of the vertical profile, the Arctic warming leads to an equatorward shift of the extratropical jet associated with reduced baroclinicity (e.g., Butler et al., 2010). Also, the prescribed Arctic heating necessitates cross-equatorial energy transport away from the Northern Hemisphere with energy surplus, resulting in a northward displacement of the tropical rainfall (e.g., Kang 2020). These remote atmospheric circulations are more effectively perturbed when the polar heating is located at upper levels in both models. This robust sensitivity arises from the dominance of surface temperature contribution to the longwave TOA fluxes. Hence, the prescribed heating that causes larger changes in surface temperature is compensated more by radiative fluxes than by atmospheric energy transport. That is, the lower-level heating with larger surface temperature changes is more effectively compensated by TOA radiation, whereas the upper-level heating with weaker surface temperature changes requires more compensation from the atmospheric energy transport. A larger atmospheric compensation is accomplished by a larger equatorward jet shift and a stronger anomalous Hadley circulation that leads to a larger northward ITCZ shift. We confirm the linearity of this sensitivity from the experiments with a varying forcing amplitude. It is worth mentioning that temperature kernels in the tropics (e.g., Soden et al., 2008) have vertical structure that would suggest opposite sensitivities to what we show is important in determining the remote response to high-latitude forcing: the tropics have larger increases in OLR for upper-tropospheric warming compared to lower tropospheric warming, suggesting a larger radiative compensation to local forcing away from the surface. While we primarily discuss the tropospheric pathway, the stratospheric pathway has been emphasized in the Arctic-midlatitude linkages (e.g., Kim et al., 2014), which is worth exploring with a model with higher vertical resolution.

The vertical profile of Arctic warming will become less bottom-heavy with an ice-free Arctic when ice-albedo feedback is no longer operative (Screen and Simmonds 2010; Feldl et al., 2017). This implies that the efficiency of Arctic warming for perturbing the remote climate may increase in the future. In other words, the effect of Arctic warming on the midlatitude jet would strengthen relative to the compensating effect of tropical warming. This is consistent with recent studies showing a stronger Arctic-midlatitude connections with deep Arctic warming (He et al., 2020; Labe et al., 2020). A larger jet shift in response to upper- than to lower-level polar warming was also reported in Yuval and Kaspi (2016).

The lapse-rate feedback associated with the vertical structure of warming is often argued to be the largest contribution to Arctic amplification (Pithan and Mauritsen, 2014). It is thought that a larger

ULSAN NATIONAL INSTITUTE OF
SCIENCE AND TECHNOLOGY

increase in surface temperatures is required to offset a given TOA imbalance under the bottom-heavy warming profile. Interestingly, our study with vertically isolated temperature tendencies imposed shows the longwave TOA flux is most effectively changed via the surface because of the large emissivity of the polar atmosphere. Overall, we still lack a theoretical understanding of the high-latitude lapse rate feedback. It may not be the lapse rate feedback itself, but rather its interaction with other feedbacks from clouds, water vapor, and surface albedo (Bintanja et al., 2011; Pavelsky et al., 2011; Cronin and Jansen 2016; Kim et al., 2018; Henry et al., 2021) that renders the lapse-rate feedback as the most important contributor to the Arctic amplification. Thus, we need to better understand the vertical temperature structure at high latitudes and how it modulates the various feedback mechanisms.

One of the caveats of our study is omission of ocean dynamical feedback. While a fully coupled setup is more realistic than a slab ocean setup, it introduces additional sources of uncertainties that give rise to a large inter-model spread, as demonstrated by the Extratropical Tropical Interaction Model Intercomparison Project (ETIN-MIP; Kang et al., 2019). This justifies our starting point of a slab ocean model investigation of the robust atmospheric dynamics, while fully coupled model studies are warrant subsequent examination to determine the effects of ocean dynamics. As ocean dynamical feedback increases internal variability associated with El Niño-Southern Oscillation (ENSO), the entire hemispheric response originating from polar warming may be difficult to robustly identify in a fully coupled setup (Peings et al., 2021), a challenge we leave for future research.

ULSAN NATIONAL INSTITUTE OF
SCIENCE AND TECHNOLOGY

6. Summary

In this thesis, we address the questions of which feedback processes determine Arctic amplification and its remote effects. To disentangle the inter-connected feedback mechanisms in Arctic climate change, the mechanism denial approach with idealized model simulations and a suite of radiative feedback diagnostic frameworks are employed.

Chapter 3 investigates the sensitivity of polar amplification to varying insolation conditions and the role of cloud radiative effect on polar amplification. The insolation condition is conducted by the equinox (EQN), the annual-mean (ANN), and the seasonally varying (SEA). In response to a doubling of CO_2, the surface-amplified polar warming is present in the EQN experiment with the presence of a stable polar boundary layer. In contrast, the ANN and SEA experiments maximize the polar warming in the mid-troposphere by atmospheric energy transport. In SEA, the surface polar warming induced by atmospheric energy transport is considerably canceled by the negative shortwave cloud radiative effect (SWCRE) in the polar region, hence, there is no polar amplification in SEA compared to ANN. Thus, the strong negative SWCRE response is a local controlling factor for determining the degree of polar amplification, its seasonality, and other feedback mechanisms in the high latitudes.

In Chapter 4, we further quantify the Arctic SWCRE with extended approximate partial radiative perturbation (APRP). The extended APRP method–the method is applied at the Arctic surface and is validated by the PRP method–allows us to decompose the SWCRE response in a tightly coupled Arctic system. For future scenarios from the CMIP models, Arctic clouds damp the positive surface albedo feedback by albedo-cloud masking effect and albedo-cloud reflecting effect. Thus, a strong negative SWCRE response is directly linked to a reduction in surface albedo, of which a large inter-model spread of changes in SWCRE potentially stems from uncertainties in the surface albedo change. On the other hand, changes in Arctic cloud properties such as cloud amount and reflectivity have little impact on the changes in SWCRE and its inter-model variation, even though model differences in cloud properties mostly yield large uncertainties of SWCRE in the present-day.

The remaining chapter focus on the remote effects of polar warming depending on its vertical structure. In Chapter 3, we confirm that the vertical structure of polar warming is determined by various mechanisms. For example, large static stability in the polar boundary layer and albedo feedback gives rise to Arctic warming amplified near the surface, while atmospheric energy transport causes a pronounced mid-tropospheric warming. To test the sensitivity to the vertical polar warming structure, we use a series of experiments in which thermal forcing is applied at different vertical levels over the polar region. We find that the warming further from the surface is more effective at perturbing the remote climate, such as the extratropical jet and Hadley circulation, than the near-surface warming. This suggests that Arctic warming may have more far-reaching impacts in the near future as the Arctic

ULSAN NATIONAL INSTITUTE OF
SCIENCE AND TECHNOLOGY

transitions to an ice-free summer season and there is less near-surface warming.

Lastly, this thesis presents the following research originality: 1) a unique modeling setup and radiative kernel technique to review feedback mechanisms of Arctic amplification, focusing on the vertical structure of the Arctic warming and SWCRE in the Arctic, 2) a proposed extended decomposition method to quantify the projected negative SWCRE in the Arctic and its inter-model spread, and 3) first study to explain the mechanism of atmospheric circulation sensitivity to changes in the vertical structure of polar warming with targeted experiments and temperature kernels.

ULSAN NATIONAL INSTITUTE OF
SCIENCE AND TECHNOLOGY

Bibliography

Alexeev, V., P. L. Langen, and J. R. Bates. (2005). Polar amplification of surface warming on an aquaplanet in “ghost forcing” experiments without sea ice feedbacks. *Climate Dynamics*, **24,** 655-666.

Alkama, R., Taylor, P. C., Martin, G. S., Douville, H., Duveiller, G., Forzieri, G., ... & Cescatti, A. (2020). Clouds damp the radiative impacts of polar sea ice loss. *The Cryosphere*, **14**(8), 2673-2686.

Anderson, J. L., and Coauthors. (2004). The new GFDL global atmosphere and land model AM2–LM2: Evaluation with prescribed SST simulations. *J. Climate*, **17**, 4641–4673.

Arrhenius, S. (1896). XXXI. On the influence of carbonic acid in the air upon the temperature of the ground, The London, Edinburgh, and Dublin Philosophical Magazine and Journal of Science, 41(251), 237-276.

Baker, H. S., T. Woollings, and C. Mbengue. (2017). Eddy-driven jet sensitivity to diabatic heating in an idealized GCM. *Journal of Climate*, **30**(16), 6413-6431.

Bekryaev, R. V., I. V. Polyakov, and V. A. Alexeev. (2010). Role of polar amplification in long-term surface air temperature variations and modern Arctic warming, *Journal of Climate*, **23**(14), 3888-3906.

Bintanja, R., R. Graversen, and W. Hazeleger. (2011). Arctic winter warming amplified by the thermal inversion and consequent low infrared cooling to space, *Nature Geoscience*, **4**(11), 758-761.

Bintanja, R., E. Van der Linden, and W. Hazeleger. (2012). Boundary layer stability and Arctic climate change: a feedback study using EC-Earth. *Climate dynamics*, **39,** 2659-2673.

Boeke, R. C., and P. C. Taylor. (2018). Seasonal energy exchange in sea ice retreat regions contributes to differences in projected Arctic warming. *Nature communications*, **9,** 1-14.

Blackport, R., and Screen, J. A. (2021). Observed statistical connections overestimate the causal effects of Arctic Sea ice changes on midlatitude winter climate. *Journal of Climate*, **34**(8), 3021-3038.

Cai, M. (2005). Dynamical amplification of polar warming. *Geophysical Research Letters*, **32**.

Ceppi, P., D. L. Hartmann, and M. J. Webb. (2016). Mechanisms of the negative shortwave cloud

ULSAN NATIONAL INSTITUTE OF SCIENCE AND TECHNOLOGY

feedback in middle to high latitudes. *Journal of Climate*, **29,** 139-157.

Cesana, G., Kay, J. E., Chepfer, H., English, J. M., & De Boer, G. (2012). Ubiquitous low-level liquid-containing Arctic clouds: New observations and climate model constraints from CALIPSO-GOCCP. *Geophysical Research Letters*, **39**(20).

Charlock, T. P. and Ramanathan, V. (1985). The Albedo Field and Cloud Radiative Forcing Produced by a General Circulation Model with Internally Generated Cloud Optics, *Journal of the Atmospheric Sciences*, 42, 1408–1429.

Choi, Y. S., Hwang, J., Ok, J., Park, D. S. R., Su, H., Jiang, J. H., ... & Limpasuvan, T. (2020). Effect of Arctic clouds on the ice-albedo feedback in midsummer. *International Journal of Climatology*, **40**(10), 4707-4714.

Chen, G., Lu, and D. M. W. Frierson. (2008). Phase speed spectra and the latitude of surface westerlies: Interannual variability and global warming trend. *Journal of Climate*, **21**, 5942–5959.

Chiang, J. C., and C. M. Bitz. (2005). Influence of high latitude ice cover on the marine Intertropical Convergence Zone. *Climate Dynamics*, 25(5), 477-496.

Chung, E. S., Ha, K. J., Timmermann, A., Stuecker, M. F., Bodai, T., & Lee, S. K. (2021). Cold-season Arctic amplification driven by Arctic ocean-mediated seasonal energy transfer. *Earth's Future*, **9**(2), e2020EF001898.

Chung, C. E., and P. Räisänen. (2011). Origin of the Arctic warming in climate models. *Geophysical Research Letters*, **38**.

Clark, S. K., Ming, Y., Held, I. M., & Phillipps, P. J. (2018). The role of the water vapor feedback in the ITCZ response to hemispherically asymmetric forcings. *Journal of Climate*, **31**(9), 3659– 3678.

Cohen, J., and Coauthors. (2020). Divergent consensuses on Arctic amplification influence on midlatitude severe winter weather. *Nature Climate Change*, **10,** 20-29.

Cohen, J. L., J. C. Furtado, M. A. Barlow, V. A. Alexeev, and J. E. Cherry. (2012). Arctic warming, increasing snow cover and widespread boreal winter cooling. *Environmental Research Letters*, **7,**

ULSAN NATIONAL INSTITUTE OF SCIENCE AND TECHNOLOGY

014007.

Colman, R. A., & McAvaney, B. J. (1997). A study of general circulation model climate feedbacks determined from perturbed sea surface temperature experiments. *Journal of Geophysical Research: Atmospheres*, **102**(D16), 19383-19402.

Conley, A. J., Lamarque, J. F., Vitt, F., Collins, W. D., & Kiehl, J. (2013). PORT, a CESM tool for the diagnosis of radiative forcing. *Geoscientific Model Development*, **6**(2), 469-476.

Cronin, T. W., and M. F. Jansen. (2016). Analytic radiative-advective equilibrium as a model for high-latitude climate. *Geophysical Research Letters*, **43,** 449-457.

Danabasoglu, G., Lamarque, J. F., Bacmeister, J., Bailey, D. A., DuVivier, A. K., Edwards, J., ... & Strand, W. G. (2020). The community earth system model version 2 (CESM2). *Journal of Advances in Modeling Earth Systems*, **12**(2), e2019MS001916.

Deser, C., Tomas, R. A., & Sun, L. (2015). The role of ocean–atmosphere coupling in the zonal-mean atmospheric response to Arctic sea ice loss. *Journal of Climate*, **28**(6), 2168-2186.

England, M. R., L. M. Polvani, L. Sun, and C. Deser. (2020). Tropical climate responses to projected Arctic and Antarctic sea-ice loss. *Nature Geoscience*, **13**(4), 275-281.

English, J. M., Gettelman, A., & Henderson, G. R. (2015). Arctic radiative fluxes: Present-day biases and future projections in CMIP5 models. *Journal of Climate*, **28**(15), 6019-6038.

Eyring, V., Bony, S., Meehl, G. A., Senior, C. A., Stevens, B., Stouffer, R. J., & Taylor, K. E. (2016). Overview of the Coupled Model Intercomparison Project Phase 6 (CMIP6) experimental design and organization. Geoscientific Model Development (Online), 9(LLNL-JRNL-736881), 1937– 1958.

Feldl, N., and G. H. Roe. (2013a). The nonlinear and nonlocal nature of climate feedbacks. *Journal of Climate*, **26,** 8289-8304.

Feldl, N., and G. Roe. (2013b). Four perspectives on climate feedbacks. *Geophysical Research Letters*, **40,** 4007-4011.

ULSAN NATIONAL INSTITUTE OF SCIENCE AND TECHNOLOGY

Feldl, *S.* Bordoni, and T. M. Merlis. (2017a). Coupled High-Latitude Climate Feedbacks and Their Impact on Atmospheric Heat Transport. *Journal of Climate*, **30,** 189-201.

Feldl, N., B. T. Anderson, and S. Bordoni. (2017b). Atmospheric eddies mediate lapse rate feedback and Arctic amplification. *Journal of Climate*, **30**(22), 9213-9224

Feldl, N., Po-Chedley, S., Singh, H. K., Hay, S., & Kushner, P. J. (2020). Sea ice and atmospheric circulation shape the high-latitude lapse rate feedback. *NPJ climate and atmospheric science*, **3**(1), 1-9.

Francis, J. A., and S. J. Vavrus. (2012). Evidence linking Arctic amplification to extreme weather in mid-latitudes. *Geophysical research letters*, **39**(6).

Freidenreich, S. M., S. T. Garner, R. G. Gudgel, C. Gordon, and I. M. Held. (2004). The new GFDL global atmosphere and land model AM2–LM2: Evaluation with prescribed SST simulations. *Journal of Climate*, **17,** 4641-4673.

Frierson, D. M., I. M. Held, and P. Zurita-Gotor. (2007). A gray-radiation aquaplanet moist GCM. Part II: Energy transports in altered climates. *Journal of the atmospheric sciences*, **64,** 1680-1693.

Gelaro, R., McCarty, W., Suarez, M. J., Todling, R., Molod, A., Takacs, L., … Zhao, B. (2017). The Modern-Era Retrospective Analysis for Research and Applications, Version 2 (MERRA-2). *Journal of Climate*, **30**(14), 5419– 5454.

Gettelman, A. (2015). Putting the clouds back in aerosol–cloud interactions. *Atmospheric Chemistry and Physics*, **15,** 12397-12411.

Graversen, R. G., and M. Wang. (2009). Polar amplification in a coupled climate model with locked albedo. *Climate Dynamics*, **33,** 629-643.

Graversen, R. G., and M. Burtu. (2016). Arctic amplification enhanced by latent energy transport of atmospheric planetary waves. *Quarterly Journal of the Royal Meteorological Society*, **142,** 2046-2054.

Graversen, R. G., P. L. Langen, and T. Mauritsen. (2014). Polar amplification in CCSM4: Contributions from the lapse rate and surface albedo feedbacks, *Journal of Climate*, **27**(12), 4433-4450.

ULSAN NATIONAL INSTITUTE OF SCIENCE AND TECHNOLOGY

Hansen, J. e., and Coauthors. (2005). Efficacy of climate forcings. *Journal of Geophysical Research: Atmospheres*, **110**.

He, S., Xu, X., Furevik, T., & Gao, Y. (2020). Eurasian cooling linked to the vertical distribution of Arctic warming. *Geophysical Research Letters*, **47**(10), e2020GL087212.

Held, I. M., and E. O'Brien. (1992). Quasigeostrophic turbulence in a three-layer model: Effects of vertical structure in the mean shear. *Journal of the Atmospheric Sciences*, **49**, 1861–1870.

Henry, M., T. M. Merlis, N. J. Lutsko, and B. E. J. Rose. (2021). Decomposing the drivers of polar amplification with a single column model. *Journal of Climate*, **34**, 2355-2365.

Hersbach, H., Bell, B., Berrisford, P., Hirahara, S., Horányi, A., Muñoz-Sabater, J., ... & Thépaut, J. N. (2020). The ERA5 global reanalysis. *Quarterly Journal of the Royal Meteorological Society*, **146**(730), 1999-2049.

Holland, M. M., and C. M. Bitz. (2003). Polar amplification of climate change in coupled models. *Climate Dynamics*, **21**(3-4), 221-232.

Hofer, S., A. J. Tedstone, X. Fettweis, and J. L. Bamber. (2017). Decreasing cloud cover drives the recent mass loss on the Greenland Ice Sheet. *Science Advances*, **3,** e1700584.

Holland, M. M., and C. M. Bitz. (2003). Polar amplification of climate change in coupled models. *Climate Dynamics*, **21,** 221-232.

Hu, X., P. C. Taylor, M. Cai, S. Yang, Y. Deng, and S. Sejas. (2017). Inter-Model Warming Projection Spread: Inherited Traits from Control Climate Diversity, *Scientific Reports*, 7(1), 4300.

Huang, Y., Xia, Y., and Tan, X. (2017). On the pattern of CO2 radiative forcing and poleward energy transport. *Journal of Geophysical Research: Atmospheres*, **122**(20), 10-578.

Huang, Y., X. Tan, and Y. Xia. (2016). Inhomogeneous radiative forcing of homogeneous greenhouse gases. *Journal of Geophysical Research: Atmospheres*, **121,** 2780-2789.

Hwang, Y. -T., D. M. Frierson, and J. E. Kay. (2011). Coupling between Arctic feedbacks and changes in poleward energy transport. *Geophysical Research Letters*, **38**, L17704

ULSAN NATIONAL INSTITUTE OF SCIENCE AND TECHNOLOGY

Inoue, J., and M. E. Hori. (2011). Arctic cyclogenesis at the marginal ice zone: A contributory mechanism for the temperature amplification? *Geophysical Research Letters*, **38**, L12502

Kang, S. M. (2020). Extratropical influence on the tropical rainfall distribution. *Current Climate Change Reports*, **6**(1), 24-36.

Kang, S. M., Frierson, D. M., and Held, I. M. (2009). The tropical response to extratropical thermal forcing in an idealized GCM: The importance of radiative feedbacks and convective parameterization. *Journal of the atmospheric sciences*, **66**(9), 2812-2827.

Kang, S. M., Hawcroft, M., Xiang, B., Hwang, Y. T., Cazes, G., Codron, F., et al. (2019). Extratropical–Tropical Interaction Model Intercomparison Project (ETIN-MIP): Protocol and initial results. *Bulletin of the American Meteorological Society*, **100**(12), 2589– 2606.

Kang, S. M., I. M. Held, D. M. Frierson, and M. Zhao. (2008). The response of the ITCZ to extratropical thermal forcing: Idealized slab-ocean experiments with a GCM, *Journal of Climate*, **21**(14), 3521-3532.

Karlsson, J., & Svensson, G. (2013). Consequences of poor representation of Arctic sea-ice albedo and cloud-radiation interactions in the CMIP5 model ensemble. *Geophysical Research Letters*, **40**(16), 4374-4379.

Kay, J.E. and Gettelman, A. (2009). Cloud influence on and response to seasonal Arctic Sea ice loss. *Journal of Geophysical Research*, **114**, D18204.

Kay, J. E., M. M. Holland, C. M. Bitz, E. Blanchard-Wrigglesworth, A. Gettelman, A. Conley, and D. Bailey. (2012). The influence of local feedbacks and northward heat transport on the equilibrium Arctic climate response to increased greenhouse gas forcing, *Journal of Climate*, **25**(16), 5433-5450.

Kay, J.E. and L'Ecuyer, T. (2013). Observational constraints on Arctic Ocean clouds and radiative fluxes during the early 21st century. *Journal of Geophysical Research*, **118**, 7s219–7236.

Kay, J. E., L'Ecuyer, T., Chepfer, H., Loeb, N., Morrison, A., & Cesana, G. (2016). Recent advances in Arctic cloud and climate research. *Current Climate Change Reports*, **2**(4), 159-169.

Kim, B. M., Son, S. W., Min, S. K., Jeong, J. H., Kim, S. J., Zhang, X., et al. (2014). Weakening of the stratospheric polar vortex by Arctic sea-ice loss. *Nature Communications*, **5**(1), 1– 8.

ULSAN NATIONAL INSTITUTE OF SCIENCE AND TECHNOLOGY

Kim, D., Kang, S. M., Merlis, T. M., & Shin, Y. (2021). Atmospheric circulation sensitivity to changes in the vertical structure of polar warming. *Geophysical Research Letters*, **48**(19), e2021GL094726.

Kim, D., S. M. Kang, Y. Shin, and N. Feldl. (2018). Sensitivity of polar amplification to varying insolation conditions. *Journal of Climate*, **31**, 4933-4947.

Klocke, D., Quaas, J., & Stevens, B. (2013). Assessment of different metrics for physical climate feedbacks. *Climate dynamics*, **41**(5), 1173-1185.

Kim, H., Pendergrass, A. G., & Kang, S. M. (2022). The Dependence of Mean Climate State on Shortwave Absorption by Water Vapor. *Journal of Climate*, **35**(7).

Kumar, A., Perlwitz, J., Eischeid, J., Quan, X., Xu, T., Zhang, T., et al. (2010). Contribution of sea ice loss to Arctic amplification. *Geophysical Research Letters*, **37**(21).

Labe, Z., Peings, Y., & Magnusdottir, G. (2020). Warm Arctic, cold Siberia pattern: role of full Arctic amplification versus sea ice loss alone. *Geophysical Research Letters*, **47**(17), e2020GL088583.

Laliberté, F., and P. J. Kushner. (2014). Midlatitude moisture contribution to recent Arctic tropospheric summertime variability. *Journal of Climate*, **27**, 5693-5707.

Langen, P. L., R. G. Graversen, and T. Mauritsen. (2012). Separation of contributions from radiative feedbacks to polar amplification on an aquaplanet. *Journal of Climate*, **25,** 3010-3024.

Lawrence, D. M., Fisher, R. A., Koven, C. D., Oleson, K. W., Swenson, S. C., Bonan, G., ... & Zeng, X. (2019). The Community Land Model version 5: Description of new features, benchmarking, and impact of forcing uncertainty. *Journal of Advances in Modeling Earth Systems*, **11**(12), 4245-4287.

Lu, J., and M. Cai. (2009). Seasonality of polar surface warming amplification in climate simulations. *Geophysical Research Letters*, **36**, L16704

Manabe, S., and R. T. Wetherald. (1975). The effects of doubling the CO2 concentration on the climate of a general circulation model, *Journal of the Atmospheric Sciences*, **32**(1), 3-15.

Manabe, S., R. Stouffer, M. Spelman, and K. Bryan. (1991). Transient responses of a coupled ocean–

ULSAN NATIONAL INSTITUTE OF SCIENCE AND TECHNOLOGY

atmosphere model to gradual changes of atmospheric CO2. Part I. Annual mean response, *Journal of Climate*, **4**(8), 785-818.

Manabe, S., M. Spelman, and R. Stouffer. (1992). Transient responses of a coupled ocean-atmosphere model to gradual changes of atmospheric CO2. Part II: Seasonal response, *Journal of Climate*, **5**(2), 105-126.

Meredith, M., Sommerkorn, M., Cassotta, S., Derksen, C., Ekaykin, A., Hollowed, A., et al. (2019). Polar regions. Chapter 3, IPCC special report on the ocean and cryosphere in a changing climate.

Merlis, T. M., and M. Henry. (2018). Simple estimates of polar amplification in moist diffusive energy balance models, *Journal of Climate*, **31**(15), 5811-5824.

Mori, M., M. Watanabe, H. Shiogama, J. Inoue, and M. Kimoto. (2014). Robust Arctic sea-ice influence on the frequent Eurasian cold winters in past decades. *Nature Geoscience*, **7**(12), 869.

Pauluis, O., A. Czaja, and R. Korty. (2008). The global atmospheric circulation on moist isentropes. *Science*, **321,** 1075-1078.

Pavan, V., & Held, I. M. (1996). The diffusive approximation for eddy fluxes in baroclinically unstable jets. *Journal of the Atmospheric Sciences*, **53**(9), 1262– 1272.

Pavelsky, T. M., J. Boé, A. Hall, and E. J. Fetzer. (2011). Atmospheric inversion strength over polar oceans in winter regulated by sea ice, *Climate dynamics*, **36**(5-6), 945-955.

Park, K., S. M. Kang, D. Kim, M. F. Stuecker, and F.-F. Jin. (2018). Contrasting local and remote impacts of surface heating on polar warming and amplification. *Journal of Climate*, **31,** 3155-3166.

Perovich, D. K., J. A. Richter-Menge, K. F. Jones, and B. Light. (2008). Sunlight, water, and ice: Extreme Arctic sea ice melt during the summer of 2007. *Geophysical Research Letters*, **35**.

Peixoto, J. P., and A. H. Oort. (1992). *Physics of Climate*, Am. Inst. of Phys., New York.

Pendergrass, A. G., Conley, A., and Vitt, F. M. (2018). Surface and top-of-atmosphere radiative feedback kernels for CESM-CAM5. *Earth System Science Dat*a, **10**(1), 317-324.

Peings, Y., Labe, Z. M., & Magnusdottir, G. (2021). Are 100 ensemble members enough to capture the

ULSAN NATIONAL INSTITUTE OF SCIENCE AND TECHNOLOGY

remote atmospheric response to +2℃ Arctic sea ice loss? *Journal of Climate*, **34**(10), 3751-3769.

Pithan, F., and T. Mauritsen. (2014). Arctic amplification dominated by temperature feedbacks in contemporary climate models. *Nature Geoscience*, **7,** 181-184.

Screen, J. A., C. Deser, and I. Simmonds. (2012). Local and remote controls on observed Arctic warming. *Geophysical Research Letters*, **39**.

Screen, J. A., and I. Simmonds. (2010). The central role of diminishing sea ice in recent Arctic temperature amplification. *Nature*, **464,** 1334-1337.

Sejas, S., M. Cai, A. Hu, J. Meehl, W. Washington, and P. Taylor. (2014). On the seasonality of polar warming amplification, *Journal of Climate*, **27**, 5653-5669.

Serreze, M., A. Barrett, J. Stroeve, D. Kindig, and M. Holland. (2009). The emergence of surface-based Arctic amplification. *The Cryosphere*, **3,** 11.

Sledd, A., and T. L'Ecuyer. (2019). How much do clouds mask the impacts of Arctic sea ice and snow cover variations? Different perspectives from observations and reanalyses. *Atmosphere*, **10,** 12

Seo, J., S. M. Kang, and D. M. Frierson. (2014). Sensitivity of intertropical convergence zone movement to the latitudinal position of thermal forcing. *Journal of Climate*, **27**(8), 3035-3042.

Shaw, T. A., and A. Voigt. (2016). What can moist thermodynamics tell us about circulation shifts in response to uniform warming? *Geophysical Research Letters*, **43**, 4566–4575, doi:10.1002/2016GL068712.

Shell, K. M., Kiehl, J. T., and Shields, C. A. (2008). Using the radiative kernel technique to calculate climate feedbacks in NCAR's Community Atmospheric Model. *Journal of Climate*, **21**(10), 2269-2282.

Singh, H., P. Rasch, and B. Rose. (2017). Increased Ocean Heat Convergence into the High Latitudes with CO2-Doubling Enhances Polar-Amplified Warming. *Geophysical Research Letters*, **44**(20).

Smith, R., Jones, P., Briegleb, B., Bryan, F., Danabasoglu, G., Dennis, J., ... & Yeager, S. (2010). The parallel ocean program (POP) reference manual ocean component of the community climate system model (CCSM) and community earth system model (CESM). LAUR-01853, 141, 1-140.

ULSAN NATIONAL INSTITUTE OF SCIENCE AND TECHNOLOGY

Smith, C. J. (2018). HadGEM2 radiative kernels. University of Leeds.

Smith, D. M., Dunstone, N. J., Scaife, A. A., Fiedler, E. K., Copsey, D., & Hardiman, S. C. (2017). Atmospheric response to Arctic and Antarctic sea ice: The importance of ocean-atmosphere coupling and the background state. *Journal of Climate*, **30**(12), 4547– 4565.

Soden, B. J., I. M. Held, R. Colman, K. M. Shell, J. T. Kiehl, and C. A. Shields. (2008). Quantifying climate feedbacks using radiative kernels. *Journal of Climate*, **21,** 3504-3520.

Solomon, S.. (2007). *Climate change 2007-the physical science basis: Working group I contribution to the fourth assessment report of the IPCC.* Vol. 4, Cambridge University Press.

Stuecker, M. F., and Coauthors. (2018). Polar amplification dominated by local forcing and feedbacks. *Nature Climate Change*, **8,** 1076-1081.

Taylor, K., and Coauthors. (2007). Estimating shortwave radiative forcing and response in climate models. *Journal of Climate*, **20,** 2530-2543.

Taylor, P. C., and Coauthors. (2021). Process drivers, inter-model spread, and the path forward: A review of amplified Arctic warming.

Taylor, P. C., R. G. Ellingson, and M. Cai. (2011a). Seasonal variations of climate feedbacks in the NCAR CCSM3, *Journal of Climate*, **24**(13), 3433-3444.

Taylor, P. C., R. G. Ellingson, and M. Cai. (2011b). Geographical distribution of climate feedbacks in the NCAR CCSM3. 0, *Journal of Climate*, **24**(11), 2737-2753.

Taylor, P. C., S. Kato, K. M. Xu, and M. Cai. (2015). Covariance between Arctic sea ice and clouds within atmospheric state regimes at the satellite footprint level, *Journal of Geophysical Research: Atmospheres*, **120**(24), 12656-12678.

Tiedtke, M. (1993). Representation of clouds in large-scale models. *Monthly Weather Review*, **121,** 3040-3061.

Tjernström, M., and R. G. Graversen. (2009). The vertical structure of the lower Arctic troposphere

ULSAN NATIONAL INSTITUTE OF SCIENCE AND TECHNOLOGY

analysed from observations and the ERA40 reanalysis, *Quarterly journal of the royal meteorological society*, **135**(639), 431-443.

Thorsen, T. J., Kato, S., Loeb, N. G., & Rose, F. G. (2018). Observation-based decomposition of radiative perturbations and radiative kernels. *Journal of climate*, **31**(24), 10039-10058.

Vavrus, S. (2004). The impact of cloud feedbacks on Arctic climate under greenhouse forcing. *Journal of Climate*, **17,** 603-615.

Vavrus, S., D. Waliser, A. Schweiger, and J. Francis. (2009). Simulations of 20th and 21st century Arctic cloud amount in the global climate models assessed in the IPCC AR4. *Climate Dynamics*, **33,** 1099-1115.

Wetherald, R. T., and S. Manabe. (1981). Influence of seasonal variation upon the sensitivity of a model climate, *Journal of Geophysical Research: Oceans*, **86**(C2), 1194-1204.

Wetherald, R. T., and S. Manabe. (1988). Cloud feedback processes in a general circulation model. *Journal of the Atmospheric*, **45**, 1397–1415.

Winton, M. (2005). Simple optical models for diagnosing surface–atmosphere shortwave interactions. *Journal of climate*, **18**(18), 3796-3805.

Winton, M. (2006). Amplified Arctic climate change: What does surface albedo feedback have to do with it? *Geophysical Research Letters*, **33**, 1099-1115.

Wu, Y., , M. Ting, , R. Seager, , H.-P. Huang, , and M. A. Cane. (2011). Changes in storm tracks and energy transports in a warmer climate simulated by the GFDL CM2.1 model. *Climate Dynamics*, **37**, 53–72.

Yuval, J., and Kaspi, Y. (2016). Eddy activity sensitivity to changes in the vertical structure of baroclinicity. *Journal of the Atmospheric Sciences*, **73**(4), 1709-1726.

Zappa, G., Ceppi, P., & Shepherd, T. G. (2021). Eurasian cooling in response to Arctic sea-ice loss is not proved by maximum covariance analysis. *Nature Climate Change*, **11**(2), 106-108.

ULSAN NATIONAL INSTITUTE OF
SCIENCE AND TECHNOLOGY

Acknowledgement

감사의 글

내가 산을 향하여 눈을 들리라 나의 도움이 어디서 올까

나의 도움은 천지를 지으신 여호와에게서로다.

시편 121편 (PSALM 121)

I lift up my eyes to the mountains—where does my help come from?

My help comes from the LORD, the Maker of heaven and earth.

제가 박사 과정을 밟는 동안 도움을 주신 많은 분들 덕분에 학위 논문 마지막 페이지를 빌려 감사한 마음을 전할 수 있게 되었습니다. 모두 정말 감사드립니다.

먼저, 제가 박사과정이라는 여정을 이탈하지 않고, 항해를 잘 마칠 수 있게 해준 선장님 이신 강사라 교수님, 진심으로 감사합니다. '대기 역학이 재밌어서' 라는 단순한 이유로 대학원 과정을 시작하였고, 특히 교수님 역학 수업은 최고로 재밌고, 유익했습니다. 교수님께서는 저를 한 명의 학생으로 대하시기 보다 같이 클 수 있는 연구자로 인격적으로 대해 주시고 믿어 주셨습니다. 또한, 제가 넓고 크게 성장할 수 있도록 국내외로 많은 기회도 주셨습니다. 그 외에도 연구하는 방법, 자세, 발표에서 논문 쓰기까지 정말 열정적으로 지도해 주셔서 누구보다도 많이 배울 수 있었습니다. 하지만 6년이라는 시간이 짧지 않았고, 많은 시간 동안 미래에 대한 고민들과 현재에 대한 걱정으로 어두운 터널을 거닐 때가 많았습니다. 그때 마다, 교수님께서 응원해주시고 길을 열어 주셔서 제가 이 학위를 무사히 마칠 수 있었다고 생각합니다. 제가 응석 아닌 응석을 부릴 때 마다 교수님께서 따뜻한 관심과 애정으로 지지 해주시고, 버팀목이 되어 주셔서 감사합니다. 앞으로도, 교수님 옆에서 자랑스러운 제자 되도록, 좋은 연구자로 성장하겠습니다.

다음으로, 학위 논문을 심사해 주신 이명인 교수님과 차동현 교수님께 감사 인사를 드립니다. 수업을 들을 때마다, 또 두 분을 밤 늦은 시간이나 주말에 복도에서 뵐 때 마다 정말 박사는 시작에 불과하고 연구자의 길은 끊임없는 노력이 필요 하구나를 늘 깨닫습니다. 저 또한 이 두 분의 열정을 꼭 기억하여 열심히 연구하여 더 성장하는 연구자 되겠습니다. 또한, 바쁘신 와중에도 심사해주신 김백민 교수님께도 감사드립니다. 처음 대학원 입학하여 극지연구소 출장에서 교수님을 뵈었을 때 만해도 제가 북극 연구를 하게 될 줄 몰랐는데, 교수님께서 그때 해 주신 연구이야기(북극곰이야기도)가 너무 흥미로워서 저도 북극 연구에 빠져버렸던 것 같습니다. 외부에서 강연해 주실 때 마다 너무 재미있었고, 귀에 쏙쏙 들어와서 저 또한 저렇게 설명을 잘 할 수 있는 과학자가 되고 싶다고 생각했습니다. 앞으로 북극 연구하면서 교수님과 함께 흥미로운 문제들을 풀어

ULSAN NATIONAL INSTITUTE OF SCIENCE AND TECHNOLOGY

나갈 수 있었으면 좋겠습니다. I cannot express enough thanks to Malte (Dear Prof. Malte F. Stuecker). You were the one always there during my graduate school, giving helpful advice and ideas to accomplish my work. I really enjoyed collaborating work with you and hope we can work together soon. Thank you! 심사위원으로 모시지는 못했지만, 제 연구에 많은 도움을 주신 Nicole Feldl 교수님과 Tim Merlis에게 감사인사를 인사를 드립니다 (I also deeply appreciate the advice from Prof. Nicole Feldl and Tim Merlis).

대학원 생활동안 항상 가족처럼 곁에서 기쁜 일과 슬픈 일을 함께한 연구실사람들에게도 감사합니다. 먼저 신예철 박사님, 너 때문에 그만 둘 뻔했는데 너 때문에 대학원 잘 마칠 수 있었어. 우리 동기로 만나서 항상 같이 붙어서 연구하고, 맛있는 거 먹고, 교회도 다니고, 힘든 일 같이 하면서 정말 이제는 너무 너무 중요한 사이가 된 것 같아. 우리 도원 결의 있지 말고 오래도록 함께 잘해보자! 너는 똑똑하고 또 누구보다 열심히 하는 사람이니까 대기 과학계에 한 획을 그을 거라 믿어 의심치 않는다! 항상 기도하고 응원할게. 그리고 아무것도 몰랐던 나 잘 가르쳐주고, 긴 대학원생활 동안 옆에서 든든히 버텨줘서 진심으로 감사해. 힘내자!! 김한준 박사님, 우리 셋 중에 한명이라도 없었으면 대학원 못 다녔다고 우리 늘 입버릇처럼 말했잖아. 정말 너가 빠진 대학원생활은 상상도 할 수가 없어. 착하고 성실해서 옆에서 늘 도와주고, 챙겨주고, 기만(?)하고 너무 고마워. 몸이 힘든 와중에도 끊임없는 너의 연구 열정은 정말 옆에서 많은 배움이 되었어. 너는 어느 곳에 데려다 놓아도 잘 할 아이라서 걱정이 안된다. 너에게 고마운 건 정말 많은데 그렇기엔 지면을 다 채우고도 부족할 것 같아. 연구실 생활 동안 누구보다 고생한 우리 한준이 수고했어! 우리 같이 좋은 연구자 되고, 또 어디서나 행복하자!

박기웅에게, 처음에 힘든 시간들 함께하는 와중에 나갈 땐 너무 슬펐는데, 왠 걸? 사람 일은 한치 앞도 모른다더니 지금 너무 성공하고 잘 살고 있어서 내가 다 행복하다. 앞으로도 우리 꽃 길 만 걷자 기웅아~! 지영이에게, 너랑 함께 대학원에 있었을 때가 제일 재미 있었던 것 같아, 나랑 놀아줘서 고마워~ 조용하지만 강단 있고, 다른 사람들과 잘 스며들어서 우리 연구실 중간다리 역할을 톡톡히 해줬지. 지영이는 연구도 일도 잘하니까 다른 곳에서도 잘 할 꺼야, 근데 제주도도 좋더라! 또 놀러 갈게~! 해외에서 열연 중인 지흔이와 찬영에게, 둘 다 연구실 들어왔을 때 잘 가르쳐주지도 못했는데 연구 정말 잘한다고 생각해~ 앞으로도 계속 우리 다같이 만나서 시간 보낼 수 있었으면 좋겠다. 지흔아, 오랜만에 보니 너무 좋더라, 너는 야무지니까 영국에서 좋은 연구할 수 있을 거라 생각해. 찬영아, 맨날 교식 같이 먹어줘서 고마워! 네가 지나치지도 부족하지도 않게 항상 잘 대해 줘서 편안했어. 너는 연구도 뚝심 있게 잘하니까 미국에서도 잘할 꺼라 믿어. 우리 연구실의 미래! 연구실의 자랑! 도석아! 네가 들어온 일이 엊그제 같은데 연구도 너무 잘하고, 코딩도, 인턴 친구들도 척척 가르치고 대단해. 너만 있어도 연구실 걱정이 없다. 연구실의 미래로서 또 많이 도와줘서 고맙고, 언제든지 도움이 필요하면 연락해~! 덧붙여, 초기 멤버로서 제가 연구실에 들어오고 싶게 해줬던 정빈 언니와 무찬이도 언제나 응원합니다.

대학원 동기로서, 밥 친구로, 밤 12시넘어서도 연구실에서 만날 수 있는, 주말에는 카공 멤버로, 힘들 때 어려울 때 함께한 이승희님. 누구보다 열심히 잘 하고 계시니 원하는 바 뭐든 성취하실

ULSAN NATIONAL INSTITUTE OF SCIENCE AND TECHNOLOGY

거라 믿습니다. 이번 학기 같이 졸업준비 열심히 했던 주현, 서희언니, 해리언니, 동혁이도 고맙습니다. 여러분들의 열정으로 봐서는 뭐든 잘 하실 것이라 믿습니다. 무용지물인 가벽으로 함께 했던 차동현 교수님 방 친구들과 이명인 교수님, 송창근 교수님 방 친구들도 정말 고맙습니다 (사람이 너무 많아서 이렇게 쓰는 걸 용서해주세요). 방금 전 주말까지 남아있던 은령언니와 또 다른 카공 멤버인 지해, 동기로 함께했던 선주언니, 우리 연구실 대소사에 함께하는 이혁재님 고맙습니다.

친구들에게 감사드립니다. 내 소중한 친구, 성연이. 바쁘다는 핑계로 자주 못보지만 너가 있다는 자체가 나에게 큰 힘이 돼. 함께 대기 과학공부를 시작했지만 이제는 각자 좋은 길로 흩어진 보름이, 여진이, 수정이, 소나, 한솔이, 현정이 10년이 다 되가는 시간동안 언제나 함께해줘서 고마워. Merci beaucoup, "POLAR BEAR" Charles! 언제나 날 응원해주는 교회사람들 감사합니다, 인선아 ~ 너가 있어서 너무 고마워. 지나갔지만, 많은 시간동안 힘이 되어준 깡이도 고맙습니다. 끝으로 졸업으로 너무 바빴을 때 옆에서 이해해주고, 또 행복한 시간 만들어 준 웅걸이에게 감사합니다.

가족들에게 감사드립니다. 어렸을때 부터 따박 따박 말대답하는 버릇을 못 고쳐서 연구를 따박 따박 따져가며 잘 하고 있습니다. 모든 일에 "왜?" "왜?"라고 물으며 엄마를 괴롭혔기에 연구도 그 호기심으로 적성에 맞게 하고 있습니다. 저는 두 자매를 키우기 위해 보험 회사, 우유 배달, 맥도날드까지 이른 아침부터 늦은 밤까지 열심히 일하고, 주말에는 도서관에서 일하시면서 그 와중에 대학에서 학위를 받으시고, 독서지도사, 수화, 일본어, 중국어, 영어까지 무슨 일이든 배우고 도전하시는 어머니 밑에서 컸습니다. 저에게 뭐든 배우고 싶은 것, 하고 싶은 것 하도록 지지해주시고. 희생하신 어머니가 있었기에 제가 이 자리에 있다고 생각합니다. 어머니가 늘 말씀해 주셨던 "빛좋은 개살구같이 살지 말라"에서 이제 조금 달콤새콤한 살구가 된 것 같습니다. 겉보기가 아닌 진짜 맛있는 살구 되도록 열심히 노력하겠습니다. 세상에서 제일 존경하는 우리 엄마, 고맙고 사랑합니다. 자랑스러운 딸 될 테니 기대하세요. 제 하나뿐인 동생에게도 감사합니다. 어렸을 때부터 뭐든 잘해내고 어디를 가든 사랑 받는 내 동생 륜희야, 일본에서 학위과정을 밟고, 어엿한 직장인이 되어 열심히 사는 네 모습이 자랑스러워. 자주 연락 못하지만 늘 사랑하고 고마워. 또한 저를 많이 응원해주신, 할아버지, 스님삼촌, 울산삼촌, 이모, 숙모, 사촌들과 친척들에게 모두 감사합니다.

마지막으로, 여기까지 인도해주신 하나님 아버지 감사합니다.